

Advanced Material Modeling in EM-FDTD

Diss. ETH No. 17969

Advanced Material Modeling in EM-FDTD

A dissertation submitted to the
SWISS FEDERAL INSTITUTE OF TECHNOLOGY
ZURICH

for the degree of
Doctor of Sciences

presented by
STEFAN SCHILD
MSc ETH
born 04 04 1977
citizen of Switzerland

accepted on the recommendation of
Prof. Dr. W. Fichtner, examiner
Prof. Dr. N. Kuster, Prof. Dr. M. Okoniewski, co-examiner

2008

Contents

Summary	ix
Zusammenfassung	xiii
Acknowledgments	xvii
I Background	1
1 Introduction	3
1.1 Motivation and Objectives	3
1.2 Outline	5
2 Fundamentals in Electromagnetics	7
2.1 Maxwell's Equations	7
2.2 Constitutive Relations	8
2.3 Linear Dispersion	8
2.4 Nonlinear Dispersion	8
3 The FDTD Method	11
3.1 General Properties	11
3.1.1 The Yee Grid	11
3.1.2 The Yee Algorithm	12
3.2 Numerical Dispersion	14
3.2.1 Uniform Grids	14
3.2.2 Nonuniform Grids	16

II	Methods	19
4	Grid Generation	21
4.1	Introduction	21
4.2	Problem Definition	22
4.2.1	Definitions	23
4.3	Algorithm	26
4.3.1	Push-Pull Algorithm	27
4.3.2	Normalization	29
4.4	Analysis	30
4.4.1	Validity	31
4.4.2	Quality	32
4.4.3	Domain Grid Preprocessing	34
4.4.4	Domain Grid Generation	35
4.5	Advanced Grid Generation	36
4.5.1	Subinterval Stepping	36
4.5.2	Geometrical Analysis	37
4.5.3	Summary of Advanced Features	40
4.6	Results	43
4.6.1	Empirical Algorithm Analysis	43
4.6.2	Case Study	45
5	Lossy-Metal Modeling	53
5.1	Introduction	53
5.2	Method	54
5.2.1	The Equivalent Network Model	55
5.3	Results & Validation	56
5.3.1	Lossy Waveguide	56
5.3.2	Lossy Microstrip Filter	57
6	Thin Conductive Sheets	61
6.1	Introduction	61
6.2	Method	63
6.2.1	1D Analysis	63
6.2.2	Generalization to 3D	66
6.3	Results	72
6.3.1	Rationale	72
6.3.2	Plane Wave Verification	73

6.3.3	Canonical Shielding Benchmark	76
6.3.4	Canonical Microstrip Benchmark	80
6.3.5	Real-World Problem	80
6.4	Conclusion	80
7	Dispersive Materials	87
7.1	Introduction	87
7.2	Dispersion	88
7.2.1	Introduction	88
7.2.2	Linear Dispersion	89
7.2.3	Nonlinear Dispersion	90
7.3	ADE Algorithm	91
7.3.1	Introduction	91
7.3.2	Linear Dispersion	92
7.3.3	ADE Formulation of the Nonlinear Effects . . .	93
7.3.4	Arbitrary Dispersive Material Algorithm	94
7.4	Stability	98
7.4.1	Dispersion Relation	98
7.4.2	Phase Velocity Error	99
7.4.3	Stability and Accuracy Analysis	100
7.4.4	Fixed Point Iteration Convergence	102
7.5	Results	104
7.5.1	Four-Wave Mixing (FWM)	104
7.5.2	Solitons	105
7.5.3	Photonic Crystal Waveguide	107
7.6	Conclusion	110
III	Conclusions	115
8	Conclusion	117
9	Outlook	119
A	Dispersion Relation	121
B	List of Acronyms	123
C	List of Symbols	125

Bibliography	129
Curriculum Vitae	143

Summary

In recent years, the increased availability of cost-effective, hardware accelerated computing equipment has enabled academic and industrial simulations and research hitherto restricted to supercomputers. The finite-difference time-domain (FDTD) method in electromagnetics (EM) was one of the first methods to benefit hugely from these massively parallel computing solutions. The simple and robust structure of the method allows a very efficient parallel implementation. Processing speeds up to 50 times faster compared to single CPU computing are common, with new hardware becoming available every year.

This surge in computing power has triggered a paradigm shift. As the actual FDTD method is no longer the main bottleneck in the entire process flow, methodological improvements to the FDTD method have ceased to be the focus because they do not provide competitive alternatives to parallelized FDTD. The sheer computational power available today has shifted the focus from discretization errors and algorithmic speed improvements towards other sources of error and other bottlenecks in computation time.

The feasibility to run larger simulations in shorter times entailed applications with unprecedented levels of detail. The number of CAD objects in state-of-the-art industrial grade applications is in the order of a few hundred to a few thousand. The first link in the chain to process very complex 3D simulation configurations is the setup of a suitable FDTD grid. With the simulation time for most of these applications being just minutes, it is not desirable to invest more time in finding a suitable grid.

Chapter 4 describes the development of a novel approach to compute an FDTD grid in the shortest time possible. The approach is

based on an ultra-fast grid generation algorithm that operates on an optimized dataset containing all the relevant information about the model. The algorithm is able to compute a new grid configuration from such data within a fraction of a second. Changes in user settings are reflected in localized changes in the preprocessed grid data, which allows the grid engine to adapt the grid and the user to see the impact of his changes immediately. This feedback loop between the user and the grid engine significantly reduces the time needed to set up a grid for any given geometry. Moreover, the algorithm is designed to produce optimal grids in the sense that it tries to maximize the minimal grid step while simultaneously minimizing the total number of steps.

A direct result of being able to resolve and run structures in very high resolution is the fact that the discretization errors due to the orthogonal grid have become small compared to the influence of material modeling. Chapters 5 to 7 describe advanced material models in FDTD. All of these models have been developed against the backdrop of the requirement to work efficiently with the accelerated FDTD kernels.

For many applications, the losses in metals play a key role, and the perfect electric conductor (PEC) approximation no longer yields accurate enough results. Addressing the material group of good conductors that are difficult to model with FDTD, Chapter 5 describes the modeling of bulk metallic structures with finite conductivity and Chapter 6 describes a novel approach to modeling very thin metallic layers.

Chapter 5 describes the generalization of a surface impedance boundary condition model (SIBC) to three-dimensional structures. The model adopts an existing approach to express the frequency-dependent surface impedance with an equivalent electric network, which introduces an additional updating scheme to account for the surface impedance.

Chapter 6 introduces a novel algorithm to model the group of very thin conductive sheets with thicknesses in the range of the skin depth. Electromagnetic waves incident on such a sheet can penetrate it. It is shown that the conventional FDTD update scheme offers enough degrees of freedom to model thin conductive sheets by changing the update coefficients only. Therefore, despite a complex scheme to identify the FDTD edges that need special update coefficients, the stability

and robustness of the conventional algorithm are preserved.

An entirely different type of material is described in Chapter 7. Three-dimensional (3D) FDTD simulations in optics have traditionally been very demanding with regard to computer resources due to the small wavelengths involved. By exploiting the speed gain of the new hardware, more and more problems in this field can be investigated with FDTD. The novel scheme presented in this chapter allows the modeling of any combination of linear (Drude, Lorentz, Debye) dispersion types with the nonlinear Raman scattering and the Kerr effect. The approach retains the conventional FDTD update equations in its formulation, making efficient use of the existing hardware implementation.

Zusammenfassung

In den letzten Jahren hat die Entwicklung von auf Grafik-Prozessoren basierenden Computerkomponenten, die Hardware-Beschleunigung für spezifische Applikationen unterstützen, grosse Fortschritte gemacht. Dies ermöglicht es, heute akademische und industrielle Simulationen kostengünstig durchzuführen, die bislang Supercomputern vorbehalten waren. Die sogenannte finite-difference time-domain (FDTD)-Methode für die Simulation von elektromagnetischen (EM) Feldern war einer der ersten Anwendungsbereiche, der von diesen massiv-parallelen Rechensystemen profitiert hat. Die robuste und zugleich einfache Struktur der FDTD-Methode erlaubt eine äusserst effiziente, parallele Programmierung. Geschwindigkeitsgewinne von einem Faktor 50 oder mehr im Vergleich mit Implementationen für Einprozessor-Systeme sind erreicht worden, und jährlich wird verbesserte Hardware verfügbar.

Der plötzliche Anstieg der Rechenleistung hat zu einem Paradigmenwechsel geführt. Weil die eigentliche FDTD-Berechnung nicht länger den grössten Anteil am gesamten Zeitaufwand bei der Modellierung und Simulation eines elektromagnetischen Problems darstellt, sind methodisch verbesserte FDTD-Varianten kaum mehr konkurrenzfähige Alternativen zu den parallelisierten Systemen. Die Verbesserung der Rechengeschwindigkeit durch neue Methoden und das Problem der numerischen Ungenauigkeit bei zu groben Diskretisierungen haben an Bedeutung verloren. Bislang weniger berücksichtigte Fehlerquellen sowie andere zeitintensive Schritte bei der Simulationen-durchführung sind dagegen in den Vordergrund gerückt.

Die Möglichkeit, grössere Rechnungen in kürzerer Zeit durchzuführen, erlaubt Simulationen von nie dagewesener Komplexität und De-

tailgenauigkeit. Moderne industrielle CAD-Anwendungen können aus mehreren hundert bis mehreren tausend Einzelteilen bestehen. Der erste Schritt, um ein fertiges ComputermodeLL mit FDTD zu analysieren, ist die Erstellung eines räumlichen Gitters. Da der Zeitaufwand für die FDTD-Berechnung für viele Anwendungsgebiete im Bereich von einigen Minuten liegt, ist es nicht sinnvoll, eine grössere Zeitspanne für die Gittergenerierung zu verwenden.

Kapitel 4 beschreibt einen neuen Ansatz um FDTD-Gitter in der kürzest möglichen Zeit zu generieren. Er basiert auf einem effizienten Algorithmus, der eine optimierte Datenstruktur mit den für das Gitter relevanten Daten verarbeitet. Geänderte Parameter werden im Bruchteil einer Sekunde in Änderungen der Datenstruktur übersetzt, was einer aus Sicht des Benutzers sofortigen Aktualisierung des Gitters gleichkommt. Dieses Feedback reduziert die Zeit, welche benötigt wird, um Gitter für komplexe Simulationsmodelle zu erstellen. Darüber hinaus garantiert der Algorithmus optimale Gitter im Sinne einer Maximierung des kleinsten erzeugten Gitterschrittes und einer gleichzeitigen Minimierung der totalen Anzahl Gitterpunkte.

Eine direkte Folge der Machbarkeit von hochauflösenden Simulationen ist, dass die Diskretisierungsfehler klein sind gegenüber dem Einfluss ungenauer Materialmodellierung. Kapitel 5 bis 7 beschreiben erweiterte Materialmodelle in FDTD, welche vor dem Hintergrund einer möglichst effizienten Integration in die bestehenden hardwarebeschleunigten Systeme erarbeitet wurden.

In vielen Anwendungen spielen die Verluste von realen Metallen eine entscheidende Rolle. Die konventionelle Approximation von Metallen durch perfekt leitendes Material mit unendlicher Leitfähigkeit ist nicht länger genügend. Um die Gruppe von Materialien mit hoher Leitfähigkeit für die Analyse mit FDTD zugänglich zu machen, behandelt Kapitel 5 die Simulation von ausgedehnten Strukturen und Kapitel 6 beschreibt einen neuartigen Ansatz zur Modellierung von sehr dünnen metallischen Schichten.

Kapitel 5 beschreibt die Generalisierung und Implementation eines Oberflächenimpedanz-Modells für dreidimensionale Strukturen. Ein bestehender Ansatz, der die Oberflächenimpedanz mittels äquivalenter elektrischer Netzwerke modelliert, wurde umgesetzt und evaluiert.

Kapitel 6 führt einen neuen Algorithmus für die Simulation von sehr dünnen metallischen Schichten mit Stärken im Bereich der Skin-

tiefe ein. Elektromagnetische Wellen, die auf eine solche Schicht treffen, können diese durchdringen. Es wird gezeigt, dass die konventionellen FDTD-Gleichungen genügend Freiheitsgrade besitzen, um solche Schichten zu modellieren. Ein komplexer Algorithmus sucht und identifiziert diejenigen Feldkomponenten im FDTD-Gitter, welche mit speziellen Koeffizienten versehen werden müssen. Da dem konventionellen FDTD-Algorithmus keine neuen Gleichungen hinzugefügt sondern nur die Koeffizienten im Gitter verändert werden, bewahrt der Ansatz die Robustheit und Stabilität der FDTD-Methode.

Eine ganz andere Art von Materialien wird in Kapitel 7 behandelt. Simulationen im Bereich von optischen Anwendungen sind sehr anspruchsvoll in Bezug auf Computerressourcen aufgrund der sehr kleinen Wellenlängen. Die heute verfügbaren beschleunigten Systeme ermöglichen jedoch die Untersuchung von immer komplexeren Problemen in diesem Gebiet. Der in diesem Kapitel vorgestellte neue Algorithmus erlaubt die Simulation von wichtigen Dispersionsphänomenen. Er verbindet lineare und nichtlineare Dispersionsmodelle (Drude, Lorentz, Debye, Raman scattering, Kerr effect) und ist so formuliert, dass die konventionellen FDTD-Gleichungen Bestandteil des Algorithmus sind, um das Potenzial der hardware-beschleunigten Systeme möglichst effizient auszunutzen.

Diese Doktorarbeit besteht aus unabhängig voneinander erarbeiteten Publikationen und kann daher Wiederholungen und sich überschneidende Teile enthalten. Des Weiteren ist die Implementation der hier beschriebenen Algorithmen nicht dokumentiert, sie ist jedoch ein fester Bestandteil dieser Arbeit.

Acknowledgments

I have been fortunate to join a more than excellent software team when I started my PhD at the IT'IS Foundation in March 2005. The support and friendship I experienced from all members of this group is more than any PhD Student could hope for. First and foremost, my deepest gratitude goes toward our group leader Dr. Nik Chavannes and the foundation director Prof. Niels Kuster for giving me the chance to carry out this thesis. I especially would like to thank Nik for his excellent leadership of our group, for his always excellent scientific advice, and also for his support throughout this thesis as a friend.

It would not have been possible to complete this work without a professional academic environment, and I would like to express my gratitude to Prof. Fichtner and his staff for welcoming me in their excellent research group and for supervising my work. Also, I wish to thank Prof. Michal Okoniewski for accepting to be co-examinor of my thesis without hesitation.

This thesis was generously supported by the Swiss Commission for Technology and Innovation (CTI) and Schmid & Partner Engineering AG (SPEAG). Special thanks go to the Nokia Research Center NRC, Finland, and Motorola Electronics Private Ltd., Singapore, for providing detailed CAD data and their friendly cooperation.

Very special thanks go to all the people involved in the SEMCAD X project. In particular, I feel like I was and still am standing on the shoulders of Hansueli Gerber and Emilio Cherubini, the creators of the more than solid code basis of SEMCAD X. Hansueli managed to engineer a GUI which is both user-friendly and can easily be extended. Without it, I could not have integrated my grid engine so easily. And without Emilio's amazing coding skills, SEMCAD X

would not be able to process the level of complexity my work is intended for. Furthermore, I want to extend my thanks to my PhD colleagues Stefan Benkler, Esra Neufeld and Chung Huan Li for all the valuable discussions and their friendship. I also want to acknowledge the great work of our support and applications team: Peter Futter, Erdem Ofli, Wayne Jennings and Maria del Mar have helped me to improve my grid engine through valuable input and patient testing. Without the numerous technical and non-technical discussions with Guillermo del Castillo my world-view would not be the same, and his technical skills have saved me a lot of time otherwise wasted with non-functioning computers. I thank Francisco Nunez for his amazing optimizer package, which has greatly motivated me to further improve my griddler, and Pedro Crespo-Valero for his valuable input on various topics from MoM solvers to S-Parameters. All of them have made my PhD an enjoyable experience - thank you all.

I would also like to acknowledge that I am in the debt of Michael Ammann and Stefan Blum who have written their diploma theses with me. Their outstanding works have given my thesis the additional thrust that it needed to come to this successful end.

I also want to extend my gratitude to all the other members of IT'IS and SPEAG who have made this journey worthwhile. The administrative skills and efforts on my behalf of Jacqueline, Martin and Yvonne have been a great support. I thank Bruno, Peter, Manu and Eric who never denied help with technical issues. And I thank Judith, Andreas, Sven, Mike, Manuel, Marie-Christine and Jonathan for all the good discussion, helping hands and smiling faces. And a special thanks goes to Jane Fotheringham, who managed to read my entire thesis and correct my germanized english sentences.

My thanks also go to the excellent staff of IIS. Norbert Felber, Dölf Aemmer and Christine Haller have managed to make the administrative jungle of ETH look so easy to cross.

My deepest thanks go towards my parents for their love and care and their unwavering support on my way towards this PhD, and my sisters and nephews for brightening my days with laughter and joy.

And finally, I thank you, Monika, for all your love, and I apologize for the many times my mind was occupied with physics and math when it should have been with you. Life is a joy when you care for someone as much as I care for you.

Part I

Background

Chapter 1

Introduction

1.1 Motivation and Objectives

Since 2005 hardware acceleration based on graphics cards has been commercially available for the finite-difference time-domain (FDTD) method in the simulation of electromagnetic (EM) fields [1]. The latest systems offer a 50 fold speed gain for large simulations. This development, together with advances in personal and professional computing, has opened up a new field of problems that can be analyzed with affordable equipment.

In the FDTD process flow, consisting of model creation/import, material assignment and simulation parameter setup, grid generation, discretization, simulation, and result analysis, the simulation part has traditionally borne the largest time consumption footprint. The available speed improvements have been and still are shifting the bottleneck in this process flow to the pre- or post-processing steps, i.e., to the processing steps before and after a simulation run.

While post-processing is by and large a question of processing power, pre-processing, i.e., the grid generation and subsequent discretization, is responsible for producing valid input data for the simulation. Moreover, because the grid generation is the first step in the purely numerical part of the FDTD process flow, it depends on user knowledge specific to the model at hand. For example, in modern

applications with hundreds of CAD objects, many of the smaller dielectric parts have no significant influence on the simulation results and can be ignored during the grid process. On the other hand, radiating or scattering structures need to be identified as they may need a very fine resolution.

For all of the above reasons, the first objective of this thesis was to create a reliable grid generation framework that allows the user to inject the specific knowledge and to see its impact on the grid, while at the same time preventing him to deal with each object separately.

A second consequence of the newly available processing power is the fact that, due to the possibility of running complex simulations with very fine resolution in a reasonable time, the errors due to inaccurate material modeling have gained importance. Also, simulations in optics that were traditionally too large for FDTD, due to the very small wavelengths, are now open for investigation. For these two reasons, new and more accurate material methods need to be considered for use with FDTD. Existing approaches were not intended to run with specialized hardware equipment and their algorithmic design does not allow for efficient implementation within the framework of the available acceleration systems.

The second objective of this thesis was the development of novel material models to enhance the applicability of FDTD in general and of acceleration systems in particular.

The most important steps to achieve these goals were:

- Investigation of the requirements for a grid generation framework capable of handling the most complex simulations. Assessment of the advantages and shortcomings of existing approaches.
- Definition of quality and validity criteria for FDTD grids. Development of a primary fast grid generation algorithm following these criteria.
- Development of a novel geometrical object analysis. Enhancement of the primary grid generation algorithm to process geometrical information.
- Implementation of a complete grid generation framework. Application and testing with state-of-the-art industrial FDTD simulations.

- Literature research on existing lossy metal models and models for higher-order optical phenomena.
- Development and implementation of a novel material models for optical media, bulk lossy metallic structures, and thin conductive sheets with focus on an efficient implementation within the framework of hardware accelerated systems.
- Benchmarking of the material models with generic and real-world examples.

1.2 Outline

The remaining chapters of this thesis are outlined as follows:

Chapter 2 introduces Maxwell's theory as foundation of the developed methods in this thesis. Also, the fundamental theory behind the linear and nonlinear dispersion models are discussed.

Chapter 3 reviews properties of the FDTD algorithm including the influence of the discretization. The basic principles and current state of the FDTD acceleration platform used throughout this thesis are also summarized.

Chapter 4 defines the quality requirements for an FDTD grid and the primary grid generation algorithm developed to meet these goals. The advanced methods used in the final implementation are described along with generic and real-world benchmarks and examples.

Chapter 5 reviews the surface impedance models and explains the generalization to arbitrary 3D structures. The validity of the model is illustrated with benchmarks.

Chapter 6 describes the approach and algorithm to model thin conductive sheets with the conventional FDTD stencil. A range of generic benchmarks shows the accuracy of the model. The application of the algorithm to a real-world example is described, where a former discrepancy between measurement and simulation was able to be resolved.

Chapter 7 describes the details of a novel arbitrary dispersive material (ADM) algorithm. The stability considerations are discussed, and computational examples and benchmarks are presented.

Chapter 2

Fundamentals in Electromagnetics

2.1 Maxwell's Equations

Classically, the electromagnetic field is described by Maxwell's equations [2]

$$\nabla \times \mathbf{E} = -\frac{\partial \mathbf{B}}{\partial t} \quad (2.1a)$$

$$\nabla \times \mathbf{H} = \frac{\partial \mathbf{D}}{\partial t} + \mathbf{j} \quad (2.1b)$$

$$\nabla \cdot \mathbf{D} = \rho \quad (2.1c)$$

$$\nabla \cdot \mathbf{B} = 0. \quad (2.1d)$$

The electric current density \mathbf{j} is connected to \mathbf{E} via Ohm's law (where valid, i.e., at sufficiently low intensities)

$$\mathbf{j} = \sigma \mathbf{E} \quad (2.2)$$

where σ is the electric conductivity.

2.2 Constitutive Relations

In a dielectric medium, the constitutive equations can be written as

$$\mathbf{D} = \mu \mathbf{E} = \mu_0(\mathbf{E} + \mathbf{P}) \quad (2.3a)$$

$$\mathbf{B} = \mu \mathbf{H} = \mu_0(\mathbf{H} + \mathbf{M}) \quad (2.3b)$$

where \mathbf{P} is the electric polarization and \mathbf{M} is the magnetization [2, 3]. Except for specific types of magnetic materials, the magnetization \mathbf{M} is a linear and isotropic function of \mathbf{H} . For a linear, isotropic, and non-dispersive material, the same holds true for the polarization \mathbf{P} , which becomes a linear function of \mathbf{E} .

To investigate higher order polarization effects, the polarization can be described in the frequency domain with

$$P_i = \epsilon_0 \left(\sum_{ij} \chi_{ij}^{(1)} E_j + \sum_{ijk} \chi_{ijk}^{(2)} E_j E_k + \dots \right) \quad (2.4)$$

where the $\chi^{(n)}$ are dielectric susceptibility tensors of rank $n + 1$ [3].

2.3 Linear Dispersion

Ignoring the higher order terms in the series on the right hand side of Equation (2.4) yields a polarization \mathbf{P} that depends linearly on \mathbf{E} . Frequency dependent first order susceptibilities $\chi^{(1)}(\omega)$ give rise to linear dispersion, where the term linear refers to the linearity of \mathbf{P} in \mathbf{E} .

The frequency dependence can take different forms depending on distinct physical phenomena. Commonly, the Drude, Debye, and Lorentz models are used to describe linear dispersion. A thorough discussion of these models and their physical foundation can be found in [3] or [4].

2.4 Nonlinear Dispersion

The higher-order terms on the right hand side of Equation (2.4) yield a polarization \mathbf{P} that depends non-linearly on \mathbf{E} .

In centrosymmetric materials, the second-order susceptibility $\chi^{(2)}$ must vanish (cf. [3]). The approach presented in Chapter 7 models the third order Kerr effect and Raman scattering.

The Kerr effect modeled by this approach is the constant, isotropic, and instantaneous third order response $\chi^{(3)} = \chi_0^{(3)}$, and its polarization contribution is given by

$$\mathbf{P}_{Kerr}(t) = \epsilon_0 \chi_0^{(3)} |\mathbf{E}(t)|^2 \mathbf{E}(t). \quad (2.5)$$

On the other hand, the Raman scattering model accounts for non-resonant phonon interaction. It describes a single Lorentzian line centered on the optical phonon frequency $1/\tau_1$ with a bandwidth of $1/\tau_2$, the reciprocal phonon lifetime. The susceptibility response and polarization contribution due to Raman scattering are given by

$$\chi_{Raman}^{(3)}(t) = \chi_0^{(3)} \frac{\tau_1^2 + \tau_2^2}{\tau_1^2 \tau_2^2} e^{-\frac{t}{\tau_2}} \sin\left(\frac{t}{\tau_1}\right) H(t) \quad (2.6a)$$

$$\mathbf{P}_{Raman}(t) = \epsilon_0 \mathbf{E}(t) \left[\chi_{Raman}^{(3)}(t) * |\mathbf{E}(t)|^2 \right] \quad (2.6b)$$

where H is the Heaviside function.

The Kerr effect is a frequency-independent, intensity-dependent contribution to the permittivity. Despite its simple mathematical description, its effects are complex. The strength of the Kerr effect depends on the local field intensity and amplitude. Thus, different parts of a light-pulse are affected differently. Depending on the sign of the susceptibility $\chi_0^{(3)}$, the Kerr effect is either focusing or defocusing. In a well balanced case, it is possible that pulse-broadening due to linear dispersion is neutralized by the Kerr effect such that the light pulse retains its shape. Such pulses are called solitons, and some illustrative results are shown in Section 7.5.2.

For nonresonant electronic nonlinearities, the third-order susceptibility $\chi^{(3)}$ can be expected to be of the order of $1/E_{at}^2$, where E_{at} is the characteristic atomic electric field strength $E_{at} = 1/(4\pi\epsilon_0) \cdot e/a_0^2$ of the hydrogen atom with Bohr radius a_0 [3]. Using Equation 2.4 as a definition for the susceptibilities, numerical values in the MKS system for the third order susceptibility are expected to be in the order of

$$\chi^{(3)} \cong 4 \times 10^{-23} \frac{\text{m}^2}{\text{V}^2}. \quad (2.7)$$

However, values for materials showing electronic nonlinearities can be up to 5 orders of magnitude larger, as shown in Table 2.1.

Table 2.1: Nonlinear optical susceptibilities for materials showing electronic nonlinearities. Adapted from [5].

Material	$\chi^{(3)}$ [m^2/V^2]
Diamond	21×10^{-22}
Yttrium aluminum garnet	8.4×10^{-22}
Sapphire	4.2×10^{-22}
Borosilicate crown glass	3.5×10^{-22}
Fused silica	2.8×10^{-22}
CaF_2	2.2×10^{-22}
LiF	1.4×10^{-18}

Chapter 3

The FDTD Method

The origin of the FDTD method to solve EM problems dates back to the paper by Kane S. Yee in 1966 [6]. Yee created a gridding scheme where each point of the grid represents a component of the E or H-field in one of the Cartesian directions. His insight was to arrange the components in a way such that each E-field component is surrounded by four H-field components in the complementary two directions, and vice versa. The four surrounding field components can be interpreted as representing the path integral along a rectangle around the central component, the integral being a finite approximation of the rotation operator. Therefore, the Yee scheme can be seen as a collection of finite rotation operators, optimally arranged into a symmetric distribution of the six E and H-field components, optimally matched to the rotation character of Maxwell's equations. Therein lies one of the keys to the robustness of the FDTD scheme, which in turn is the reason that, more than four decades after its conception, the method is still the tool of choice for a wide range of applications.

3.1 General Properties

3.1.1 The Yee Grid

Figure 3.1 shows a single Yee cell with the E-field components on the edges and the H-field components on the faces of the cell. Each cell in

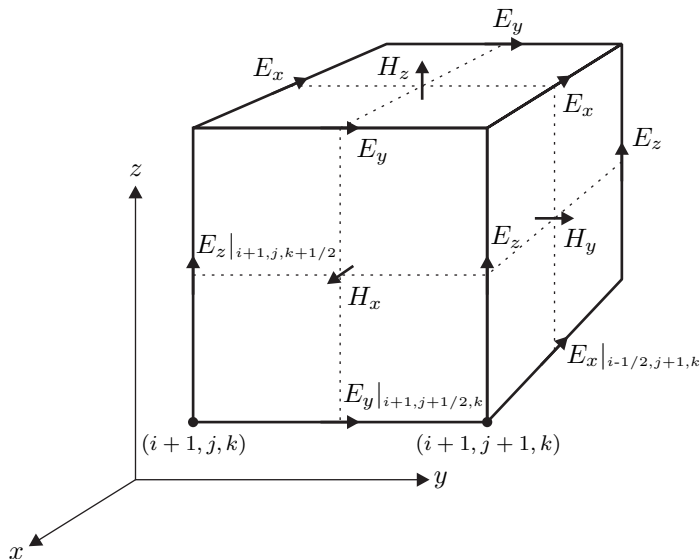


Figure 3.1: Yee cell with E-field components on the edges and H-field components on the faces.

an FDTD grid is numbered by a three-dimensional index (i, j, k) . Each E-field component is offset by half a grid step in the direction that it inscribes, as in, for example, $E_x|_{i-1/2, j, k}$. Each H-field component is offset by half a grid step in its complementary directions, as in $H_x|_{i, j+1/2, k+1/2}$.

Analogously, the temporal axis is discretized with a time step Δt . The E-field components are computed and stored at the full steps $n \cdot \Delta t$, and the H-field components are computed and stored at the intermediate steps $(n + 1/2) \cdot \Delta t$.

3.1.2 The Yee Algorithm

Using the finite-difference approximation of a derivative

$$\frac{\partial}{\partial k} F(k = n\Delta k) = \frac{F([n + 1/2]\Delta k) - F([n - 1/2]\Delta k)}{\Delta k}, \quad (3.1a)$$

Maxwell's Equations (2.1a) and (2.1b) can be rewritten to find the FDTD update equations

$$E_x|_{i+1/2,j,k}^{n+1} = \alpha_E \cdot E_x|_{i+1/2,j,k}^n + \beta_E \cdot \left(\frac{\Delta H_z|_{i+1/2,j\pm 1/2,k}^{n+1/2}}{\Delta y_j^H} - \frac{\Delta H_y|_{i+1/2,j,k\pm 1/2}^{n+1/2}}{\Delta z_k^H} \right) \quad (3.2a)$$

$$H_x|_{i,j+1/2,k+1/2}^{n+1/2} = \alpha_H \cdot H_x|_{i,j+1/2,k+1/2}^{n-1/2} - \beta_H \cdot \left(\frac{\Delta E_z|_{i,j+1/2\pm 1/2,k+1/2}^n}{\Delta y_j^E} - \frac{\Delta E_y|_{i,j+1/2,k+1/2\pm 1/2}^n}{\Delta z_k^E} \right) \quad (3.2b)$$

where the contracted notation $\Delta F|_{i,j\pm 1/2,k}^n$ denotes the difference between the field values $F|_{i,j+1/2,k}$ and $F|_{i,j-1/2,k}$, and Δ_i^E and Δ_i^H denote the local spatial steps. The distinction between the grid steps for the E and H-field updates is necessary when a nonuniform grid is used (cf. Section 3.2.2). Analogous update equations for the remaining four components can be obtained by permuting the axis indices $x \rightarrow y \rightarrow z \rightarrow x$.

Using exponential time-differencing (ETD) (cf. [7]) the update coefficients are

$$\alpha_E = \exp\left(-\frac{\sigma \Delta t}{\epsilon}\right) \xrightarrow{\sigma \rightarrow 0} 1 \quad (3.3)$$

$$\beta_E = \frac{1 - \alpha_E}{\sigma} \xrightarrow{\sigma \rightarrow 0} \frac{\Delta t}{\epsilon} \quad (3.4)$$

$$\alpha_H = 1 \quad (3.5)$$

$$\beta_H = -\frac{\Delta t}{\mu}. \quad (3.6)$$

Although these update coefficients yield a stable algorithm for all conductivities, an FDTD grid would have to resolve the skin-depth

and wavelength for highly conductive materials. This is usually not feasible because the resulting grid steps would become extremely small compared to the wavelength of interest. Thus, for conductivities above approx. 1000 S/m, surface impedance models, as described in Chapter 5, are required to make such simulations feasible.

It can be shown that the Yee-Algorithm, although it is derived from Equations 2.1a and 2.1b, inherently upholds the divergence free nature in a charge free region (see, for example, [8]).

Also, the algorithm is conditionally stable with the stability limit

$$\Delta t \leq \min_{\text{Yee Cells}} \left\{ \frac{\sqrt{1/(\epsilon\mu)}}{\sqrt{1/(\Delta x)^2 + 1/(\Delta y)^2 + 1/(\Delta z)^2}} \right\}, \quad (3.7)$$

which coincides with the Courant-Friedrichs-Lewy (CFL) criterion [9]. In many applications, the smallest grid steps are approximately equal along all axes. In this case, and if those minimal steps can be found in the same material, Equation (3.7) can be approximated by

$$\Delta t \approx \frac{\Delta x}{\sqrt{3}\sqrt{\epsilon\mu}}, \quad (3.8)$$

which reveals an linear relationship between time step and grid step. Thus, in the worst case, refining the grid by a factor r can cause an r^4 increase in computational resources needed to complete the simulation. It is therefore imperative to avoid any unnecessary overdiscretization.

3.2 Numerical Dispersion

Equation (A.14) describes the relation between the numerical wave vector \mathbf{K} and the numerical frequency Ω in the Yee grid. By choosing a fixed frequency ω and/or a fixed wave vector \mathbf{k} , one can solve for their respective numerical counterparts.

3.2.1 Uniform Grids

The dispersion error has been thoroughly analyzed in a range of publications [10, 11, 12, 13, 14, 15].

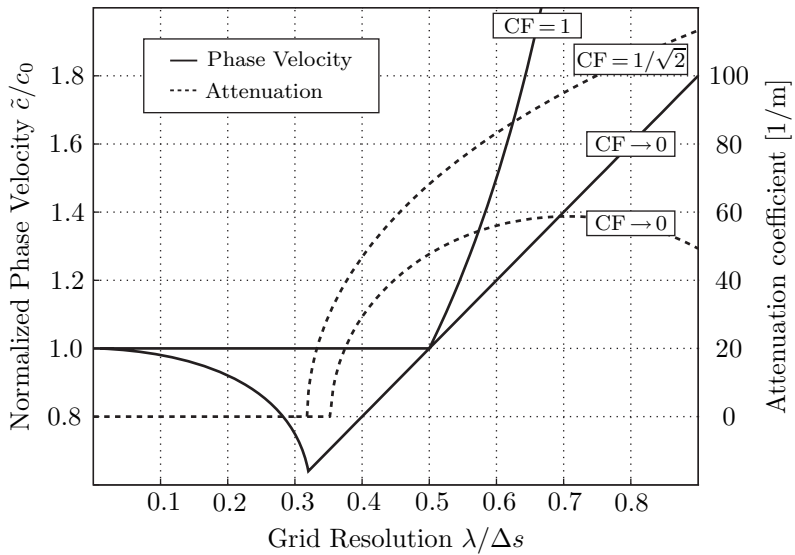


Figure 3.2: Numerical phase velocity and spurious attenuation of the Yee algorithm as a function of the uniform grid resolution for different Courant factors (CF).

Figure 3.2 shows the phase velocity and the attenuation coefficient as functions of the grid resolution for different Courant factors (CF), defined by $CF = \Delta t / \Delta t_{\max}$, for wave propagation along a major grid axis, taken from [14, 16]. Also, the dispersion error was found to be below 1% for any incident angle for a wavelength resolution of $\lambda/10$ or less [15].

Generally, a grid resolution of

$$\Delta x \leq \frac{\lambda}{10} \quad (3.9)$$

is considered to yield sufficiently accurate results. However, the required accuracy depends heavily on the application, and a grid generation engine must be able to process any chosen wavelength resolution factor for any material.

3.2.2 Nonuniform Grids

State-of-the-art FDTD applications can not be modeled using uniform grids. The necessary resolution of fine structures would produce grids too large to be processed.

A range of error sources are present in nonuniform FDTD [17, 18]. First, the second-order central difference approximation is lost because the grid steps Δi^E in Equation (3.2b) need to be averaged over two adjacent cells. Although the global second order accuracy is preserved [19], locally first order errors influence the overall uncertainty depending on the grading ratio and cell size. Despite the loss in accuracy, nonuniform grids clearly outperform uniform grids in almost all applications as long as the grid resolution limit (3.9) is satisfied throughout the grid [15, 20, 21, 22]. A range of approaches has been proposed to improve the error in nonuniform grids [15, 23, 24, 25, 26]. Another source of error in nonuniform grids is an increased dispersion error.

Finally, the orthogonal gridding used in the Yee scheme results in a staircased representation of curved structures. The staircasing of perfect electric conductors (PEC) such as antennas and waveguides can have a significant impact on the accuracy of the simulation [27, 28, 29, 30]. An summary and overview of the possible side-effects of staircasing in FDTD can be found in [31]. In the case of PEC objects,

it has been found that, aside from the need to meet the wavelength resolution criterion (3.9), tilted PEC planes should be resolved such that the diagonals of the FDTD cells at the object boundaries are bounded to

$$\Delta x \leq \lambda/2. \quad (3.10)$$

An advanced grid generation algorithm should be able to process the geometry of critical structures in order to ensure a sufficiently fine resolution for conducting bodies and, if necessary, dielectric objects that have a significant impact on the simulation accuracy. A rigorous approach to allow for an optimal gridding of such structures is presented in Chapter 4.

Part II

Methods

Chapter 4

Grid Generation

4.1 Introduction

Grid generation in FDTD is the process of creating a nonuniform spatial grid in three dimensions that satisfies the necessary numerical and geometrical constraints. Most importantly, different material models demand certain restrictions as to how large the distance between the discrete field components (grid step) can become. Also, the geometry may require the grid to be refined for very fine or curved structures.

The first FDTD applications using nonuniform grids were reported in the late 70s. The scheme was successfully applied to EM problems in the fields of Radar Cross Section (RCS) assessment [32, 33], low frequency scattering problems [34], waveguide structures [21, 35, 22, 36], numerical dosimetry [37, 38, 39], antenna analysis [40, 41], and optics [42, 43]. All of these applications have demonstrated that the savings in computational resources by graded meshes clear outweigh decreased accuracy [20, 44].

Empirically derived rules for appropriate grid generation in FDTD have been published by [44, 45, 46]. The effect of a graded grid on the dispersion error in FDTD simulations has been thoroughly analyzed in [15]: Firstly, the dispersion error is increased because the time step for most cells is smaller than the CFL limit. Secondly, the grading introduces spurious amplification and attenuation. In practice, a

grading ratio of 1.2 and a maximal step size of $\lambda/10$ have proved to be a good compromise between accuracy loss and simulation speedup due to a reduction in grid size.

Several approaches to automating the grid generation to a certain degree have been published [47, 48, 23]. However, none is designed to handle to complexity of modern FDTD applications, and they do not offer the necessary level of control over the grid generation process.

One of the foremost challenges for modern FDTD solutions is the processing of very complex models. State-of-the-art models can contain hundreds of different 3D parts with distinct material properties. For example, simulations involving human phantoms are nowadays performed routinely with the phantom containing about 100 dielectric tissue parts. Together with the radiating structures of interest, such as on-body or in-body antennas, MRI coils, mobile phones, etc., the complexity reaches a level where it is no longer possible to set up the grid parameters for each model part manually in a reasonable time. On the other hand, these models require detailed knowledge of the simulation to set up the grid properly. Questions, such as which model parts have the largest influence on radiation and scattering patterns, are known only to the user and cannot be automatically detected. Therefore, user interaction with the grid engine is unavoidable in order to create and verify a reliable discretization of a model.

The approach presented is designed to minimize the time needed for the user to set up a suitable grid. It is based on an ultra-fast grid engine that computes the grid interactively, where interactivity means that changes in user interface settings are immediately reflected in a new grid configuration, i.e., typically within fractions of a second. The typical trial and error phase during grid setup, which is in essence the process of incorporating the specialized user knowledge into the grid setup, can be shortened considerably with this approach.

4.2 Problem Definition

In all FDTD models¹, a certain number of points in space can be identified so that the three grid axes contain elements to match their

¹Even for an empty simulation, the domain boundaries can serve as two fixed points.

components, i.e., where a grid without a point at that location is not suitable for the model at hand. Examples of entities to require such special points are excitation sources, sensors, or sharp boundaries of radiating structures. The existence of such fixed points or baselines is the rationale behind the approach of splitting a grid axis into distinct regions and to apply a grid algorithm to each region separately.

The FDTD-grid engine has to fill the regions with grid points while satisfying the constraints inside and across their boundaries. The spatial axes are interdependent only with regard to the constraints originating from geometrical features and material types. However, these preconditions are themselves not dependent on the grid configurations, and the three axes of an FDTD grid can thus be independently generated.

The two major constraints that need to be satisfied are the wavelength resolution and the grading ratio. Different materials exhibit different wavelengths in the frequency band of interest, and it is necessary to resolve all wavelengths that can occur in a simulation with a certain number of grid steps to ensure sufficient accuracy. On the other hand, the grid stepping between regions of different wavelengths should not vary too quickly and the concept of capturing this requirement is to introduce a grading ratio (cf. Definitions 2 and 4).

A good grid engine satisfies all the numerical restrictions while finding an optimal solution in terms of grid size. Because of the stability constraints in FDTD, the smallest grid step is linked to the time step of the simulation. Thus, an FDTD simulation can be large not only in its three spatial but also in the temporal dimension, i.e., a very small spatial step can induce a very small time step. A grid engine must try to keep the grid “small” in the spatial domain by producing a minimal number of cells, and also in the time axis by keeping the smallest cell as large as possible.

4.2.1 Definitions

A few definitions are necessary to facilitate the description and analysis of the presented algorithm. For completeness, the frequently used terms grid point and baseline are defined first.

Definition 1 (Basic Definitions). *A **grid point** or **grid line** is a*

coordinate of an edge of a cell of the primary orthogonal FDTD Yee-grid (cf. [8]). A **baseline** is a given grid point that can neither be moved nor removed² during the grid generation.

Definition 2 (Region). A **region** R is a set of numbers

$$\begin{aligned} R &= \{a_0, b_0, g, \Delta g, \Delta a_0, \Delta b_0\} \in \mathbb{R}^6, \\ b_0 &> a_0, \quad g > 1, \\ 0 &< \Delta g \leq b_0 - a_0, \\ 0 &< \Delta a_0 \leq b_0 - a_0, \quad 0 < \Delta b_0 \leq b_0 - a_0, \end{aligned} \tag{4.1}$$

where a_0 and b_0 are the **region boundaries**, g is the **grading ratio**, Δg is the **maximal step**, and Δa_0 and Δb_0 are the **boundary steps**.

Essentially, a region describes an interval bounded by two baselines along with the local grid constraints or parameters. The meanings of the grading ratio, the maximal step, and the boundary steps are developed in Definition 4.

Definition 3 (Grid). A **Grid** G is a set of $n + 1$ points

$$\begin{aligned} G &= \{p_0, \dots, p_n\} \in \mathbb{R}^n, \\ p_{k+1} &> p_k \quad \forall k, 0 \leq k < n. \end{aligned} \tag{4.2}$$

The **intervals** or **steps** Δp_k are the n distances between adjacent grid points

$$\Delta p_k = p_{k+1} - p_k \quad \forall k, 0 \leq k < n. \tag{4.3}$$

Without further restrictions, any strictly monotone series of real numbers is a grid. Definition 4 now introduces the constraints necessary for a grid to be used in an FDTD simulation.

Definition 4 (Regional Grid). A **regional grid** M is a grid to a region R where the following conditions are satisfied:

$$\begin{aligned} p_0 &= a_0, \quad p_n = b_0, \\ \Delta p_0 &\leq \Delta a_0, \quad \Delta p_{n-1} \leq \Delta b_0, \\ \Delta p_k &\leq \Delta g \quad \forall k, 0 \leq k < n, \\ g^{-1} &\leq \frac{\Delta p_{k+1}}{\Delta p_k} \leq g \quad \forall k, 0 \leq k < n - 1. \end{aligned} \tag{4.4}$$

²Note that baselines can not be removed during grid generation, but they can be removed during preprocessing, cf. Section 4.4.3.

Definitions 3 and 4 describe the nature of an FDTD grid. The maximal step usually originates from the need to resolve the wavelength inside some material. The distance between region boundaries and their neighboring grid points is limited by the boundary steps. The most important part of this section is Definition 5:

Definition 5 (Optimal Regional Grid). *A regional grid is **optimal** with respect to its region if a) there is no other regional grid that has fewer grid points, and b) there is no other regional grid whose smallest interval is larger.*

An optimal grid combines the two goals of having a grid which is as small as possible, both in terms of spatial and temporal steps. The latter is reflected in the need to maximize the smallest step in a regional grid.

Clearly, the boundary steps can safely be assumed to be smaller than the maximal step. If they were larger, they would have been overridden by the maximal step to be met in the entire region.

Definition 6 (Domain). *A **domain** is a set of m regions and a grading relaxation constant g_r*

$$D = \{R_0, \dots, R_m, g_{relax}\}, \quad m \geq 1, \quad (4.5)$$

$$g_{relax} \in \mathbb{R}, \quad g_{relax} \geq 1,$$

where

$$b_0|_{R_k} = a_0|_{R_{k+1}} \quad \forall k, 0 \leq k < m,$$

$$\max_{i=k, k+1} \left\{ \frac{1}{g_{relax} \cdot g|_{M_i}} \right\} \leq \frac{\Delta b_0|_{R_k}}{\Delta a_0|_{R_{k+1}}} \quad \forall k, 0 \leq k < m, \quad (4.6)$$

$$\min_{i=k, k+1} \{g_{relax} \cdot g|_{M_i}\} \geq \frac{\Delta b_0|_{R_k}}{\Delta a_0|_{R_{k+1}}} \quad \forall k, 0 \leq k < m.$$

Definition 6 ensures that a relaxed grading ratio is satisfied across region boundaries. Regions can, by definition, have distinct grading ratios. Because any grid that satisfies a grading ratio g also satisfies any larger grading ratio $g' > g$, only the smaller of the two has to be considered.

The grading relaxation g_{relax} , with typical values of approx. 1.1 or 10%, plays an important role in the creation of domain grids, and is described in Section 4.4.4.

A domain describes an entire one-dimensional interval that encompasses the FDTD model on one of the axes. An FDTD grid engine is presented with three domains, one for each axis, as input data. The creation of the axial domains is part of the preprocessing and is described in Section 4.4.3.

Finally, the definition of a grid for an entire domain wraps up the list of definitions:

Definition 7 (Domain Grid). *A **domain grid** DM of a domain D is a set of m regional grids*

$$DM = \{M_0, \dots, M_m\}, \quad m \geq 1, \quad (4.7)$$

where the M_k are valid grids of their corresponding regions R_k in D .

Because the definition of a domain D already enforces the necessary constraints across the region boundaries, Definition 7 is a complete definition of a valid grid along one axis. The following section contains some additional definitions as they arise in the investigation of the grid algorithm.

4.3 Algorithm

The innermost part of the grid algorithm is described in this section. It is responsible for computing the regional grids. The algorithm, by design optimized for speed, avoids higher mathematical functions of any sort and relies on the most simple floating point operations only. Moreover, it attempts to create an optimal grid directly, as opposed to searching iteratively for a solution.

The solutions computed by the presented algorithm might be obtained by other methods. However, the most important advantage of the presented approach is that it can be augmented to provide advanced methods to further optimize a grid. These methods are discussed in Section 4.5.

Figuratively, the regional grid is created by pushing the lower region boundary a_0 stepwise toward the upper boundary b_0 , and by

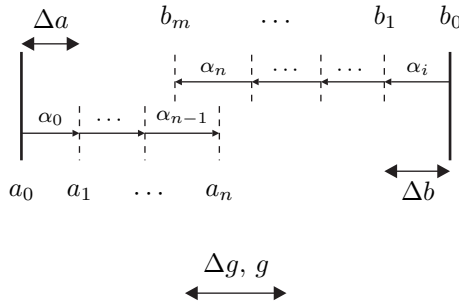


Figure 4.1: Grid region with fixed boundaries (baselines) a_0 and b_0 . The region is filled from both boundaries with the grid line sets a_0, \dots, a_n and b_0, \dots, b_m , respectively, until the sets overlap.

pulling b_0 toward a_0 , respectively, until the two points pass each other. Then, the two sets of intervals created are normalized such that the two last points of each set meet.

4.3.1 Push-Pull Algorithm

Figure 4.1 depicts the intermediate situation for a region R . It is bounded by its baselines a_0 and b_0 , respectively. The goal is to find two sets of points

$$A = \{a_0, \dots, a_n\} \text{ and } B = \{b_0, \dots, b_m\}, \quad (4.8)$$

$$n, m \geq 0, \quad a_{k+1} > a_k, \quad b_{k-1} > b_k,$$

that satisfy the following conditions:

$$\begin{aligned} a_0|_A &= a_0|_R, & b_0|_B &= b_0|_R, & a_n &\geq b_m, \\ \Delta a_0|_A &\leq \Delta a_0|_R, & \Delta b_0|_B &\leq \Delta b_0|_R, \\ \frac{1}{g} &\leq \frac{\Delta a_{k+1}}{\Delta a_k} \leq g & \forall k, 0 &\leq k < n, \\ \frac{1}{g} &\leq \frac{\Delta b_{k+1}}{\Delta b_k} \leq g & \forall k, 0 &\leq k < m, \\ \Delta a_k &\leq \Delta g & \forall k, 0 &\leq k < n, \\ \Delta b_k &\leq \Delta g & \forall k, 0 &\leq k < m. \end{aligned} \quad (4.9)$$

Definition 8 (Intermediate Sets). *The sets A and B described above are called **intermediate sets** of the grid M and they combine to form the **intermediate grid** $\tilde{M} = \{A, B\}$, where A is its **left-hand set** and B its **right-hand set**.*

An example situation of two intermediate sets filling a region is shown in Figure 4.1. The push-pull algorithm to construct such an initial configuration consists of the following steps:

- A) The initial sets of grid points are given by: $A^{(0)} = \{a_0\}$ and $B^{(0)} = \{b_0\}$.
- B) For two sets of points $A^{(i)}$ and $B^{(j)}$ compute the maximal next step for each of the sets given by

$$\Delta a_{\max} = \begin{cases} \min\{\Delta g, \Delta a_0\} & \text{if } i = 0 \\ \min\{\Delta g, g \cdot (a_i - a_{i-1})\} & \text{if } i > 0 \end{cases} \quad (4.10)$$

$$\Delta b_{\max} = \begin{cases} \min\{\Delta g, \Delta b_0\} & \text{if } j = 0 \\ \min\{\Delta g, g \cdot (b_{j-1} - b_j)\} & \text{if } j > 0 \end{cases}$$

- C) Choose the smaller of the two steps Δa_{\max} and Δb_{\max} and add an additional point to the corresponding set, i.e., $A^{i+1} = A^i \cup (a_i + \Delta a_{\max})$ or $B^{j+1} = B^j \cup (b_j - \Delta b_{\max})$, thereby increasing i or j by one. If the two steps are equal, choose a side at random.
- D) Stop if the largest element of set A is larger than or equal to the smallest element of set B . Otherwise, repeat Step B with the new sets.

It is easy enough to see that the push-pull algorithm described above terminates for every region. The intermediate sets A and B are divergent series, because the grading ratio, by definition, can not be smaller than 1. A simple boundary for the maximal number of iterations I_{\max} can readily be given by

$$I_{\max} \leq \frac{b_0 - a_0}{\min\{\Delta a_0, \Delta b_0, \Delta g\}}. \quad (4.11)$$

4.3.2 Normalization

An equivalent description of the sets A and B is given by defining a set of intervals normalized to a positive grid step Δs

$$I = \{\alpha_0, \dots, \alpha_{i=n+m-1}\} \quad (4.12)$$

through

$$\alpha_k = \begin{cases} \frac{a_{k+1} - a_k}{\Delta s} & \text{if } 0 \leq k < n \\ \frac{b_{m+n-k-1} - b_{m+n-k}}{\Delta s} & \text{if } n \leq k < m+n \end{cases} \quad (4.13)$$

as depicted in Figure 4.1. The **excess length** S is defined by

$$S = \sum_{k=0}^{m+n-1} (\alpha_k - 1) \Delta s. \quad (4.14)$$

If Δs is chosen to be equal to the smallest interval in A and B , the excess length describes the amount by which the interval sum $\sum_0^{m+n-1} \alpha_k \Delta s$ can be reduced such that it is still larger than the region without compromising the grading or stepping requirements.

In order to find a valid set of grid points that satisfy Definition 4, the interval description I is renormalized writing

$$\tilde{\alpha}_k = 1 + (\alpha_k - 1)Q \quad (4.15)$$

with the renormalization factor

$$Q = 1 - \frac{a_n - b_m}{S}. \quad (4.16)$$

The sum of the renormalized intervals $\tilde{\alpha}_k$ writes

$$\begin{aligned}
\sum_{k=0}^{m+n-1} \tilde{\alpha}_k \Delta s &= \sum_{k=0}^{m+n-1} [1 + (\alpha_k - 1)Q] \Delta s = \\
&= \sum_{k=0}^{m+n-1} \left[1 + \alpha_k - 1 - \frac{a_n - b_m}{S} (\alpha_k - 1) \right] \Delta s = \\
&= \sum_{k=0}^{m+n-1} \alpha_k \Delta s - \Delta s \sum_{k=0}^{m+n-1} \frac{a_n - b_m}{S} (\alpha_k - 1) = \\
&= (b_0 - a_0) + (a_n - b_m) - (a_n - b_m) = b_0 - a_0, \quad (4.17)
\end{aligned}$$

which is exactly the initial interval to be gridded.

Employing this normalization/renormalization routine, the last step of computing the final grid lines inside the interval is given as follows:

- Normalize the constructed set of overlapping grid lines to the smallest grid step Δs found in both intermediate sets.
- If the resulting renormalization factor Q is positive, i.e., if $S > (a_n - b_m)$, the final grid points are given iteratively by

$$p_0 = a_0, \quad p_{k+1} = p_k + \tilde{\alpha}_k \Delta s. \quad (4.18)$$

- If Q is negative, the normalization step Δs needs to be compromised in order to fill the interval. In that case, the region is split into $m + n - 1$ uniform intervals.

4.4 Analysis

Having established a regional grid generation algorithm that terminates for every region, the question remains whether its output is always a regional grid and, if it is, whether it is optimal according to Definition 5. The first question is answered in Section 4.4.1, and the second question in Section 4.4.2.

4.4.1 Validity

Theorem 1. *A grid M created with the push-pull algorithm is a regional grid.*

Proof. In order for M to be a regional grid, it has to be shown that the set p_k created by the push-pull algorithm satisfies Definition 4.

The first two requirements, namely $p_0 = a_0$ and $p_n = b_0$ are trivial, because a_0 and b_0 are by definition equal to the region boundaries, p_0 is by definition equal to a_0 , and with the sum of all intervals described by the p_k equal to $b_0 - a_0$ as shown in Equation (4.17), it follows immediately that $p_n = b_0$.

The boundary step conditions $\Delta p_0 \leq \Delta a_0$ and $\Delta p_{n-1} \leq \Delta b_0$ are satisfied. This follows directly from Equation (4.10) and the following consideration: It is not possible for either the left-hand or the right-hand intermediate set to surpass the opposite region boundary with a step larger than the boundary step because, in such a case, the push-pull algorithm would have chosen to add a step to the opposite intermediate set, thus enforcing the boundary step.

The regional step constraint $p_{k+1} - a_k \leq \Delta g|_R$ is clearly satisfied because of Equations (4.10), (4.15), (4.16), and (4.18). The normalization factor Q can not be larger than 1. Therefore, the final intervals $\hat{\alpha}_k \Delta s$ can not be larger than the intermediate intervals computed by the push-pull algorithm, and the latter are, by Equation (4.10), strictly bounded to Δg .

The grading ratio g is enforced throughout the grid: From Equation (4.10) follows that the ratio of two adjacent intervals in an intermediate set can be written as a function of Q : $g(Q) = (1 + Q(\alpha - 1))/(1 + Q(\beta - 1))$. Q is by definition in the range $0 < Q \leq 1$ and one can assume without loss of generality that $\alpha > \beta > 1$. Clearly, $g(Q)$ is a monotonously increasing function in Q . This directly shows that the normalization process can only decrease the grading ratio between adjacent intervals, because Q decreases during the renormalization process from 1 to some value smaller than 1.

It remains to be shown that the grading ratio is satisfied between the last intervals of both intermediate sets. The trivial cases where either A or B has only one element is easily dismissed, because in that case the grading ratio can not be violated as the intervals have grown from one side only. Now, let both intermediate sets have more than

one element. One can look at the last intervals created in both sets α_n in A and β_m in B . Without loss of generality, let α_n be larger than β_m , which implies that β_m was created last.

Now, let α_n be larger than $g \cdot \beta_m$, which would violate the grading ratio. This implies that α_{n-1} (or the boundary step if $n = 1$) is larger than β_m , because of the grading ratio g . But then, α_{n-1} is larger than all the intervals in B , which would have prevented α_n from being added to A in the first place. Thus, α_n cannot be larger than $g \cdot \beta_m$, and the grading ratio is always satisfied. \square

4.4.2 Quality

Theorem 2. *For a region R that satisfies Definition 2 and a regional grid M created with the push-pull algorithm, there is no other regional grid M' that satisfies Definition 4 with $n|_{M'} < n|_M$.*

Proof. Let M' be an arbitrary regional grid according to Definition 4, and let M be a regional grid created with the push-pull algorithm and \tilde{M} its intermediate grid. The number of intervals in the left-hand set A of \tilde{M} is denoted by n and the number of intervals in the right-hand set B of \tilde{M} by m .

Clearly, because of the definition of the push-pull algorithm, there can be no other series $a'_0, \dots, a'_{n'}$ with $a'_{n'} = a_n$ and $n' < n$ that fulfills the requirements of Definition 4. This is because the series created by the push-pull algorithm starts by definition with the largest possible initial step and grows with the maximally possible grading ratio. A completely analogous derivation holds for the right-hand series B .

The trivial cases where either $n = 0$ or $m = 0$ are now easily proved, for it follows directly from the above. For example, if $m = 0$ and $n > 1$, the push-pull algorithm created a intermediate series a_0, \dots, a_n with $a_{n-1} < b_0$ and $a_n \geq b_0$. Looking at the reduced series a_0, \dots, a_{n-1} , one can apply the above and see that there can be no series a'_0, \dots, a'_{n-1} with $n - 1$ elements that can reach b_0 .

In the general case there is $n > 0$ and $m > 0$. Let x be a point between a_n and b_m , i.e., $b_m \leq x \leq a_n$. If x is not equal to any point in M' , then some integer q can be found such that $a'_{q-1} < x < a'_q$. Looking at the constructed left- and right-hand series in \tilde{M} , one can see that in order for M' to have less intervals than M , $q - 1 \leq n - 1$

and $n' - q \leq m - 1$. Then, $a'_{q-1} \leq a_{n-1}$ and $a'_q \geq b_{m-1}$. But then, $a'_q - a'_{q-1} \geq b_{m-1} - a_{n-1}$ is an interval larger than Δg , because the push-pull algorithm would have found an overlap with one step less, i.e., either n or m would have been one less. Thus, M' is no regional grid if it has less intervals than M .

Finally, in the special case where $a_n = b_m = a'_q$ for some q , one can immediately see that q can not be smaller than n , and $n' - q$ can not be smaller than m . \square

To verify that the initial goal of generating an optimal grid for a region R is reached, this section is concluded with Theorem 3:

Theorem 3. *The push-pull algorithm for regional grid generation yields an optimal regional grid as given by Definition 5 for every region R that satisfies Definition 2.*

Proof. Let \tilde{M} be the intermediate grid that is created after the push-pull phase and M be the final regional grid as constructed by the full push-pull algorithm.

Equation (4.10) enforces all the steps in the push-pull phase to be larger than or equal to Δa_0 and Δb_0 respectively. Thus, before normalization, the smallest step in two sets A and B is given by

$$\Delta s = \min\{a_{k+1} - a_k, b_k - b_{k+1}\} = \min\{\Delta a_0, \Delta b_0, \Delta g\}. \quad (4.19)$$

The step Δs given by Equation (4.19) is by definition the normalization step used in the push-pull algorithm. It follows immediately that all the interval values as given by Equation (4.13) must be larger than or equal to 1.

Assuming for the moment that Q is positive, one can immediately see through Equation (4.15) that the normalized interval factors $\hat{\alpha}_k$ are larger than or equal to one. Then, Equation (4.18) ensures that the final grid steps p_k describe intervals no smaller than Δs .

Assuming that there is another regional grid M' with a smallest interval larger than Δs , this grid would necessarily violate Equation (4.19). Therefore, M' does not suffice Definition 4.

If, on the other hand, Q is negative, one can create a second intermediate grid \tilde{M}' by normalizing the intermediate sets A and B of \tilde{M} with $Q' = 0$. This yields two intermediate sets A' and B' where all

intervals are equal to Δs . Because Q' is larger than the original factor Q defined by Equation (4.16), it follows directly from Equation (4.17) that the sum of all intervals in A' and B' must still be larger than the region itself. Thus, the region cannot be split into $m + n - 1$ intervals of length Δs . It follows immediately that the largest possible minimal step cannot be larger than $(b_0 - a_0)/(m + n - 1)$, and the only optimal regional grid in this case is the grid with $m + n - 1$ uniform steps.

Therefore, together with Theorem 2, it follows that M is indeed optimal. \square

4.4.3 Domain Grid Preprocessing

In order to apply the push-pull algorithm to the connected regions of a domain, the dataset describing a domain needs to be generated. In other words, upon initialization of the grid engine, the simulation data needs to be processed and translated into regions.

This involves a number of steps such as the computation of the wavelengths inside the present material types or a geometrical analysis if requested (cf. Section 4.5). Also, the necessary baselines need to be collected. Typical simulations with hundreds of CAD parts can yield very large numbers of baselines. The distances between such baselines can be arbitrarily small, especially if the triangulation of the 3D data is of low quality, giving rise to numerical artifacts. Thus, the initial baseline collection needs to be filtered. This is done by assigning priority values to the initial baselines according to material types and manual input and subsequently ignoring baselines of low priority that are too closely spaced.

This preprocessing step can consume a considerable amount of time. For large simulation setups, execution times of up to a few seconds have been observed, although the average time needed is well below one second. The additional resources needed for the preprocessing step do not slow the push-pull grid engine down because this step needs to be performed only once in full. Subsequent user induced parameter changes result in small changes to the preprocessed dataset since they can affect only one model part at a time.

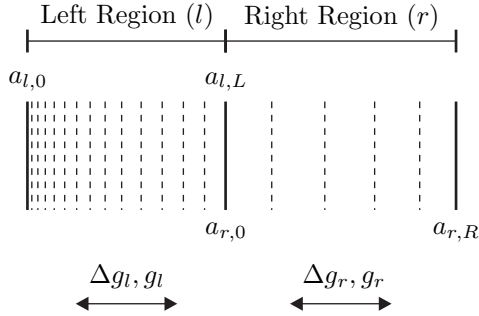


Figure 4.2: Two adjacent grid regions with the corresponding constraints. With a small grading ratio g_l in the left region, the small boundary step $a_{l,0}$ can propagate to the common boundary $b_{r,0} = a_{l,0}$ of the two regions. The grading constraint across the boundary is violated and the right region needs to be updated.

4.4.4 Domain Grid Generation

A complete grid problem consists of multiple regions with shared boundaries as depicted in Figure 4.2. The methodology presented in Section 4.3 can be applied to each section, yielding valid grid configurations that are valid for each region respectively.

The push-pull algorithm can produce grid steps at the region boundaries that might be smaller than the initial boundary steps a_0 and b_0 . Then, the grading ratio across the region boundaries might be too large, and the neighboring regions need to be updated with new boundary steps.

As an example, in Figure 4.2, the leftmost grid step $a_{r,1} - a_{r,0}$ of the right region is too large. Therefore, the maximal boundary step $\Delta a_{0,r}$ at the left side of the right region needs to be updated to

$$\Delta a_{0,r} = (a_{l,L} - a_{l,L-1}) \cdot g_{relax} \cdot \min\{g_l, g_r\}. \quad (4.20)$$

Equation (4.20) shows that such a boundary step correction can only yield smaller values. If Equation (4.20) were to give a larger value, it would mean that the opposite region had needed its boundary step updated.

In the limit of a grading ratio close to 1, as well as for areas of closely spaced baselines, it is often necessary to apply grid steps much smaller than the smallest region in order to satisfy the grading ratio across all region boundaries. As an example, for two regions of 10 and 11 mm, respectively, and a grading ratio of 1, the only solution is a uniform grid step of 1 mm. If the regions themselves are already very small compared to the simulation wavelength, this can lead to an unnecessarily fine discretization. In order to avoid this, it is necessary to relax the grading ratio across region boundaries whenever the maximal boundary step is updated.

No proof has been found that there might not be a domain configuration which leads to an infinite number of such correction steps. In order to avoid unnecessarily repetitive regional grid cycles, the grid engine sorts the regions according to the smallest stepping constraints present in each region ($\min\{\Delta a_0, \Delta b_0, \Delta g\}$). In doing so, it tries to estimate which region may yield the smallest grid step, and, subsequently, triggers a boundary step update for its neighboring regions and processes the regions in this order. Empirical data, summarized in Table 4.1, indicates that the number of correction steps per grid run (Reprocessed Regions) is indeed limited (cf. Section 4.6).

4.5 Advanced Grid Generation

The push-pull algorithm, as described in the previous sections, provides a powerful basis to further optimize and simplify the grid generation.

It is beyond the scope of this work to describe all the refinements and additions to the basic push-pull algorithm. The most important addition, however, is its ability to handle more complex restrictions regarding the stepping. The basic algorithm operates on regions where all steps are bound to a maximum Δg . For many regions this restriction itself leads to suboptimal grids.

4.5.1 Subinterval Stepping

An extended version of the push-pull algorithm allows the processing of arbitrary stepping constraints that may differ throughout the

region. The maximal step Δg is replaced by a subinterval stepping vector:

Definition 9 (Subinterval Stepping). A **stepping vector** S to a region R is a set S_1 of n maximal steps paired with a set S_2 of $n + 1$ subintervals

$$\begin{aligned} S_1 &= \{\Delta g_0, \dots, \Delta g_n\} \in \mathbb{R}^n \\ g_k &> 0 \quad \forall k, 0 \leq k \leq n, \\ S_2 &= \{s_0, \dots, s_{n+1}\} \in \mathbb{R}^{n+1} \\ s_{k+1} &> s_k \quad \forall k, 0 \leq k \leq n \end{aligned} \tag{4.21}$$

where each successive pair $\{s_k, s_{k+1}\}$ defines a subinterval to be gridded with max step Δg_k , and the first and last elements of S_2 match the boundaries a_0 and b_0 of the region R .

To process this information, Equation (4.10) has to be replaced during the push-pull phase with a more sophisticated method to find the next possible step to be added to the intermediate sets. Also, the normalization process must be adapted to account for intermediate sets with arbitrarily varying intervals.

A push-pull algorithm that can process arbitrary maximal steps supports two important cases: First, small regions that originate from model parts with low significance can be merged into enclosing regions by relaying their stepping constraints. This can significantly reduce the number of regions and baselines, thus increasing the degree of freedom for the grid algorithm.

Second, the model may be analyzed for its geometry, and stepping constraints derived for critical structural features. This geometrical analysis allows the automatic resolution of the geometry of critical model parts such as antennas.

4.5.2 Geometrical Analysis

Many applications include structures much smaller than the wavelengths of interest. The major geometrical characteristics of a 3D structure with respect to a staircased grid are the widths (thicknesses) of its subparts, the curvature radii of its surfaces, and the distance between surfaces facing each other (slot widths).

Therefore, an algorithm has been developed and implemented that analyses a structure for the smallest curvature radii, thicknesses, and slots, and translates the gathered information into a stepping vector.

Alongside the main objective of simplifying the grid generation process, the geometrical analysis forms the basis of the optimization engine in SEMCAD X due to its ability to follow changes in geometry automatically [49, 50].

Curvature and Thickness Analysis

Figure 4.3 shows a comparison between conventional and geometrical grid generation for a helix type antenna. Both grids and their corresponding voxels are suitable discretizations because both resolve the antenna features correctly. However, the grid created using the geometry analysis is significantly smaller.

4.3 a) and 4.3 c) show a manually set up grid with maximal step and boundary steps iteratively decreased such that the subsequent voxel generation produced an error free discretization after [51]. This manual grid needed the fine tuning of 6 parameters (boundary steps and maximal steps for each axis) and is only suitable for the helix as is. For a changed geometry, these settings produce a suboptimal, i.e., either an over- or undersampled, grid. On the other hand, Figures 4.3 b) and 4.3 d) show the grid and voxels produced with geometrical analysis. Only 1 to 2 parameters (thickness and/or curvature resolution) are needed here to produce a suitable grid in less than three iterations. More importantly, the geometrical analysis produces optimal grids for any change in geometry, automatically resolving the thickness and curvatures.

Slot Analysis

Figure 4.4 shows an example of geometrical grid generation for a slot antenna, cf. [50]. Figure 4.4 a) shows a uniform grid of a slot antenna where the max step was reduced until the subsequent discretization in Figure 4.4 b) was suitable. The fine grid step is necessary due to highly curved parts of the antenna, and the resulting grid is unnecessarily fine for most areas. This manual grid needed the fine tuning of 6 parameters (boundary steps and maximal steps for each axis) and is

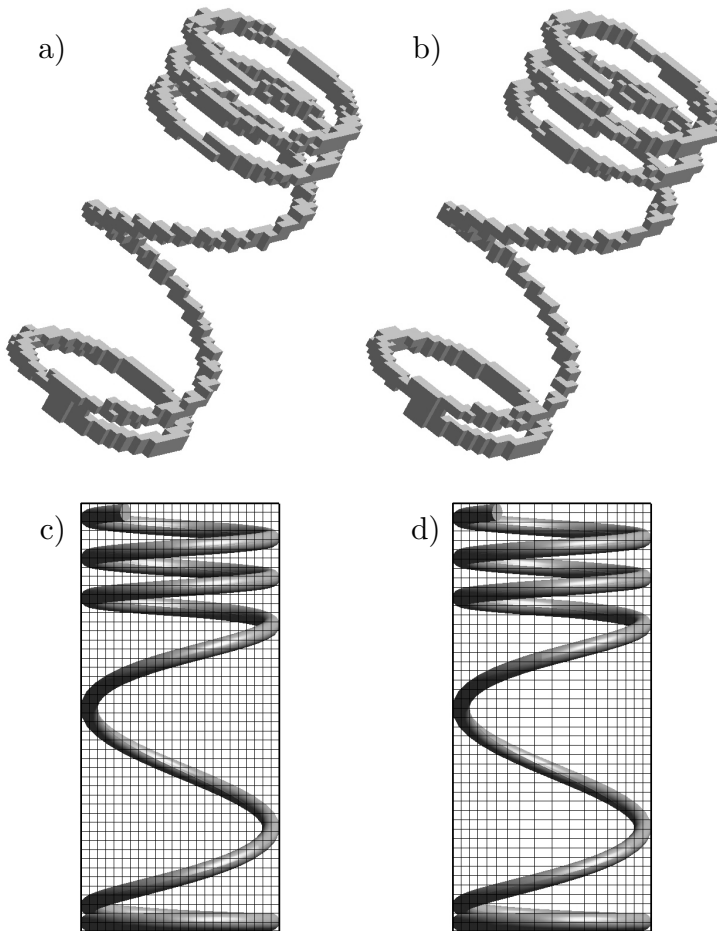


Figure 4.3: Grid and voxels of two different discretizations of a helical antenna. Both meshes resolve the geometry correctly, a visual inspection shows little difference. However, the automatic geometric analysis reduces the total grid size significantly without compromising the smallest grid step. a), c): Manually tuned uniform grid using 44'000 Cells. b), d): Grid and voxels generated with the automatic geometry analysis. Due to the automatic coarsening of the grid, the resulting discretization needs only 22'000 Cells.

only suitable for the antenna as is. For any change in geometry, these settings produce a suboptimal, i.e., either an over- or undersampled, grid. On the other hand, Figures 4.4 b) and 4.4 d) show the grid and voxels produced with geometrical analysis. Only 1 to 2 parameters (thickness and/or curvature resolution) and less than 3 user iterations are necessary to produce a suitable grid. More importantly, the geometrical analysis produces optimal grids for any change in geometry, automatically resolving the slots with the chosen number of grid steps.

4.5.3 Summary of Advanced Features

This section gives an overview over the key features of the interactive grid engine and provides the basis for the interpretation of the results presented in Section 4.6.

Grid Parameters

The following list explains and defines the key grid parameters provided by the interactive grid analysis window (cf. Figure 4.6).

- **Grid Size.** The grid size is given in million cells (MCells) and is defined by

$$(n_x - 1) \cdot (n_y - 1) \cdot (n_z - 1) \cdot 10^{-6} \quad (4.22)$$

where n_k is the total number of grid lines along axis k .

- **Estimated Runtime.** The interactive grid engine features a simulation runtime estimation algorithm that estimates the time step based on the smallest grid steps found in the grid configuration and the material properties assigned to these cells.
- **Min Step.** The minimal grid interval or step of the domain grid of an axis, see Definitions 3 and 7.
- **Max Step.** The maximal grid interval or step of the domain grid of an axis, see Definitions 3 and 7.
- **Max Grad.** The maximal grading ratio of the domain grid of an axis, see Definitions 3 and 7. Here, the grading ratio is, without loss of generality, defined to be the ratio of the larger and the smaller of two intervals, and not vice versa.

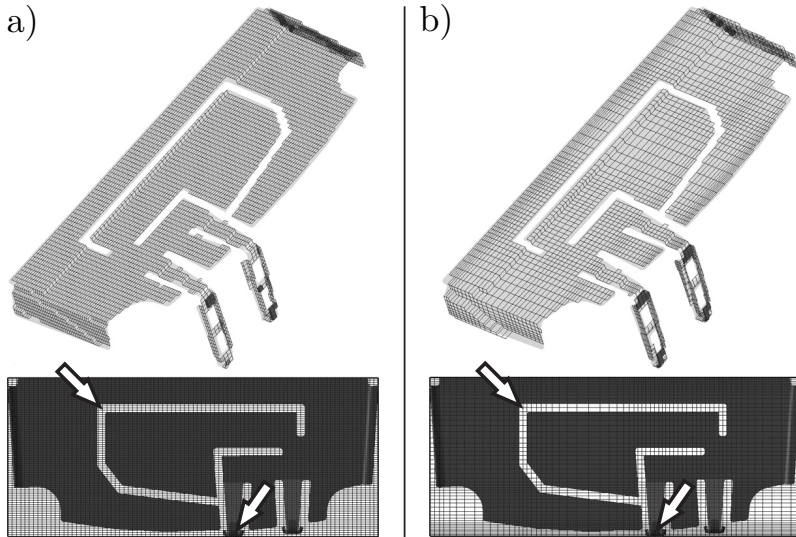


Figure 4.4: Grid and voxels of two different discretizations of a slot antenna. Both meshes resolve the geometry correctly, a visual inspection shows little difference. However, the automatic geometric analysis reduces the total grid size significantly without compromising the smallest grid step. a), c): A slot antenna gridded manually with a uniform grid. The grid enclosing the antenna consists of 400'000 Cells. b), d): The same model is gridded using the slot analysis using only 80'000 Cells. In spite of the much coarser grid, the slots and connectors (indicated by the white arrows) are correctly resolved to ensure accurate results.

Global Grid Settings

The global settings define the default criteria for all objects that do not bear manual (local) settings as described in Section 4.5.3. All of the following global settings can be defined separately for each axis:

- **Max Step.** The maximal step Δg applied to all regions. By default, given in fractions of the smallest wavelength present in the region.
- **Baseline Resolution.** The minimal allowed distance between baselines. The pre-processed collection of baselines is filtered according to the baseline resolution and their respective importance.
- **Scale Factor.** The scale factor is a multiplier for the maximal step and the baseline resolution. Its main use is the interactive refinement of grid sections.
- **Padding (Low, High).** The padding defines the layer of background material (usually free space) around a model.
- **Grading Ratio.** The grading ratio defines the maximally allowed grading.
- **Grading Relaxation.** The grading relaxation defines the maximally allowed relaxation of the grading ratio for densely spaced baselines.

Local Grid Settings

Any model part can be modified to be gridded in one of the following modes:

- **Not Relevant for Grid.** The object along with its material parameters is ignored.
- **Regional.** No baselines are generated, the maximal step is met, and entries in the grid stepping vectors of the enclosing regions are generated.

- **Bounding Box** Baselines are created at the boundaries of the object to create a region with individual grid stepping constraints.
- **Geometrical.** The object is subjected to a geometrical analysis. Grid stepping vectors are produced for the thicknesses, surface curvatures and slots and resolved according to the respective advanced settings.

In addition to the parameters max step, baseline resolution, and scale factor, the following so-called local settings can be adapted for any object in the model:

- **Boundary Steps (Low, High).** The boundary steps define the maximal boundary steps at the lower and higher end of a region belonging to a model part.
- **Curvature Resolution.** The curvature resolution defines a scale factor for the curvature stepping vector. Only in combination with the geometrical mode.
- **Width Resolution.** The width resolution defines a scale factor for the width stepping vector. Only in combination with the geometrical mode.
- **Slot Resolution.** The slot resolution defines a scale factor for the slot stepping vector. Only in combination with the geometrical mode.

4.6 Results

4.6.1 Empirical Algorithm Analysis

Table 4.1 summarizes data from more than 50 simulations for various industrial and academic applications performed at IT'IS [52]. The total of 1968 generated grids, i.e., 1968×3 axes = 5904 domain grid generation cycles, shows that an average of about 40 grids were generated for each simulation, which illustrates the trial-and-error phase during grid setup.

The computers used in this study all had a 2 GHz cpu clock speed or better. The data indicate that the vast majority of execution times are well below 1 ms. This enables the implementation of the algorithm as an interactive feature, where parameter changes are immediately reflected in new grid configurations.

Table 4.1 also shows that the number of regions that needed to be reprocessed (No. of Reprocessed Regions) is, on average, 5 out of 32. More importantly, the number of iterations experienced by a single region (No. of Iterations per Region) never exceeded 2.

Finally, Table 4.1 gives the average and minimal ratio between the smallest grid step and the smallest constraint present throughout all regions (MinMax Ratio), where the smallest constraint is defined as the global minimum of all region widths $b_0 - a_0$ and all boundary and maximal steps, cf. Definition 2. The average of 0.84 underlines the excellent quality of the algorithm.

Table 4.1: Algorithm Performance

Parameter	Value
Max. Execution Time [ms]	41
Avg. Execution Time [μ s]	224
Standard Deviation of Execution Time [μ s]	934
Max. No. of Regions	157
Avg. No. of Regions	32
Max. No. of Reprocessed Regions	65
Avg. No. of Reprocessed Regions	5
Max. No. of Iterations per Region	2
Max. No. of Lines	3872
Avg. No. of Lines	331
Min. MinMax Ratio	0.17
Avg. MinMax Ratio	0.84

4.6.2 Case Study

A fictitious case study presented in this section shows the process flow of an interactive grid generation for a highly complex simulation. The study is thought to investigate a possible influence of implanted devices on the SAR distribution in the human body on exposure to real-world mobile phones. An example simulation of such a study is subject to the new interactive grid generation approach and consists of the following main parts:

- A male phantom forms the basis of the presented study. Taken from the Virtual Family [53], the phantom consists of more than 80 different tissue parts with relative permittivities between 1 and 118 and conductivities between 0 and 2 S/m.
- The Motorola v980 flip phone [54] is placed next to the human phantom head. The phone consists of more than 200 distinct CAD parts, and the helical antenna has a diameter of less than 0.5 mm.
- A pacemaker implant is positioned inside the human phantom. The generic model features lead wires with a radius of 0.5 mm that extend over a region more than 100 mm in diameter.

The resulting model is depicted in Figure 4.5. The leads from the pacemaker and the main antenna of the mobile phone are highlighted. The phone operates in the GSM-1900 band, and the simulation is carried out at 1880 MHz, the center frequency of this band.

The goal is to set up a grid that allows the investigation of whether the pacemaker has a significant impact on the SAR distribution in the upper body part. This exemplary problem demands that all of the three major components are discretized with a sufficiently fine resolution. Additionally, the specifications of the hardware in use limit the maximal resolution to 200 MCells [1] including the PML boundaries. Therefore, a size of 175 MCells is targeted, with the premise to discretize the model as accurately as possible without exceeding that boundary. The following step-by-step case study shows that all of these goals can be met within a few iterations. After each step, the feedback from the interactive grid generation algorithm is used

to evaluate the current quality of the grid and to decide on the next steps that need to be taken.

1. **Initial Grid.** Upon starting the grid engine, the initial dataset is created and the default settings are applied to each model part depending on the material type. The default grid step is 0.07λ for all objects. Baselines are created at the boundaries of all metallic parts and the default baseline resolution is 0.002λ . The key parameters of the initial grid are:

Grid Size:	521 MCells	Min. Step:	0.132 mm
Max. Step:	8.79 mm	Est. Runtime:	-

2. **Padding Adjustment.** In a second step, the padding of the simulation, i.e., the layer of air surrounding the model, is adjusted. To investigate a possible influence of the pacemaker, it is not necessary to include the entire body in the simulation. The radiation absorbed by the legs is typically very low due to their distance from the radiating device.

Therefore, the domain boundary in the negative z -direction is moved by 1.2 m, reducing the domain length from 1.9 m to 0.7 m. This is instantly reflected in the grid size while the minimal and maximal step are unaffected:

Grid Size:	247 MCells	Min. Step:	0.132 mm
Max. Step:	8.35 mm	Est. Runtime:	-

3. **Global Settings.** This step, typical for many applications, is the fine-tuning of the global parameters. In this example, a dense distribution of baselines is generated for the large number of very small metallic parts of the phone, leading to grid domains with over 100 regions and a min step of 0.132 mm. This yields an overdiscretization for most parts of the model. In order to reduce the number of baselines and regions, the grading relaxation is increased to a value of 1.15 (15%) and the baseline resolution is increased to $\lambda/100 \approx 1.6 \text{ mm}$. The resulting min step is 0.76 mm, about half of the baseline resolution, as is typically expected for dense distributions of baselines.

Grid Size:	52 MCells	Min. Step:	0.76 mm
Max. Step:	8.42 mm	Est. Runtime:	13 min

4. **Tissue Settings.** The human phantom is a very inhomogeneous collection of parts with hugely varying material properties. Its non-metallic parts, by default, produce no baselines. In order to further reduce the grid, the wavelength resolution inside the tissue parts is set to 0.09λ . This guarantees a correct discretization of the phantom. More importantly, the influence of the subsequent refinement steps on the grid performance can be assessed more accurately because parameters such as the total grid size can be covered by the influence of electrically large bodies. Thus, reducing the grid for the dielectric parts can greatly ease the grid setup for the metallic structures.

Grid Size:	32 MCells	Min. Step:	0.76 mm
Max. Step:	8.6 mm	Est. Runtime:	10 min

5. **Phone.** The most important step in the grid generation process is the refinement of the phone because the antenna contains very thin radiating parts. The setup of these parts will determine the smallest grid step throughout the simulation domain and, therefore, have the greatest influence on the total simulation time.

First, the metallic parts that belong to the antenna are switched to geometrical mode. Due to the thin wires of the helical antenna, the width resolution is set to 1 to ensure that the entire antenna is resolved with at least 1 voxel.

In a second step, the most critical parts of the antenna are refined one by one to improve the accuracy where necessary. Figure 4.6 is a screenshot of the interactive grid session during refinement of the inner helix of the antenna. The user is provided with the grid lines in the main modeling window. It shows the normal grid lines (gray), the baselines (green) defining the grid regions, and the baselines ignored due to the baseline resolution (purple). A scaling window allows interactive refinement of the local grid by scaling the max step for the currently selected model part, while an analysis windows lists the most important

grid characteristics. The user can scale the part interactively to reach an optimal trade off between a fine resolution and an acceptable min step.

This refinement increases the grid size considerably. Due to the reduction of the grid during Steps 1 to 4, the grid parameters after the refinement, when compared to the values taken after Step 4, give an idea of the influence of such a detailed phone model on the total simulation performance. The grid, increasing from 32 to 105 MCells, yields an estimated 2.5 hours of simulation time:

Grid Size:	105 MCells	Min. Step:	0.04 mm
Max. Step:	8.6 mm	Est. Runtime:	2.5 hrs

6. **Pacemaker.** The refinement of the pacemaker follows a procedure analogous to Step 5. The identical geometrical settings are applied to the wires and a subsequent manual refinement is performed. This results in an additional increase of the grid size. However, due to the massive reduction in Steps 2 to 4, the grid is still well below the target of 175 MCells, and a final global refinement can be applied (Step 7).

Grid Size:	137 MCells	Min. Step:	0.04 mm
Max. Step:	9.0 mm	Est. Runtime:	3 hrs

7. **Global Refinement.** Because the hardware used to run the simulation exhibits higher efficiency for grid sizes closer to the supported maximum, and the goal was to run the simulation with the highest possible accuracy, the grid can be enlarged and refined up to the targeted size. The scaling of the global max step preserves the min step in the grid because it can only affect areas with a previously large stepping. Therefore, the global scaling can safely be reduced until the targeted 175 MCells are reached. This results in a max step in the grid of 1.86 mm, an excellent resolution for the phantom.

Grid Size:	174.6 MCells	Min. Step:	0.04 mm
Max. Step:	1.86 mm	Est. Runtime:	13 hrs

Summary

A grid has been created meeting the targeted 175 MCells with a minimal resolution of 40 microns and maximal resolution of 1.86 mm in 7 simple steps. Figures 4.8 and 4.7 show the voxels of the phone and the pacemaker in the generated grid and illustrate the accurate resolution of the critical model parts.

During and after each step, the interactive grid engine has provided the key grid parameters to guide the user towards the desired grid configuration. The methodology can easily be adapted to meet a different set of goals such as providing a grid with the shortest possible simulation time, where the focus would lie on gridding the smallest antenna parts with the coarsest grid possible.

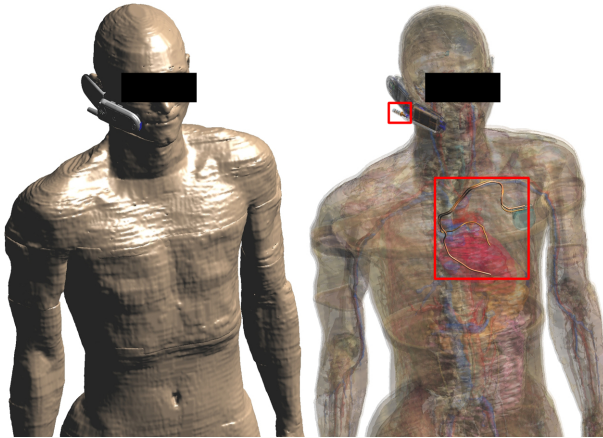


Figure 4.5: Upper half of the model used in the fictitious case study combining an industrial CAD model of a mobile phone, a full body phantom and a generic pacemaker. The left hand side shows a solid rendering, the right hand side a transparent image where the main antenna of the phone and the pacemaker leads are highlighted.

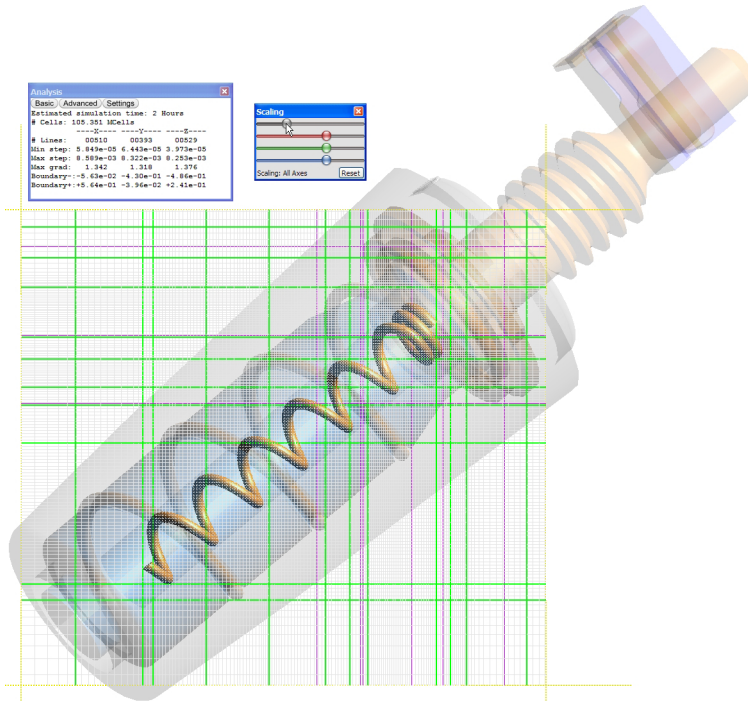


Figure 4.6: Interactive grid generation session to set up the refined regions for the helical antenna of the mobile phone. The scaling window allows interactive refinement of the main parameters for the grid regions of any chosen CAD part, while the feedback window provides a real-time analysis of the current grid.

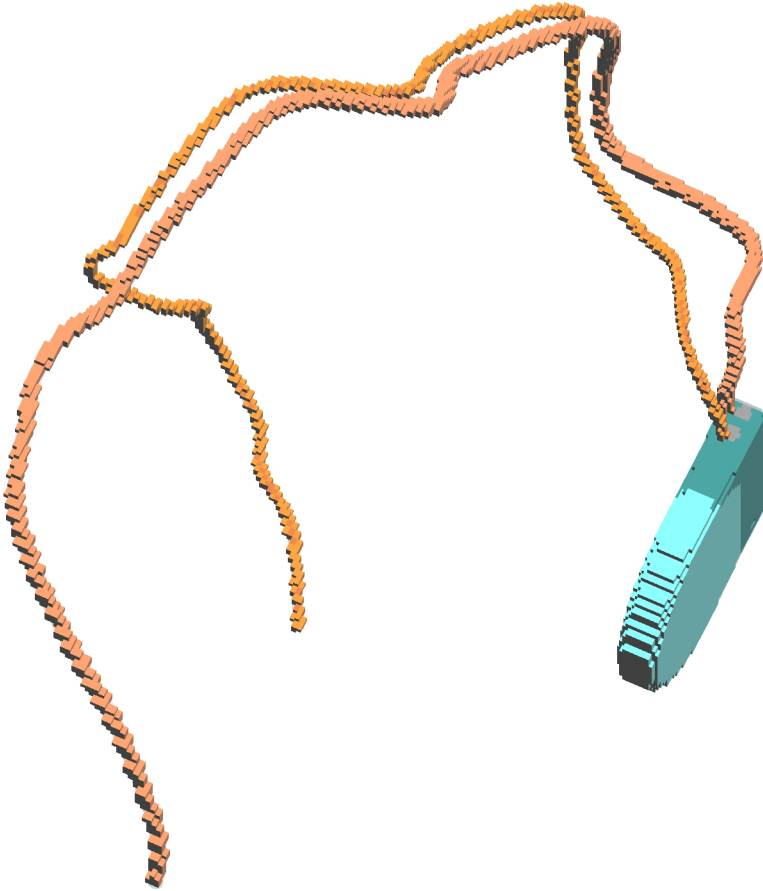


Figure 4.7: Voxel representation of the pacemaker after discretization of the final grid with the voxel generation engine of SEMCAD X [51]. The leads are accurately discretized.

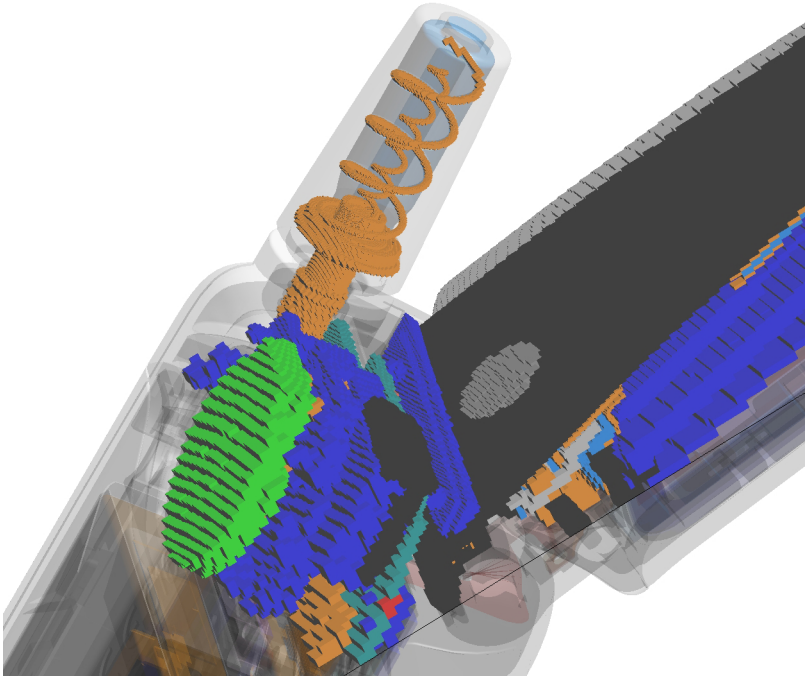


Figure 4.8: Voxel representation after discretization of the final grid with the voxel generation engine of SEMCAD X [51]. The main antenna components are accurately discretized.

Chapter 5

Lossy-Metal Modeling

5.1 Introduction

In order to provide a complete set of algorithms to analyze the influence of losses in metallic structures, a surface impedance boundary condition has been implemented and verified in SEMCAD X. The original approach published in [55] has been enhanced for arbitrary 3D-structures.

One of the shortcomings of the conventional FDTD algorithm is its inability to model and simulate highly conductive media in an efficient manner. The conventional self- and curl-coefficients for the E-update of dielectric, lossy media are given by

$$\alpha_E = \left(1 - \frac{\sigma \Delta t}{2\epsilon}\right) / \left(1 + \frac{\sigma \Delta t}{2\epsilon}\right) \quad (5.1a)$$

$$\beta_E = \left(\frac{\Delta t}{\epsilon \Delta x}\right) / \left(1 + \frac{\sigma \Delta t}{2\epsilon}\right). \quad (5.1b)$$

From Equation (5.1a), one can easily derive the boundary for σ above which α_E is negative:

$$\sigma = \frac{2\epsilon}{\Delta t}. \quad (5.2)$$

For a typical time-step of $\Delta t \approx 10^{-12}$ in an RF simulation at a frequency of $f_0 = 2$ GHz, Equation (5.2) yields an approximate boundary

of $\sigma \approx 1 \text{ S/m}$. The exponential update coefficients, Equations (3.3) through (3.6), keep the simulation stable, if not very accurate, for conductivities that are slightly too large for the conventional update equations.

In principle, it is possible to model any conductivity value with the conventional or exponential update coefficients if the grid-step and the time-step are sufficiently small. However, for almost all applications that need to model high conductivities, this approach is not feasible since it results in extremely large grids and small time-steps.

Surface impedance boundary conditions (SIBCs) have been used for more than 50 years [56, 57, 58]. In FDTD, SIBCs are used to avoid having to resolve the interior of bulk metallic objects. Instead, the complex surface impedance is modeled at the object boundaries.

5.2 Method

Two entirely different approaches have been reported to model broadband SIBC conditions in FDTD. The first group models the SIBC by expressing the frequency-domain SIBC condition by a convolution in the time-domain, and avoiding the infinite sum resulting from the convolution by a recursive-sum technique [59, 60]. These methods show good results, but make it necessary to introduce an additional element into the update equations to account for the convolution terms, altering the conventional update equations significantly. Therefore, it is not possible to combine these material models with other models. As an example, it is not possible to place dispersive media next to lossy metallic objects.

The second method is based on the modeling of the frequency-domain SIBC through an equivalent electrical network that takes the E and H-field components tangential to the metal surface as input [55]. The method bears the advantage that it can be implemented to modify the surface E-field components only, which enables a straightforward combination with all dielectric material models. However, it lacks a general derivation for arbitrary geometries and structures, and the algorithm reported in [55] and summarized in [8] can be applied to brick-shaped objects only. Nevertheless, the possibility of combining the method with other frequency-dependent material models and

its simple algorithmic structure make this approach suitable for an implementation in a professional EM-FDTD tool.

In this section, the equivalent network method is generalized to arbitrarily shaped three-dimensional structures. The method is non-conformal, i.e., it requires a staircased representation of the metal structure to be modeled. This ensures the preservation of the conventional FDTD updating scheme.

5.2.1 The Equivalent Network Model

The equivalent network model is based on the introduction of a special updating scheme for E-Field edges. The model requires moderate additional computational resources compared to the conventional PEC model.

The relation between the tangential E-field and surface-current vectors as described by Ohm's law is given by [61]:

$$\mathbf{E}_{tan}(\mathbf{r}) = Z_s(\mathbf{r}, \omega) \mathbf{J}(\mathbf{r}) = Z_s(\mathbf{r}, \omega) [\mathbf{n}(\mathbf{r}) \times \mathbf{H}(\mathbf{r})]. \quad (5.3)$$

In the Leontovich boundary approximation [56], the surface impedance writes

$$Z(\omega) = \sqrt{\frac{i\omega\mu}{\sigma}}. \quad (5.4)$$

This frequency dependence can be approximated by an equivalent network. An infinite ladder of RC elements, as shown in Figure 5.1, has the input admittance

$$Y(\omega) = \sqrt{\frac{i\omega C}{R}}. \quad (5.5)$$

The authors of [55] show that a truncation of the ladder with 8 RC-elements yields sufficient accuracy. Also, they suggest balancing the parasitic effects of too small or too large values for R and C with the following values to model the surface impedance (5.4):

$$G = \sqrt{\frac{\omega_0\mu}{\sigma}} \frac{\Delta x}{\Delta y} \quad (5.6a)$$

$$C = \sqrt{\frac{\mu}{\omega_0\sigma}} \frac{\Delta x}{\Delta y}. \quad (5.6b)$$

By applying Equation (5.3) to the FDTD update Equation (3.2b), one finds that Y connects the surface current $E_S \Delta e$ with the surface voltage $H_S \Delta h$:

$$E_S \Delta e = Y \cdot H_S \Delta h \quad (5.7)$$

where Δe and Δh are the respective grid steps in direction of the surface E and H components (cf. Figure 5.2).

Figure 5.2 illustrates two cases that require distinct treatment: The left case depicts the situation for a staircased boundary of a metallic object, such as for flat but tilted or curved surfaces. In this case, two H-field components are used to extrapolate the surface voltage, where H_S in Equation (5.7) is taken to be the average. The right case depicts the situation for a flat surface as described in [55] where only one H-field component is used.

The remaining cases, for example, when a lossy metal E-field edge E_S is surrounded by three or four H-field components that do not belong to a lossy metal surface, are ignored, i.e., the E-field edge is considered to represent perfect metal ($E_s \equiv 0$).

5.3 Results & Validation

5.3.1 Lossy Waveguide

A coaxial cable with inner radius $r_i = 3.04$ mm and outer radius $r_o = 7.0$ mm serves as a primary benchmark for evaluating the ac-

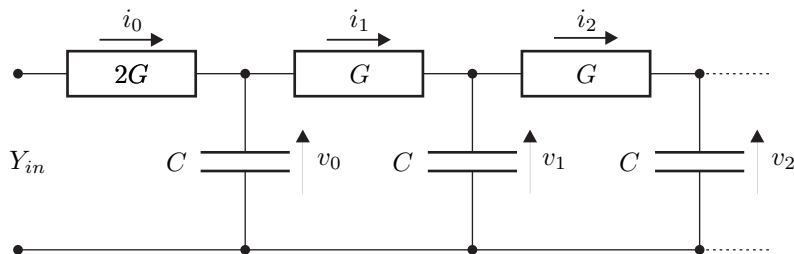


Figure 5.1: A network of an infinite number of RC-elements with input admittance Y_{in} .

curacy of the broadband SIBC for curved surfaces. Figure 5.3 shows the simulated transmission S_{12} over a distance of 30 cm compared to the analytical solution [62]. The results show a gradually growing deviation from the analytical values with decreasing conductivity.

Nevertheless, the model has proved to be sufficiently accurate to model the influence of metallic losses for the majority of applications. Further refinements may include a conformal variant to account for the error introduced by curved surfaces.

5.3.2 Lossy Microstrip Filter

The circuit used for this benchmark was originally published in [63]. Its functionality and the measurement results used in this benchmark have been thoroughly verified and found to be accurate in [64] and [65] by comparison with the results obtained from the method of moments as well as commercial finite element software.

The structure, as defined in [64], has been modeled with SEM-CAD X. Figure 5.4 shows the 3D model of the device including the coaxial waveguides used in the measurement prototype.

The structure was analyzed with the equivalent network model as described in Section 5.2.1. The S-Parameters obtained with SEM-CAD X are compared to the measurement results taken from [64] in Figure 5.5. The FDTD results show the pass-band shifted by less than 0.05 GHz and are in excellent agreement with the measured values.

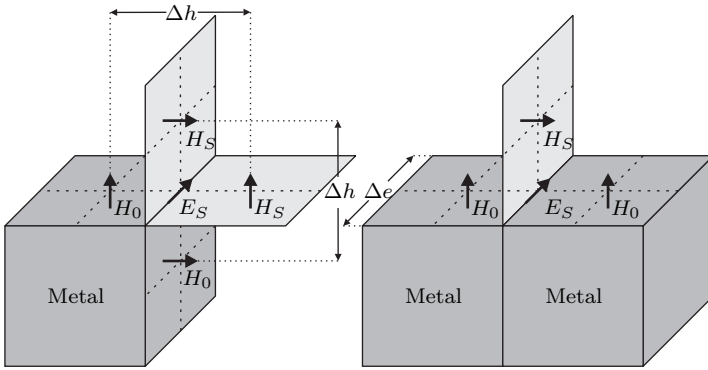


Figure 5.2: The primary two situations for SIBC surface edges E_S and H_S . Left: Staircased surface of a lossy metal object. Right: Flat surface. The H-field edges H_0 are considered to be inside the metallic object and do not contribute to the SIBC computation, i.e., $H_0 \equiv 0$.

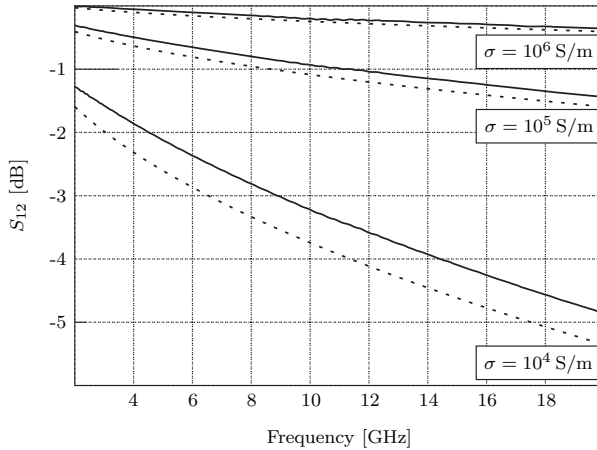


Figure 5.3: S_{12} of a 30 cm long coaxial cable with inner radius $r_i = 3.04 \text{ mm}$ and outer radius $r_o = 7.0 \text{ mm}$. The contiguous lines show the simulated results, the dashed lines the analytical values.

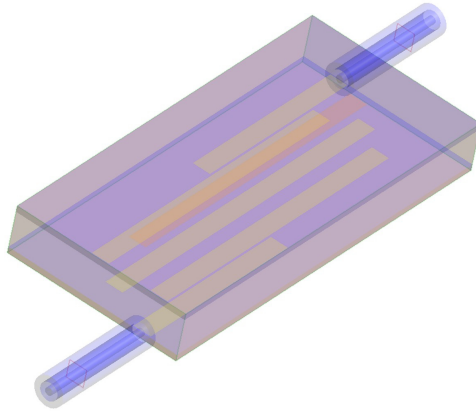


Figure 5.4: The multilayer boxed printed circuit as reported in [63] acts as a bandpass filter. The waveguides at the input and output are excited in SEMCAD X with waveguide sources [66].

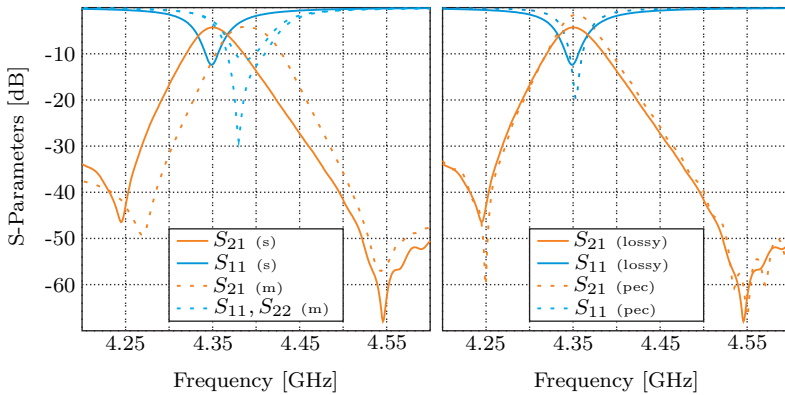


Figure 5.5: S-Parameters of the microstrip filter. Left: Simulated (s) and measured (m) S-Parameters. The unequal S_{11} and S_{22} from measurement indicate to a small asymmetry in the prototype. Right: The simulated S-Parameters for the nonlossy (pec) and lossy (lossy) case depict a significant influence of the metallic losses.

Chapter 6

Thin Conductive Sheets

6.1 Introduction

Presumably the most significant drawback of the conventional Yee FDTD method in electromagnetics [6] is the linear relation between the discretization steps in space and time. If, for example, an electrically small structure makes it necessary to refine the FDTD grid by a factor r in all three spatial dimensions, the total increase in computational resources ranges between r^2 and r^4 . Thus, the method as is cannot be used to model structures relevant to the simulation having dimensions much smaller than the wavelength of interest, such as metallic coatings with thicknesses in the range of 1 μm for frequencies around 1 GHz.

One of the subgroups of electrically small objects is the set of thin conductive (TC) sheets. Multiple approaches to treat TC sheets ([67, 68, 69, 70, 71, 72, 73, 74], an overview can be found in [75]) and thin layers in general ([76, 59, 77, 78, 79, 80]) with the FDTD method have been reported. However, most suffer from the fact that they show results for flat, grid-aligned sheets only. More importantly, the common methodology underlying all of these approaches is that they start from Maxwell's equations to find a discretized form that can be combined with the Yee scheme. By introducing additional degrees of freedom (DOF), i.e., additional grid components or state

variables, the proven robustness and implementational feasibility are no longer guaranteed. Therefore, problems such as instabilities or unmanageable implementational burdens leave such approaches unfit for commercial use in 3D EM FDTD applications.

In this paper, we pursue a different approach: Before enhancing the Yee scheme itself, we propose that the possibility of modeling the phenomenon under consideration with the DOF offered by the Yee scheme should be carefully evaluated. Any such modeling, ultimately resulting in a special set of update coefficients, will be able to exploit the following core advantages over the conservative approach described above:

- The well documented robustness and stability of the Yee scheme are preserved.
- A set of special update coefficients can always be transformed into special material properties, allowing modular programming without the need to change existing FDTD kernels.

Starting from the analytical description of a plane wave incident to a TC sheet, we ask whether we can match its discretized form with the unaltered FDTD equations by choosing appropriate coefficients. The result is an efficient way of treating 3D TC sheets within FDTD without the need to resolve the sheet thickness. We show that it is the physical properties of TC sheets that enable us to do so without the need of additional DOF. In fact, in the case of TC sheets not all DOF offered by the Yee scheme are used, i.e., there is an infinite number of sets of update coefficients that can model TC sheets accurately.

The algorithm has been implemented into the full-featured EM FDTD simulation platform SEMCAD X [66] and applied to various canonical and real-world problems.

6.2 Method

6.2.1 1D Analysis

Plane Wave Penetration

The first step is to define the set of TC sheets. Any 3D object is considered to be a sheet when it can be accurately described by a three-dimensional surface that is extruded along the local surface normals. The extrusion depth is called the thickness of the sheet.

The material of a TC sheet is a good conductor, i.e., inside a TC sheet S with permittivity ϵ_S and conductivity σ_S the current density $\mathbf{J}_S = \sigma_S \mathbf{E}_S$ must be substantially larger than the dielectric displacement current density $\epsilon_S \frac{d}{dt} \mathbf{E}_S$ where \mathbf{E}_S is the electric field strength. For the harmonic case with angular frequency ω this condition reduces to

$$\sigma_S \gg \omega \epsilon_S. \quad (6.1)$$

The second requirement is that the thickness of a sheet d_S is significantly smaller than the skin depth δ_S inside the sheet material:

$$d_S \ll \delta_S = \sqrt{\frac{2}{\omega \sigma_S \mu_S}}. \quad (6.2)$$

Such sheets exhibit the following key properties necessary for the presented algorithm to be applicable:

1. A ray incident on such a sheet will cross the sheet (almost) normally because of the high conductivity. Thus, the distance that a wave travels inside a sheet does not depend on the angle of incidence.
2. Because of 1) and Equation (6.2) the sheet is lossless in very good approximation.

The range of applicability of this method is defined by Equations (6.1) and (6.2). In practice, the accuracy starts to drop as soon as the sheet thickness reaches $d_S = \delta_S/20$.

Considering plane waves incident with an angle θ , TC sheets exhibit the following key features: In the case of normal incidence ($\theta = 0$) and identical material on either side of the sheet, the sum

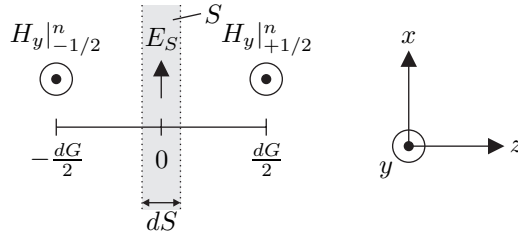


Figure 6.1: 1D Yee grid with a TC sheet S of thickness dS located at $z = 0$. The material parameters of S are ϵ_S , μ_S and σ_S .

of the total reflection coefficient R and transmission coefficient T is unity in very good approximation ($R + T = 1$), i.e., the loss within the sheet is neglectable.

For sheets where the conductivity is not large enough, there will be propagation inside the sheet in direction parallel to the sheet's surface which cannot be neglected. Thus, in order to treat sheets with smaller values of conductivity with this method, it would be necessary to consider propagation parallel to the sheet surface when deriving the update coefficients (cf. Section 6.2.1) which is subject to further research.

Plane Wave Approximation

Figure 6.1 depicts the situation of a one-dimensional TC sheet S at position $z = 0$ in a uniform grid surrounded by free space. The immediate field components are $H|_{-1/2}^n$ and $H|_{+1/2}^n$. The spacing between these field components and the E-field edge at the thin sheet boundary is $dG/2$, i.e., half a grid step.

In the case of a plane wave propagating through the sheet in the $+z$ -direction, the field on the $-z$ side of the sheet is the superposition of the incident and reflected waves, and the field on the $+z$ side is the transmitted part of the plane wave. The analytical field components

are given by

$$E(t, z)|_{z<0} = A_0 e^{i(\omega t - kz)} - R A_0 e^{i(\omega t + kz)} \quad (6.3)$$

$$E(t, z)|_{z>0} = T A_0 e^{i(\omega t - kz)} \quad (6.4)$$

$$H(t, z)|_{z<0} = \frac{1}{Z} A_0 e^{i(\omega t - kz)} + \frac{1}{Z} R A_0 e^{i(\omega t + kz)} \quad (6.5)$$

$$H(t, z)|_{z>0} = \frac{1}{Z} T A_0 e^{i(\omega t - kz)}. \quad (6.6)$$

where Z is the free space impedance and A_0 is the amplitude of the incident E-field.

In contrast, the Yee update equations for the thin sheet edge $E_S^{n+1/2} = E|_0^{n+1/2}$ and the H-field edge $H|_{+1/2}^{n+1}$ are

$$E|_0^{n+1/2} = \alpha_S E|_0^{n-1/2} + \beta_S \left(H|_{-1/2}^n - H|_{+1/2}^n \right) \quad (6.7)$$

$$H|_{+1/2}^{n+1} = \alpha_H H|_{+1/2}^n + \beta_H \left(E|_0^{n+1/2} - E|_{+1}^{n+1/2} \right) \quad (6.8)$$

where the update coefficients α_S , β_S , and β_H are a priori unknown and $\alpha_H = 1$ in free space. Assuming harmonic behavior in steady state for the thin sheet edge $E_S = S A_0 e^{i(\omega t)}$ with amplitude $S A_0$, one can insert the analytical solution given by Equations (6.3) to (6.6) into Equation (6.8) to find

$$\frac{1}{Z} T A_0 e^{-ik \frac{dG}{2}} \left(e^{i\omega \frac{dT}{2}} - e^{-i\omega \frac{dT}{2}} \right) = \beta_H (S A_0 - T A_0 e^{-ikdG}). \quad (6.9)$$

For $S = T$ it follows that β_H must be equal to

$$\beta_H = \frac{1}{Z} \frac{\sin \omega \frac{dT}{2}}{\sin k \frac{dG}{2}} \quad (6.10)$$

which can be simplified to

$$\beta_H \cong \frac{dT}{\mu dG} \quad (6.11)$$

using $\sin x \cong x$, $x \ll 1$. This corresponds to the standard definition for the curl update coefficient in the Yee scheme. Analogously, if $\beta_H = \frac{dT}{\mu dG}$ is inserted into Equation (6.9), one finds that the amplitude S of the field component at $z = 0$ must be $S = T$. Furthermore, the corresponding derivation for the field component $H|_{-1/2}^{n+1}$ yields the very same result.

1D Coefficients

An intermediate conclusion is that the reflection and transmission of a 1D plane wave at a TC sheet in a uniform grid can be modeled by forcing the sheet edge to $E_S(t) = TA_0e^{i\omega t}$. In order to find the appropriate update coefficients, Equation (6.7) is used. Inserting the analytical solutions from Equations (6.3) to (6.6), dividing by the common factor $A_0e^{i\omega t}$ and using $R = 1 - T$ leads to

$$Te^{i\omega dT} = \alpha_S T + \beta_S \frac{R}{Z} e^{i\omega \frac{dG}{2}} \left(e^{ik \frac{dG}{2}} + e^{-ik \frac{dG}{2}} \right), \quad (6.12)$$

a single equation with the two unknown variables α_S and β_S . Obviously, there exists an infinite number of solutions which might be exploited to model a wider range of material properties and/or geometries with this approach. In practice, the following procedure removes one degree of freedom and has produced reliable and stable results. Introducing the common normalized factor c using $\alpha_S = c\alpha_0 = c$ and $\beta_S = c\beta_0$ with the free space values $\alpha_0 = 1$ and $\beta_0 = dT/\epsilon_0 dG$ yields in the limit of an infinitesimally refined grid ($dG, dT \rightarrow 0$)

$$T = cT + c\beta_0 \frac{2}{Z} \frac{R}{dG}, \quad (6.13)$$

which leads to the following formula for the 1D coefficient c and the corresponding update coefficients for the sheet edge:

$$c = \frac{ZT}{ZT + 2R\beta_0}, \quad (6.14)$$

$$\alpha_S = c, \quad (6.15)$$

$$\beta_S = c\beta_0. \quad (6.16)$$

This solution fits nicely into the established material coefficient schemes: For $T \rightarrow 0$ and $R \rightarrow 1$, i.e., for PEC, it follows that $c = 0$. For $T \rightarrow 1$ and $R \rightarrow 0$, i.e., free space, it follows that $c = 1$.

6.2.2 Generalization to 3D

The Minimal Grid

To model arbitrarily curved TC sheets that are not grid aligned, we start from their representation in the primary grid, i.e., the E-field

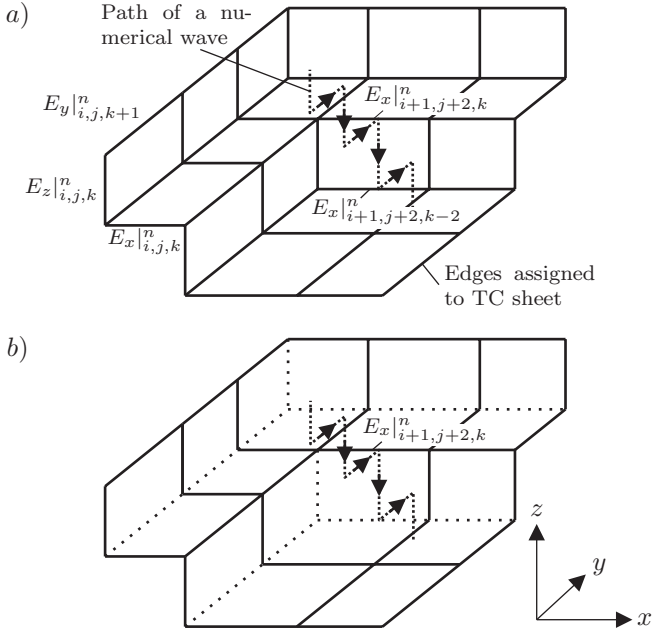


Figure 6.2: Full grid and minimal grid in the primary FDTD grid: a) Full E-field edge representation of a surface. b) A minimal grid. The dotted lines represent reassigned edges.

edges that are associated with a particular sheet. Throughout the following discussion we assume that for all points in space the corresponding grid step is substantially smaller than the curvature radius of the sheet. Thus, the following discussion is spared implementational considerations that are not relevant to the core functionality of the presented TC sheet algorithm.

Figure 6.2a shows part of a staircased representation of a 3D surface in the primary Yee grid. A (numerical) wave incident with wave vector $\mathbf{k} = (0, +1, -1)$ will excite the FDTD edges in the order indicated in Figure 6.2 by the dotted line. The wave will cross (or be reflected by) the sheet by exciting $E_x|_{i+1,j+2,k}^n$ and $E_x|_{i+1,j+2,k-2}^n$.

If the surface models a perfect electric conductor (PEC) where the

values of the corresponding E-field edges are always equal to zero, the numerical wave following the staircased path shown in Figure 6.2 will never reach edge $E_x|_{i+1,j+2,k-2}^n$. With regard to the incident wave, it does not matter whether that edge is updated with PEC coefficients. Thus, starting from the full FDTD representation of a surface, there must be at least one subset of edges that models a (PEC) surface accurately that cannot be further reduced. We call such a subset of edges a *minimal grid*.

The minimal grid from Figure 6.2b, in which the dotted lines are normal free space edges, yields the very same numerical result as the full grid from Figure 6.2a in the case of a PEC surface and a wave incident as described above. In contrast, a numerical wave incident with wave vector $\mathbf{k}' = -\mathbf{k} = (0, -1, +1)$ would clearly experience a difference: In the case of the minimal grid, it would pass edge $E_x|_{i+1,j+2,k-2}^n$ before being reflected. Thus, every possible minimal PEC grid provides 100% reflection but may introduce a small difference in the phase of the reflected wave compared to the standard representation. However, because both the minimal grid and the full grid represent merely a numerical approximation of the original 3D sheet, both have the same level of validity.

In the context of the presented thin sheet algorithm, the important property of a minimal grid is that every edge is responsible for connecting field components from either side of the sheet. Thus, we can see the minimal grid as a collection of one-dimensional edges. The 3D TC sheet algorithm can be seen as a collection of 1D transmissions, each of them responsible for a certain polarization.

Minimal Grid Generation A minimal grid can be found using the algorithm outlined by the following items where the edge and corner labeling depicted in Figure 6.3 is used:

1. Collect all voxels (FDTD cells in the primary grid) that contain at least 7 edges that are assigned to some thin sheet. The number of such edges is called the *thin sheet edge count* of a voxel.
2. Find the subset of voxels with the largest thin sheet edge count and perform the following analysis for each voxel in this subset:

3. Find all thin sheet edges that have two “parallel neighbors” that also belong to the thin sheet. If, for example, edges 0, 2 and 4 belong to the thin sheet, mark edge 0, if edges 8, 9 and 10 are thin sheet edges, mark edge 9, and so on . . .
4. Using the marked edges from item 3, find the corners that belong to three thin sheet faces (faces of the voxel where all 4 edges belong to a thin sheet). If, for example, edges 2, 3 and 11 are marked, corner D is a thin sheet corner.
5. If a thin sheet corner is found in item 4, reassign all edges connecting to this corner to belong to the material surrounding the thin sheet and re-evaluate the voxel by going back to step 3. Note: If multiple corners are found, only perform the reassigned for one of them (to be chosen at random).
6. If no thin sheet corner is found (anymore), reassign all of the marked edges found in item 3.
7. Stop if the processed subset of voxels had a thin sheet edge count of 7 (cf. item 2) and no edges had to be reassigned. Otherwise, return to item 2.

Coefficients in 3D

For flat, grid aligned¹ (FG) sheets in uniform grids, Equation (6.14) gives very accurate results as shown in Section 6.3.2. For staircased, curved sheets the situation becomes a bit more challenging. If the special update coefficients as defined by Equation (6.14) are applied to the minimal grid of an arbitrary 3D surface, the simulation effectively models a staircased surface with a much larger total surface area than the original 3D model. The simulation becomes strongly dependent on the grid.

To alleviate this discretization error, each E-field edge of the minimal grid is considered to model the tangential component $E_t = TE_0 e^{i\omega t}$ of a plane wave that is incident at a normal angle. In other

¹i.e., with a surface normal in x -, y -, or z -direction.

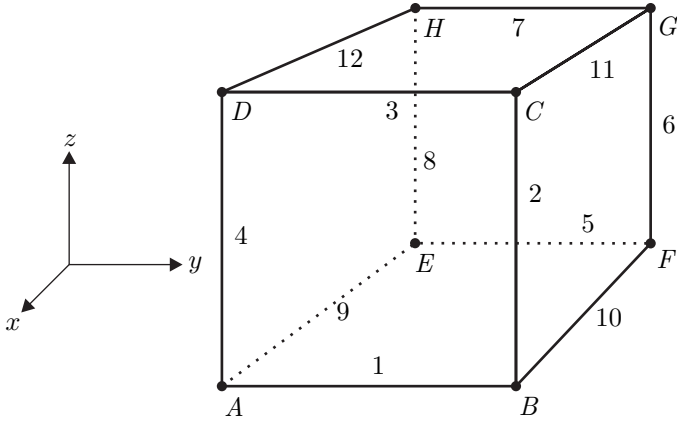


Figure 6.3: Enumeration of the 12 edges (numerals) and 8 corners (letters) of a voxel in the primary grid.

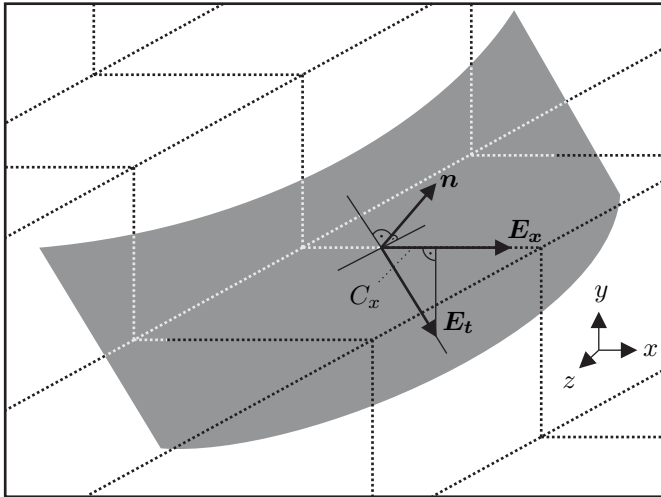


Figure 6.4: A surface element (gray area) in the FDTD grid. At the point where the \mathbf{E}_x pierces the surface, the surface normal \mathbf{n} is used to find the largest tangential component \mathbf{E}_t and the projection ratio C_x .

words, the E-field edges that model a TC sheet are required to represent a field component tangential to the original 3D sheet. Trivially, this condition is satisfied for FG sheets.

In the case of tilted or curved sheets, the E-field edges of the resulting minimal grid are no longer orthogonal to the local (averaged) surface normal. Thus, in a case as depicted in Figure 6.4 the 1D theory cannot be applied directly. Such an edge does not model a locally tangential field component. Furthermore, this geometrical problem applies to the H-field edges as well.

If the local surface normal² is known, the projection to the tangential component is straightforward. Figure 6.4 shows a staircased grid sliced by a curved surface (gray). In general, the numerical Yee component \mathbf{E}_x is not tangential to the surface. Rather, it is thought to model the tangential component \mathbf{E}_t , which is defined by the intersection of the local surface and the plane spanned by \mathbf{n} and \mathbf{E}_x , i.e., \mathbf{E}_t is the largest possible projection of \mathbf{E}_x onto the local surface. As a result, the projection fraction C_x has to be applied during the derivation of the coefficient modification factor c .

Using the normalized vectors \mathbf{e}_x and $\mathbf{e}_t = \mathbf{E}_t / |\mathbf{E}_t| = (\mathbf{n} \times \mathbf{e}_x) \times \mathbf{n}$ the projection fraction C_x is

$$C_x = |\mathbf{e}_t \cdot \mathbf{e}_x| = \sqrt{n_y^2 + n_z^2}. \quad (6.17)$$

Analogously, the coefficients C_y and C_z for the H-field components are

$$C_y = |\mathbf{e}_t \times \mathbf{n}| \cdot \mathbf{e}_y = |n_z| / \sqrt{n_y^2 + n_z^2} \quad (6.18)$$

$$C_z = |\mathbf{e}_t \times \mathbf{n}| \cdot \mathbf{e}_z = |n_y| / \sqrt{n_y^2 + n_z^2}. \quad (6.19)$$

In analogy to Equation (6.13) the simplified update equation for the case of arbitrary field components is

$$C_x T = C_x c T + c \beta_0 \frac{2}{Z} \left(C_y \frac{1-T}{dZ} + C_z \frac{1-T}{dY} \right). \quad (6.20)$$

²The local surface is the plane defined by the local surface normal and the point where the 3D sheet is pierced by the Yee grid edge under consideration. The normal of the local surface is well defined for a sufficiently large curvature radius (cf. Section 6.2.2).

Thus, using $\beta'_0 = \beta_0 dG = dT/\epsilon$, the final formula for the normalized update coefficient c is

$$c = \frac{C_x ZT}{C_x ZT + 2R\beta'_0 \left[\frac{C_z}{dY} + \frac{C_y}{dZ} \right]}. \quad (6.21)$$

which again reduces to Equation (6.14) for the FG case ($C_x = C_y \equiv 1$, $C_z = 0$, $dY = dZ \equiv dG$).

Summary

To model TC sheets that meet the specifications given in Section 6.2, we need information about the local surface normals and the pre-computed transmission and reflection coefficients of a sheet in free space with the given parameters.

By projecting the sheet edges onto the local surface of the sheet, we can find modification factors accounting for surfaces that show an arbitrary angle to the grid axes.

Because of the special properties of TC sheets, the dependence on the angle of incidence is intrinsically taken care of by the Yee scheme. Furthermore, as will be shown in Section 6.3, although the properties of the material surrounding a TC sheet can alter the reflection and transmission coefficients significantly, their influence is automatically modeled by the Yee scheme. Thus, the computation of c is independent from the materials a TC sheet is embedded in.

6.3 Results

6.3.1 Rationale

The benchmarking process is grouped into four steps:

Plane Wave equations provide the basis for the proposed method. Naturally, the first step is to compare numerically analyzed plane wave problems with their analytical solutions.

A Canonical Benchmark modeling a thin metallic bowl in free space allows investigation of the error that tilted, curved sheets and non-uniform grids may introduce.

A *Generic Application* consisting of a simplified microstrip structure serves as a general verification where the parameters of interest are not directly related to the reflection and transmission of plane waves.

A *Real-World Example* modeling a cell phone shows how the TCS algorithm has been successfully applied to a problem that would have been impossible to compute by standard FDTD because of the computational costs.

6.3.2 Plane Wave Verification

Because analytical solutions are required in this step, the set of possible structures is limited to simple geometries, i.e., flat sheets. In this section, the correct treatment of the following variables that can influence the behavior of a sheet is shown:

- Polarization of the incoming wave.
- Angle of incidence of the incoming wave.
- Tilting angle of the thin sheet with respect to the grid.
- Material parameters on either side of the thin sheet.

The common setup for all plane wave verification simulations consisted of a flat sheet either grid-aligned or tilted at one or two axes.

A Total Field/Scattered Field plane wave source³ (cf. [8], Chapter 5) was used to excite the plane wave. The simulation size and time were chosen such that errors originating at the model and source boundaries could not propagate to the field recording region, i.e., a cubic region at the center of the sheet. The measurements were performed by averaging the extracted RMS E-field values in the field recording region. Table 6.1 summarizes the relevant setup parameters for the presented simulations.

Figure 6.5 shows the simulation result of transmission and reflection coefficients in comparison with the corresponding analytical values for Simulation A (Table 6.1). The deviation to the analytical

³The TF/SF source was solely used to excite a plane wave and not to measure the scattered field.

Table 6.1: Plane Wave Simulation Parameters

Parameter		Sim. A	Sim. B	Sim. C
Frequency	GHz	1.8		
Sheet Thickness	μm	1		
Sheet Conductivity ¹	S/m	5309		
Free Space ² :				
Reflection	%	50		
Transmission	%	50		
Material Parameters ³ :				
Incident Side		$\epsilon_r = 1, \mu_r = 1, \sigma = 0$		
Outgoing Side		$\epsilon_r = 2, \mu_r = 1, \sigma = 0$		
Grid Resolution		$\lambda/20$		
Sheet Position:				
X-Axis Tilt:		0°	0°	30°
Y-Axis Tilt:		0°	45°	30°

¹The chosen conductivity yields 50% reflection for a sheet in free space with the given simulation parameters.

²Characteristics of a TC sheet with the given parameters in free space.

³A range of simulations with different combinations of parameters yielded the same accuracy.

values is below the error that can be expected from the simulation uncertainty. The uncertainty was estimated by performing the RMS measurement at the outgoing side when using a PEC sheet which resulted from wave propagation from the edge of the simulation where the plane wave source would inject a field at high angles of incidence.

A series of simulations with different material parameters at both incident and outgoing side showed, that for grid-aligned, flat sheets the algorithm models transmission and reflection of an incident plane wave with good agreement for all material parameters and incident angles.

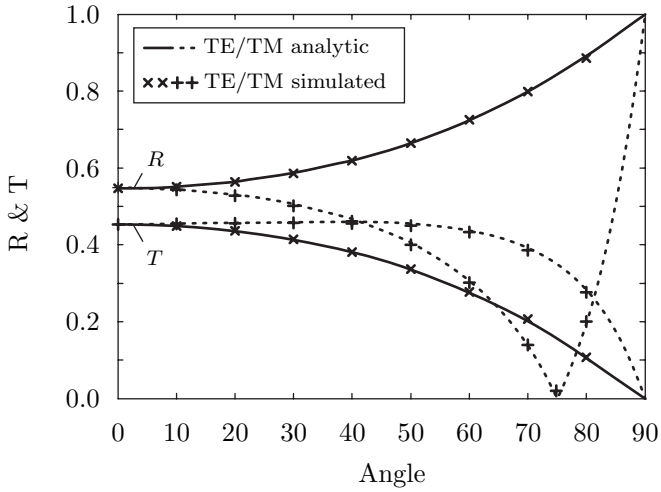


Figure 6.5: Reflection (\times) and transmission ($+$) coefficients of a plane wave incident on a flat, grid-aligned sheet (cf. Table 6.1, **Sim. A**).

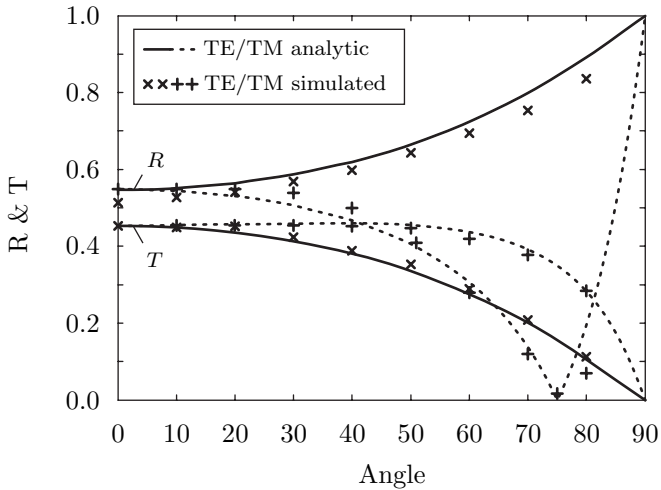


Figure 6.6: Reflection (\times) and transmission ($+$) coefficients of a plane wave incident on a flat, tilted sheet (cf. Table 6.1, **Sim. B**).

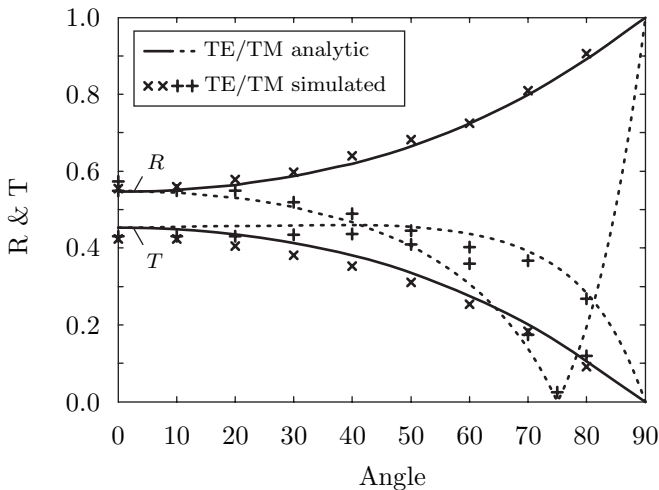


Figure 6.7: Reflection (\times) and transmission ($+$) coefficients of a plane wave incident on a flat, tilted sheet (cf. Table 6.1, **Sim. C**).

Figure 6.6 and 6.7 show the transmission and reflection coefficients for Simulations B and C, respectively (cf. Table 6.1). These simulations describe a canonical example of the generalization to non-grid-aligned sheets as described in Section 6.2.2. As could be expected, there occur small deviations compared to the accuracy of the grid-aligned case shown in Figure 6.5. The resulting slight overall shift in R and T is different for each simulation and polarization. This shift could be due to either dispersion or boundary effects and will be subject to further research.

6.3.3 Canonical Shielding Benchmark

In order to investigate curved sheets in non-uniform grids, a canonical benchmark is used. Because most thin sheet structures are electrically too thin to be modeled with standard FDTD, the range of possible benchmark structures is limited. The geometry used in the presented benchmark consists of a TC sheet in the shape of a spherical dome as depicted in Figure 6.8. It is surrounded by free space. The simulation

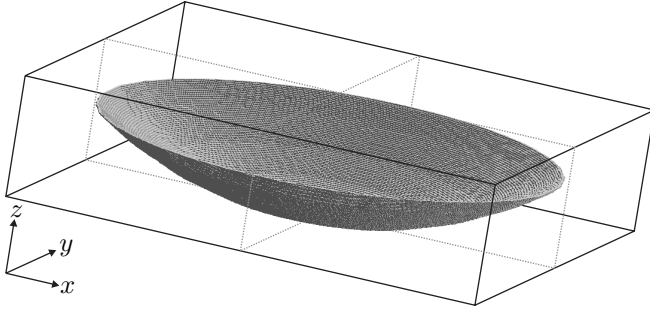


Figure 6.8: Canonical example of a curved TC sheet simulation.

shown in Figure 6.8 proved suitable for our purposes, i.e., it provided the simulation parameters given in Table 6.2 and a full resolution simulation of the dome with standard FDTD is possible with commonly available computational resources.

Figure 6.9 shows a comparison of the root mean square (RMS) E-field values in dB in the x - y -plane at $y = 0$, i.e., the cross-section in the middle of the dome, for the three simulations described in Table 6.2. While the left side shows the simulation results normalized to 1 V/m , the right side shows the difference to the fully resolved FDTD reference simulations.

One can see that the conductivities of the three different sheets have a strong impact on the resulting field distribution. Thus, good agreement between regular FDTD and TCS algorithm provides a strong indication of the validity and performance of the TCS algorithm.

The level of agreement between regular FDTD and TCS algorithm can be ascertained from the difference-plots on the right side of Figure 6.9: As one can expect, the field values differ in close proximity to the thin sheet due to the entirely different modeling approach but otherwise match within -40 dB .

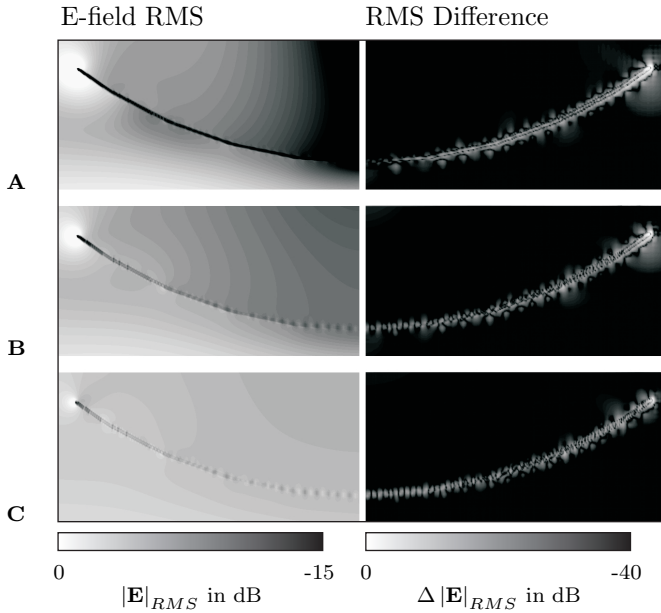


Figure 6.9: Simulation results from simulations **A**, **B** and **C** in the x - y -plane at $y = 0$ as listed in Table 6.2. *Left*: RMS E-field distribution in dB normalized to 1 V/m . *Right*: Difference in E-field RMS between the fully resolved FDTD simulations and the results obtained using the TCS algorithm.

Table 6.2: Shielding Benchmark Simulation Parameters

Parameter	Simulation			
	A	B	C	
Frequency	GHz	60.0		
Sheet Dimensions	mm	$6.0 \times 6.0 \times 2.0$		
Sheet Thickness	μm	20		
Sheet Conductivity	S/m	1065	265	66
Free Space Reflection	%	80	50	20
Free Space Transmission	%	20	50	80
Resources (Staircased FDTD only):				
Max Grid Step	μm	35.5		
Min Grid Step	μm	7.75		
Size	MCells*	22.6		
Simulation Time	sec	1150		
Speed	MCells/sec	121		
Resources (With TCS Algorithm):				
Max Grid Step	μm	54.4		
Min Grid Step	μm	49.7		
Size	MCells	0.64		
Simulation Time	sec	2.4		
Speed	MCells/sec	73		
Running on:	SEMCAD X [66] featuring ClusterInABox 400 [1]			

*Million Yee Cells

6.3.4 Canonical Microstrip Benchmark

To provide an example that relies on a derived value rather than analyzing and comparing the field values, a generic microstrip line is used as defined by Table 6.3. The simple structure allowed the microstrip to be resolved with standard FDTD in order to investigate the relation between the input impedance and the strip parameters. As shown in Figure 6.10, the results taken from the standard FDTD simulations are in very good agreement with the TCS algorithm. Despite the large differences in the discretization and required computational resources as shown in Table 6.3, the TCS algorithm accurately models the strong dependence of the impedance value on the conductivity over the entire frequency range.

One must note, however, that the algorithm was deliberately designed to work with modification of coefficients only. Thus, there can be no true dispersive behavior. The microstrip benchmark merely shows the robustness and validity for broadband simulations as compared to conventional FDTD without dispersive material.

6.3.5 Real-World Problem

Finally, the approach was applied to a real-world application. The multiband (GSM/DCS) phone Nokia 8310 was simulated using SEMCAD X. A discrepancy with the measured results was successfully alleviated using the novel TCS algorithm. One of the parts, a dielectric support frame shown in Figure 6.11, was coated with a thin metallic paint to facilitate grounding between the two printed circuit boards (PCB). Using the TCS algorithm, a series of simulations with different parameters applied to the coating shows a significant effect: as the properties of the coating become less metallic, the grounding between the 2 PCBs is degraded. Significant influence on the E-field strength above the antenna can be seen in Figure 6.12, changing the overall radiation performance of the device.

6.4 Conclusion

A novel algorithm that extends the applicability of FDTD to include the group of arbitrarily curved, thin metallic sheets has been devel-

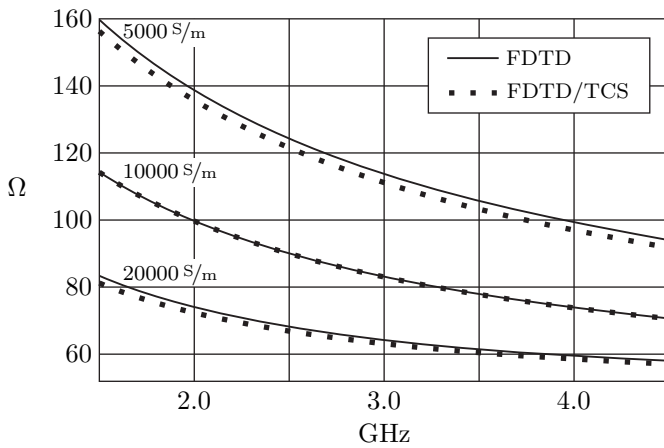


Figure 6.10: Input impedance $Z(f)$ of the microstrip defined in Table 6.3, simulated with regular FDTD and FDTD using the new TCS algorithm. For conductivities between 5000 and 20000 S/m, the recorded impedances are within $\pm 3\%$.



Figure 6.11: SEMCAD X model of the Nokia 8310. The support frame (highlighted) was coated using a conductive spray, which then acts as a grounding mechanism between main and keypad PCBs. Integrated into enhanced FDTD platforms [66] the novel algorithm allows the simulation of such complex 3D real-world problems including EMI and metallic coatings which could not be performed by the standard Yee scheme.

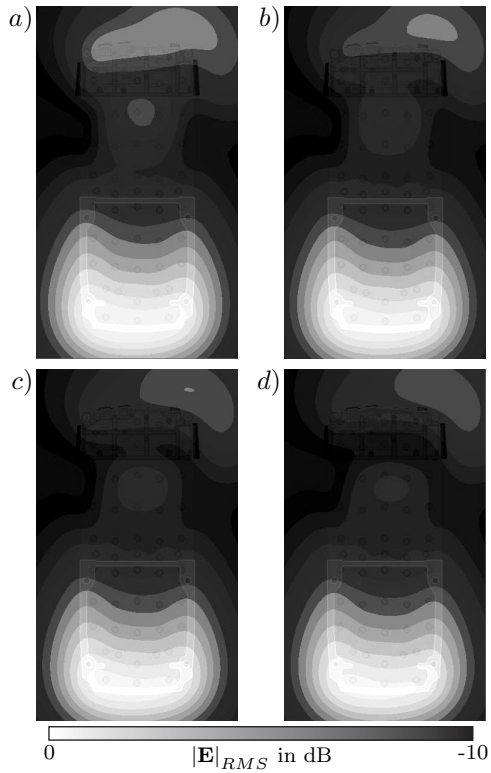


Figure 6.12: E-field RMS distribution at 902 MHz measured 5 mm above the phone casing. With a sheet thickness of $0.5 \mu\text{m}$, the transmission factor and conductivity for the four different cases are: *a)* 75 %, 3500 S/m *b)* 50 %, 10^4 S/m *c)* 25 %, $3 \cdot 10^5 \text{ S/m}$ *d)* 0 %, 10^8 S/m (PEC).

Table 6.3: Microstrip Benchmark Simulation Parameters

Parameter		Simulation		
		A	B	C
Center Frequency	GHz	3.0		
Bandwidth	GHz	3.0		
Substrate Dimensions	mm	90.0 × 70.0 × 0.3		
Substrate Material		$\epsilon_r = 2.7$; $\mu_r = 1.0$ $\sigma = 0.002 \text{ S/m}$		
Microstrip:				
Dimensions	mm	90.0 × 0.8 × 0.01		
Conductivity	10^3 S/m	5	10	20
Resources (FDTD only):				
Max Grid Step	mm	4.67		
Min Grid Step	μm	10.0		
Size	MCells*	3.3	5.24	8.4
Simulation Time	hrs	2.0	2.75	3.75
Speed	MCells/sec	80	90	110
Resources (With TCS Algorithm):				
Max Grid Step	mm	4.67		
Min Grid Step	μm	40		
Size	MCells	0.124		
Simulation Time	sec	5		
Speed	MCells/sec	60		
Running on:		SEMCAD X [66] featuring ClusterInABox 400 [1]		

*Million Yee Cells

oped, implemented and applied to various benchmarks and real-world problems. The core advantage of the approach is that it does not introduce new dependencies to the common FDTD scheme; the TCS update coefficients can thus be transformed into effective material parameters. The algorithm could be successfully applied to existing solvers, including new hardware accelerated solutions.

The benchmarks and applications show very good agreement with analytic values and reference simulations using standard FDTD.

Future work and research will include an extension of the scheme to treat a broader range of materials: *Layers with low or zero conductivity* may be treated by using the additional DOF offered by the unused H-field edges inside the minimal grids. Those H-field edges can be used to model the propagation inside the layer tangential to the surface. *Losses* may be considered by investigating the effect of distributing the modification factor c differently on the update coefficients and/or including more than one layer of edges in the FDTD scheme into the derivation.

Chapter 7

Dispersive Materials

7.1 Introduction

Emerging applications in the fields of photonics [81, 82, 83, 84, 85] and metamaterials [86, 87, 88, 89, 90, 91, 92] involve materials having frequency and intensity dependent polarizations and magnetizations. In the approach by Greene and Taflove [93], it has been shown that the auxiliary differential equation (ADE) method is well suited to model materials that incorporate several non-trivial properties. However, with the prospect of such a method being applied to state-of-the-art problems in optics, the so-called General Vector ADE approach (GVADE) proposed by Greene and Taflove suffers from two major shortcomings:

- Modularity: The method relies on the solution of vector equations such that its structure makes parallelization and adaption to existing FDTD kernels difficult.
- The method employs a Newton iteration to solve the nonlinear equations. This comes with a considerable speed penalty as the inverse of a 3×3 matrix has to be computed for each iteration.

In this paper, an improved ADE-FDTD algorithm is proposed that allows electromagnetic wave propagation to be modeled in materials that exhibit any combination of the first order Drude and Lorentz

dispersion models and the third order phenomena Kerr effect and Raman scattering.

The approach is based on two steps. Firstly, the new variable

$$I = |\mathbf{E}|^2 \quad (7.1)$$

is introduced to preserve the linear nature of the FDTD update equations (cf. Section 7.3). Secondly, it is shown that the determining equation for I is a cubic equation that can be solved analytically if the third-order susceptibility $\chi^{(3)}$ is positive.

The pre-existing code- and data-structure of an existing FDTD kernel can make an implementation of the analytical solution difficult. Therefore, another approach to solve the cubic equation is presented that uses a fixed-point iteration with proven convergence (the equation is badly conditioned for the more efficient Newton iteration). Despite the fixed-point iteration being less efficient than the Newton iteration in terms of number of iterations, the resulting algorithm is shown to be faster than GVADE due to the efficient algorithmic structure of the fixed-point iteration.

To provide validation, the algorithm has been implemented in both Matlab code and the full-featured EM FDTD simulation platform SEMCAD X [66]. Using both implementations, the algorithm is applied to generic benchmark problems and used to verify existing results.

7.2 Dispersion

7.2.1 Introduction

The following discussion provides a summary and description of the phenomena modeled by the proposed algorithm.

In a dielectric medium, the constitutive equations are:

$$\mathbf{B} = \mu\mathbf{H} = \mu_0\mathbf{H} + \mathbf{M} \quad (7.2)$$

$$\mathbf{D} = \epsilon\mathbf{E} = \epsilon_0\mathbf{E} + \mathbf{P}. \quad (7.3)$$

In most cases the magnetization \mathbf{M} is negligible because the magnetic susceptibility is small compared to the electric permittivity. The

overall polarization in terms of higher order susceptibilities (cf. [3]) commonly writes

$$P_i = \epsilon_0 \left(\sum_{ij} \chi_{ij}^{(1)} E_j + \sum_{ijk} \chi_{ijk}^{(2)} E_j E_k + \dots \right) \quad (7.4)$$

where $\chi^{(n)}$ are the dielectric susceptibility tensors of rank $n + 1$.

7.2.2 Linear Dispersion

Ignoring the higher order terms in the series on the right hand side of Equation (7.4) yields a polarization \mathbf{P} that depends linearly on \mathbf{E} . Frequency dependent first order susceptibilities $\chi^{(1)}(\omega)$ that relate \mathbf{E} to \mathbf{P} give rise to linear dispersion. A thorough discussion of the physical concepts and their contribution to linear dispersion can be found in [3] and [4].

Drude Media

The Drude model is based on the collective excitation of the free charges as observed in metals. Their displacement against the ionic trunks results in positively and negatively charged clouds that exert an attractive force on each other. The polarization due to a single Drude pole \mathbf{P}_d is given by

$$\mathbf{P}_d(\omega) = \epsilon_0 \chi_d^{(1)} \mathbf{E}(\omega) = -\epsilon_0 \frac{\omega_d^2}{\omega^2 + i\omega\delta_d} \mathbf{E}(\omega) \quad (7.5)$$

where ω_d is the pole frequency and δ_d is the inverse of the pole relaxation time.

Lorentz Media

A harmonic oscillator is assumed to produce a dipole-moment linear to the amplitude of the excitation. This situation can be found in systems with electrons that are bound harmonically to the atomic trunks, natural frequencies of molecules with dipole-moment or lattice oscillations of ionic crystals. For the polarization due to a single

Lorentz pole \mathbf{P}_l one finds the relation

$$\mathbf{P}_l(\omega) = \epsilon_0 \chi_l^{(1)} \mathbf{E}(\omega) = \epsilon_0 \frac{\Delta\epsilon \omega_l^2}{\omega_l^2 - \omega^2 - 2i\omega\delta_l} \mathbf{E}(\omega) \quad (7.6)$$

with resonance frequency ω_l , damping constant δ_l and $\Delta\epsilon = \epsilon_s - \epsilon_\infty$ being the difference between static and high frequency limit relative dielectric constants.

7.2.3 Nonlinear Dispersion

Because the second-order susceptibility $\chi^{(2)}$ cannot exist in an isotropic medium, this approach models Kerr effect and Raman-Scattering, both of which are third-order effects (cf. [3]).

In a simplified model of the electron response accounting for non-resonant and intensity dependent nonlinear effects, the general equation for $\mathbf{P}(\mathbf{E})$ reduces in the Born-Oppenheimer [5] approximation to

$$P(t) = \epsilon_0 \chi_0^{(3)} E(t) \int_{-\infty}^t g(t-t') E(t')^2 dt' \quad (7.7)$$

where $g(t)$ is the normalized causal response function. The induced polarization is assumed to lie in the same direction as the electric field. The modeled non-resonant third-order processes include phonon interactions and non-resonant electronic effects. The response function can be described as

$$g(t) = \alpha \delta(t) + (1 - \alpha) g_r(t) \quad (7.8)$$

where $\alpha \in [0, 1]$ represents the relative strengths of the Kerr and Raman polarizations. $\delta(t)$ is a Dirac delta function modeling the instantaneous Kerr non-resonant virtual transitions, and

$$g_r(t) = \frac{\tau_1^2 + \tau_2^2}{\tau_1^2 \tau_2^2} e^{-\frac{t}{\tau_2}} \sin\left(\frac{t}{\tau_1}\right) H(t) \quad (7.9)$$

is an approximation of the Raman response function with parameters τ_1 and τ_2 chosen to fit the Raman-gain spectrum and where $H(t)$ is

the Heaviside function. $g_r(t)$ models transient Raman scattering. Effectively, $g_r(t)$ models a single Lorentzian line centered on the optical phonon frequency $\frac{1}{\tau_1}$ having a bandwidth of $\frac{1}{\tau_2}$, the reciprocal phonon lifetime.

Thus, the polarization due to the Kerr effect is given by

$$\begin{aligned} \mathbf{P}_k(t) &= \epsilon_0 \chi_0^{(3)} \mathbf{E}(t) \int_{-\infty}^{\infty} \alpha \delta(t-t') |\mathbf{E}(t')|^2 dt' \\ &= \epsilon_0 \alpha \chi_0^{(3)} |\mathbf{E}(t)|^2 \mathbf{E}(t) = \epsilon_0 \chi_k^{(3)} |\mathbf{E}(t)|^2 \mathbf{E}(t) \end{aligned} \quad (7.10)$$

and the polarization due to Raman scattering is

$$\mathbf{P}_r(t) = \epsilon_0 \mathbf{E}(t) \left[\chi_r^{(3)}(t) * |\mathbf{E}(t)|^2 \right] \quad (7.11)$$

where

$$\chi_r^{(3)}(t) = (1 - \alpha) \chi_0^{(3)} g_r(t). \quad (7.12)$$

The Kerr effect is a frequency-independent, intensity-dependent contribution to the permittivity. Despite that its contribution looks trivial, its effects are very complex. The strength of the Kerr effect is intensity dependent and depends therefore also on the field amplitude. Thus, different parts of a light-pulse are differently affected by the Kerr effect. Depending on the sign of the susceptibility $\chi_k^{(3)}$, the Kerr effect is either focusing, when positive, or defocusing, when negative. In a well balanced case it is possible that the pulse-broadening due to dispersion is neutralized by the Kerr effect such that the light-pulse retains its shape. Such wave-pulses that retain their shape are called solitons. Some illustrative results of solitons are shown in Section 7.5.

7.3 ADE Algorithm

7.3.1 Introduction

The following discussion provides an overview of the modeling of linear and nonlinear dispersion and summarizes the underlying concepts with respect to the ADE formulation. A more thorough discussion can be found in [8].

The ADE method to model dispersive materials in FDTD uses time-domain differential equations to link polarisation terms to the electric flux density. These equations are time stepped in synchronism with Maxwell's curl equations, yielding a composite and self-consistent system. For example, the electric field is still updated via Ampere's law

$$\nabla \times \mathbf{H} = \frac{\partial \mathbf{D}}{\partial t} + \sigma \mathbf{E} = \epsilon_0 \epsilon_\infty \frac{\partial \mathbf{E}}{\partial t} + \frac{\partial \mathbf{P}}{\partial t} + \sigma \mathbf{E} \quad (7.13)$$

and the polarization term requires an additional update equation that is solved in parallel. ADE methods have second-order accuracy. Their time-domain basis makes the modeling of arbitrary nonlinear dispersive media particularly attractive. Furthermore, this method bypasses the computation of convolutions.

The ADE-FDTD formulation presented in this work will be derived for the electric field only. The derivation of the expressions for the magnetic field is completely analogous.

7.3.2 Linear Dispersion

Consider a dispersive medium with D Drude poles and L Lorentz poles in its susceptibility response. In the frequency-domain, the contributions to the polarization from Drude-pole d and Lorentz-pole l write:

$$\mathbf{P}_d(\omega) = -\frac{\epsilon_0 \omega_d^2}{\omega^2 + i\omega\delta_d} \mathbf{E}(\omega) \quad (7.14)$$

and

$$\mathbf{P}_l(\omega) = \frac{\epsilon_0 \Delta \epsilon_l \omega_l^2}{\omega_l^2 - \omega^2 - 2i\omega\delta_l} \mathbf{E}(\omega) \quad (7.15)$$

respectively. A Fourier-transformation of Equations (7.14) and (7.15) to the time-domain, applying finite-difference expressions and substituting $\alpha_{d,l} = \omega_{d,l}^2 \Delta t^2$ and $\beta_{d,l} = \delta_{d,l} \Delta t$ one finds the ADE update equations for the Drude contributions to be

$$\mathbf{P}_d^{n+1} = \frac{4\mathbf{P}_d^n + (\beta_d - 2)\mathbf{P}_d^{n-1} + 2\epsilon_0 \alpha_d \mathbf{E}^n}{\beta_d + 2} \quad (7.16)$$

and for the Lorentz contributions

$$\mathbf{P}_l^{n+1} = \frac{(2 - \alpha_l)\mathbf{P}_l^n + (1 - \beta_l)\mathbf{P}_l^{n-1} + \epsilon_0\Delta\epsilon_l\alpha\mathbf{E}^n}{1 + \beta_l}. \quad (7.17)$$

The update equation for the electric field is then derived by evaluating Ampere's law (7.13) at time step $n + 1/2$. Using the finite-difference expression for the polarization current $\mathbf{J}^{n+1/2} = \frac{\mathbf{P}^{n+1} - \mathbf{P}^n}{\Delta t}$, the update equation for \mathbf{E}^{n+1} writes

$$\begin{aligned} \mathbf{E}^{n+1} &= C_1\mathbf{E}^n + C_2\nabla \times \mathbf{H}^{n+1/2} \\ &\quad - C_2 \sum_{d=1}^D \mathbf{J}_d^{n+1/2} - C_2 \sum_{l=1}^L \Delta \mathbf{J}_l^{n+1/2} \end{aligned} \quad (7.18)$$

with update coefficients

$$C_1 = \frac{2\epsilon_0\epsilon_\infty - \sigma\Delta t}{2\epsilon_0\epsilon_\infty + \sigma\Delta t}, \quad C_2 = \frac{2\Delta t}{2\epsilon_0\epsilon_\infty + \sigma\Delta t}. \quad (7.19)$$

7.3.3 ADE Formulation of the Nonlinear Effects

The following derivation follows the approach presented in [93] up to the point where a Newton iteration is used.

Kerr effect

The equation for the polarization of the Kerr effect at time step n is obtained directly by the finite-difference expression of Equation (7.10):

$$\mathbf{P}_k^n = \epsilon_0\chi_k^{(3)}|\mathbf{E}^n|^2\mathbf{E}^n. \quad (7.20)$$

Raman scattering

Equation (7.11) is solved by introducing a scalar auxiliary variable for the convolution:

$$R(t) \doteq \chi_r^{(3)}(t) * |\mathbf{E}(t)|^2. \quad (7.21)$$

Taking the Fourier transform of Equation (7.21) leads to the Raman frequency domain susceptibility

$$\chi_r^{(3)}(\omega) = \frac{\chi_r^{(3)}\omega_r^2}{\omega_r^2 + 2i\omega\delta_r - \omega^2} \quad (7.22)$$

with

$$\omega_r = \sqrt{\frac{\tau_1^2 + \tau_2^2}{\tau_1^2\tau_2^2}}, \quad \delta_r = \frac{1}{\tau_2}. \quad (7.23)$$

Multiplying both sides by $(\omega_r^2 + 2i\omega\delta_r - \omega^2)$, transforming back to the time-domain and applying finite-difference expressions leads to following update equation for R^{n+1} :

$$\begin{aligned} R^{n+1} &= \left(\frac{2 - \omega_r^2\Delta t^2}{\delta_r\Delta t + 1} \right) R^n + \left(\frac{\delta_r\Delta t - 1}{\delta_r\Delta t + 1} \right) R^{n-1} \\ &+ \left(\frac{\chi_r^{(3)}\omega_r^2\Delta t^2}{\delta_r\Delta t + 1} \right) |\mathbf{E}^n|^2, \end{aligned} \quad (7.24)$$

and the finite-difference expression of Equation (7.11) at time step n becomes

$$\mathbf{P}_r^n = \epsilon_0 \mathbf{E}^n R^n. \quad (7.25)$$

7.3.4 Arbitrary Dispersive Material Algorithm

To outline the final form of the algorithm, consider Ampere's law where we introduce the total polarization \mathbf{P}_{tot} :

$$\nabla \times \mathbf{H} = \epsilon_0 \epsilon_\infty \frac{\partial \mathbf{E}}{\partial t} + \frac{\partial \mathbf{P}_{tot}}{\partial t} + \sigma \mathbf{E} \quad (7.26)$$

where \mathbf{P}_{tot} is given by

$$\mathbf{P}_{tot} = \sum_{l=1}^L \mathbf{P}_l + \sum_{d=1}^D \mathbf{P}_d + \mathbf{P}_k + \mathbf{P}_r. \quad (7.27)$$

The finite-difference expression that follows from (7.26) can be written as

$$\begin{aligned} \nabla \times \mathbf{H}^{n+1/2} &= \mathbf{E}^{n+1} \frac{(2\epsilon_0\epsilon_\infty + \sigma\Delta t)}{2\Delta t} - \\ &\mathbf{E}^n \frac{(2\epsilon_0\epsilon_\infty - \sigma\Delta t)}{2\Delta t} + \mathbf{J}_{tot}^{n+\frac{1}{2}}. \end{aligned} \quad (7.28)$$

The Drude and Lorentz contributions are computed via Equations (7.16) and (7.17) and do not depend on \mathbf{E}^{n+1} . The nonlinear contributions are given by Equations (7.20) and (7.25), where the Raman term depends linearly on \mathbf{E}^{n+1} . In order to preserve the structure of the conventional FDTD update scheme, the linear dependence is enforced for the Kerr term by introducing the new variable

$$I^n \doteq |\mathbf{E}^n|^2. \quad (7.29)$$

Equation (7.28) can now be solved for \mathbf{E}^{n+1} :

$$\begin{aligned} \mathbf{E}^{n+1} &= C_1 \mathbf{E}^n + C_2 \nabla \times \mathbf{H}^{n+1/2} \\ &+ C_2 \left[\sum_{l=1}^L \mathbf{J}_l^{n+1/2} + \sum_{d=1}^D \mathbf{J}_d^{n+1/2} \right] \end{aligned} \quad (7.30)$$

with update coefficients

$$\begin{aligned} C_1 &= \frac{\epsilon_0\epsilon_\infty - \frac{\sigma}{2}\Delta t + \epsilon_0 R^n + \epsilon_0 \chi_k^{(3)} I^n}{\epsilon_0\epsilon_\infty + \frac{\sigma}{2}\Delta t + \epsilon_0 R^{n+1} + \epsilon_0 \chi_k^{(3)} I^{n+1}}, \\ C_2 &= \frac{\Delta t}{\epsilon_0\epsilon_\infty + \frac{\sigma}{2}\Delta t + \epsilon_0 R^{n+1} + \epsilon_0 \chi_k^{(3)} I^{n+1}}. \end{aligned} \quad (7.31)$$

Lastly, one has to compute I^{n+1} , which is by definition

$$I^{n+1} = \mathbf{E}^{n+1} \cdot \mathbf{E}^{n+1}. \quad (7.32)$$

Noting that the update coefficients C_1 and C_2 in Equation (7.31) share the same denominator, one can easily verify that Equation (7.32) can

be written in the scalar form

$$I^{n+1} = \frac{\tilde{a}^2}{(\tilde{b} + \tilde{c}I^{n+1})^2} = f(I^{n+1}) \quad (7.33)$$

where

$$\tilde{a}^2 = \sum_{i=x,y,z} \left[\left(\epsilon_\infty - \frac{\sigma \Delta t}{2\epsilon_0} + R^n + \chi_k^{(3)} I^n \right) E_i^n + \frac{\Delta t}{\epsilon_0} \nabla \times \mathbf{H}^{n+1/2} \Big|_i + \frac{1}{\epsilon_0} \Delta \mathbf{P} \Big|_i \right]^2, \quad (7.34)$$

$$\tilde{b} = \epsilon_\infty + \frac{\sigma \Delta t}{2\epsilon_0} + R^{n+1}, \quad \text{and} \quad \tilde{c} = \chi_k^{(3)}.$$

The term $\nabla \times \mathbf{H}^{n+1/2} \Big|_i$ stands for the i -component of the finite-difference expression of the rotation of the H -Field. The term $\Delta \mathbf{P} \Big|_i$ stands for the i -component of the terms containing the linear dispersion contributions.

Using the substitution $X = I^{n+1}$, Equation (7.33) can be rewritten as a cubic equation

$$aX^3 + bX^2 + cX + d = 0 \quad (7.35)$$

with

$$\begin{aligned} a &= \tilde{c}^2, & b &= 2\tilde{b}\tilde{c}, \\ c &= \tilde{b}^2, & d &= -\tilde{a}^2. \end{aligned} \quad (7.36)$$

The corresponding depressed cubic for $Y = X + b/(3a)$ is

$$Y^3 + pY + q = 0 \quad (7.37)$$

with

$$\begin{aligned} p &= -\frac{1}{3} \left(\frac{b}{a} \right)^2 + \frac{c}{a}, \\ q &= \frac{2}{27} \left(\frac{b}{a} \right)^3 - \frac{bc}{3a^2} + \frac{d}{a}. \end{aligned} \quad (7.38)$$

This depressed cubic has one real solution if the discriminant D given by

$$D = \left(\frac{p}{3}\right)^3 + \left(\frac{q}{2}\right)^2 \quad (7.39)$$

is positive, which reduces to

$$4\tilde{b}^3\tilde{c} + 27\tilde{a}^2\tilde{c}^2 > 0. \quad (7.40)$$

If D is positive, then the solution of Equation 7.35, i.e., the update equation for I is given by

$$I^{n+1} = \left(-\frac{q}{2} + \sqrt{D}\right)^{\frac{1}{3}} + \left(-\frac{q}{2} - \sqrt{D}\right)^{\frac{1}{3}} - \frac{b}{3a}. \quad (7.41)$$

An upper boundary of the second-order Raman contribution R^n depending on the maximal electric intensity $I_{max} = |\mathbf{E}|^2$ is given by

$$R(t) < \chi_r^{(3)}(t) * I_{max} < \frac{\chi_k^{(3)}}{\tau_1} I_{max}. \quad (7.42)$$

Therefore, if the condition

$$\frac{\chi^{(3)}}{\tau_1} I_{max} \ll \epsilon_\infty \quad (7.43)$$

is satisfied, \tilde{b} is always positive and Equation (7.40) is satisfied for all positive values of \tilde{c} and, thus, for all positive values of $\chi^{(3)}$.

Alternatively, Equation (7.33) can be solved by a fixed-point iteration. It can be shown that the fixed-point iteration is stable if the applied field intensities are within a certain range. However, ongoing research is investigating the relation between the stability constraints of the solution of the cubic and the stability of the fixed-point iteration.

Thus, the update cycle of the electric field components can be summarized as in Table 7.1.

Table 7.1: Algorithm Summary

Type	Mathematical Description	Equation
Drude	$\mathbf{P}_d^n \rightarrow \mathbf{P}_d^{n+1}$	(7.16)
Lorentz	$\mathbf{P}_l^n \rightarrow \mathbf{P}_l^{n+1}$	(7.17)
Raman	$R^n \rightarrow R^{n+1}$	(7.24)
Kerr	$I^n \rightarrow I^{n+1}$	(7.33)
E-Field	$\mathbf{E}^n \rightarrow \mathbf{E}^{n+1}$	(7.30)

7.4 Stability

7.4.1 Dispersion Relation

Inserting a discrete plane wave

$$\mathbf{E}(t, \mathbf{r}) = \mathbf{E}_0 \cdot e^{i(\omega n_t \Delta t - k_x n_x \Delta x - k_y n_y \Delta y - k_z n_z \Delta z)} \quad (7.44)$$

into Maxwell's equations (no free charges, no currents)

$$\nabla \times \mathbf{E} = -\mu_{num} \frac{\partial}{\partial t} \mathbf{H} \quad (7.45)$$

$$\nabla \times \mathbf{H} = -\epsilon_{num} \frac{\partial}{\partial t} \mathbf{E} \quad (7.46)$$

$$\nabla \cdot \mathbf{E} = 0 \quad (7.47)$$

$$\nabla \cdot \mathbf{H} = 0 \quad (7.48)$$

$$(7.49)$$

leads to the general dispersion relation

$$\mathbf{K} \cdot \mathbf{K} = \Omega^2 \epsilon_0 \epsilon_{num} \mu_0 \mu_{num} = \Omega^2 \frac{1}{c_0^2} \epsilon_{num} \mu_{num} \quad (7.50)$$

where ϵ_{num} and μ_{num} are the relative numerical permittivity and permeability, respectively, and the numerical frequency Ω and the

numerical wave vector \mathbf{K} are given by

$$\mathbf{K} = \frac{\mathbf{e}_x}{\Delta x} \sin \frac{k_x \Delta x}{2} + \frac{\mathbf{e}_y}{\Delta y} \sin \frac{k_y \Delta y}{2} + \frac{\mathbf{e}_z}{\Delta z} \sin \frac{k_z \Delta z}{2}, \quad (7.51)$$

$$\Omega = \frac{1}{\Delta t} \sin \frac{\omega \Delta t}{2}. \quad (7.52)$$

In a medium with a permeability that is determined by one Drude-pole, one Lorentz-Pole, and the Kerr effect, and a permittivity determined by one Drude-pole, one Lorentz-Pole, Raman scattering and the Kerr effect, the relative numerical permittivity and permeability are given by

$$\epsilon_{num} = \epsilon_\infty + \chi_{k,\epsilon}^{(3)} |\mathbf{E}|^2 + \frac{\Delta \epsilon \omega_{l,\epsilon}^2}{\omega_{l,\epsilon}^2 - \Omega^2 - 2i\Omega \delta_{l,\epsilon}} \quad (7.53)$$

$$- \frac{\omega_{d,\epsilon}^2}{\Omega^2 + i\Omega \delta_{d,\epsilon}} + \frac{\chi_{r,\epsilon}^{(3)} \omega_r^2 |\mathbf{E}|^2}{\omega_r^2 - \Omega^2 + 2\delta_r i\Omega} \quad (7.54)$$

and

$$\mu_{num} = \mu_\infty + \chi_{k,\mu}^{(3)} |\mathbf{H}|^2 + \frac{\Delta \mu \omega_{l,\mu}^2}{\omega_{l,\mu}^2 - \Omega^2 - 2i\Omega \delta_{l,\mu}} \quad (7.55)$$

$$- \frac{\omega_{d,\mu}^2}{\Omega^2 + i\Omega \delta_{d,\mu}} \quad (7.56)$$

respectively.

7.4.2 Phase Velocity Error

Inserting Equations (7.53) and (7.55) into the dispersion relation given by Equation (7.50) and solving for the numerical wave vector K yields

$$K = \frac{2}{\Delta x} \arcsin \left[\frac{\sqrt{\epsilon_{num} \mu_{num}}}{S} \sin \left(\frac{\pi S}{N_\lambda} \right) \right]. \quad (7.57)$$

where we used the conventional definition of the Courant-number

$$S = \frac{c_0 \Delta t}{\Delta x} \quad (7.58)$$

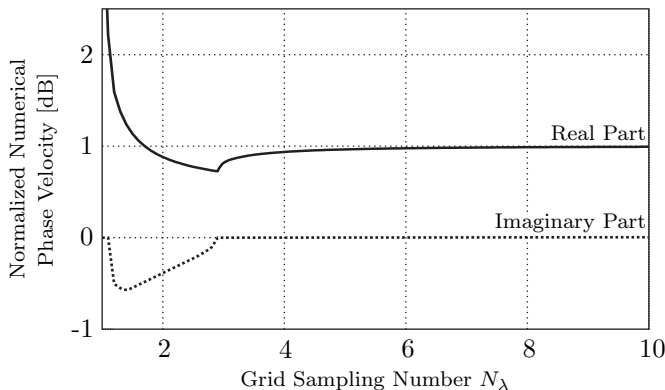


Figure 7.1: The real (solid line) and imaginary (dashed line) parts of the phase velocity $v = \omega/k$ as functions of the grid sampling N_λ . For N larger than ≈ 2.5 the imaginary part vanishes and the numerical phase velocity approaches the physical phase velocity.

and the grid sampling number $N_\lambda = \lambda/\Delta x$ for a given uniform spatial discretization step $\Delta x \equiv \Delta y \equiv \Delta z$.

Equation (7.57) can be solved numerically. An example solution is shown in Figure 7.1. For a large enough grid sampling N_λ , the imaginary part vanishes and the numerical phase velocity approaches the physical phase velocity.

However, Figure 7.1 only shows the qualitative shape of the numerical phase velocity since the latter depends on the material parameters as well as the incident field. It is therefore necessary to estimate the peak intensity that is expected during a simulation to compute a bound for the grid density. As a result, it may be necessary to run multiple simulations with refined grids if the intensity inside the dispersive material is estimated inaccurately.

7.4.3 Stability and Accuracy Analysis

In order to find an upper bound for the time step that guarantees stability, Equation (7.50) has to be solved for the numerical frequency

Ω . In the general case, this is not possible analytically. Moreover, this nonlinear dispersion-relation might contain multiple roots, each of which describes an individual numerical frequency component that yields its own time step boundary.

It is part of ongoing research to develop a reliable and easy to use framework to safely predict the necessary time step constraint for each combination of material parameters.

However, it has been shown in practice that it is sufficient to derive the stability conditions for each material effect separately and choose a time step which satisfies the smallest boundary.

Table 7.2: Stability Conditions

Type	ϵ_{num}	$\Delta t <$	$\Delta x <$
Drude ¹	$\epsilon_\infty - \frac{\omega_d^2}{4\Omega^2}$	$\sqrt{\frac{4\epsilon_\infty \Delta x^2}{4c_0^2 + \Delta x^2 \omega_d^2}}$	$\sqrt{\frac{4c_0^2}{\omega^2 \epsilon_\infty - \omega_d^2}}$
Lorentz ^{1,2,3}	$\epsilon_\infty + \frac{\Delta \epsilon \omega_l^2}{\omega_l^2 - 4\Omega^2}$	$\sqrt{\frac{2\epsilon_\infty}{\xi_1 + \sqrt{\xi_1^2 + \xi_2^2}}}$	$\sqrt{\frac{4c_0^2 \Delta \omega_l}{\omega^2 (\epsilon_\infty \Delta \omega_l + \omega_l^2 \Delta \epsilon)}}$
Kerr	$\epsilon_\infty + \chi_k^{(3)} I$	$\frac{\Delta x}{c_0} \sqrt{\epsilon_\infty + \chi_k^{(3)} I}$	$\sqrt{\frac{4c_0^2}{\omega^2 (\epsilon_\infty + \chi_k^{(3)} I)}}$
Raman ^{1,2,4}	$\epsilon_\infty + \frac{\chi_r^{(3)} I \omega_r^2}{\omega_r^2 - 4\Omega^2}$	$\sqrt{\frac{2\epsilon_\infty}{\tilde{\xi}_1 + \sqrt{\tilde{\xi}_1^2 + \xi_2^2}}}$	$\sqrt{\frac{4c_0^2 \Delta \omega_r}{\omega^2 (\epsilon_\infty \Delta \omega_r + \omega_r^2 \chi_r^{(3)} I)}}$

¹Lossless case ($\delta_d \equiv 0$)

$$^2 \xi_1 = \frac{c_0^2}{\Delta x^2} \sin^2\left(\frac{k_x \Delta x}{2}\right) + \frac{1}{4} \omega_l^2 \epsilon_s; \quad \xi_2 = \sqrt{\epsilon_\infty} \omega_l c_0 \frac{1}{\Delta x} \sin\left(\frac{k_x \Delta x}{2}\right)$$

$$^3 \Delta \omega_l = \omega_l^2 - \omega^2$$

$$^4 \tilde{\xi}_1 = \frac{c_0^2}{\Delta x^2} \sin^2\left(\frac{k_x \Delta x}{2}\right) + \frac{1}{4} \omega_r^2 \left((1 - \alpha) \chi_r^{(3)} + \epsilon_\infty \right); \quad \Delta \omega_r = \omega_r^2 - \omega^2$$

Table 7.2 summarizes the stability conditions for the different dispersion effects.

Another constraint on the time step can be derived from accuracy requirements. It originates in the fact that the physical frequency

ω is misrepresented by the numerical frequency Ω because the time step Δt is always finite. Only in the limit of an infinitesimally small time step are the numerical and the physical frequencies equal. Thus, it is important when simulating dispersive effects that the difference between the numerical and physical frequency is small, i.e., $\omega_{max}\Delta t \leq 0.1$ where ω_{max} is the maximum frequency in the applied frequency spectrum.

7.4.4 Fixed Point Iteration Convergence

The convergence of the fixed point iteration that can be used in the update algorithm for the Kerr effect is proven with Banach's fixed point theorem [94].

Noting that the update coefficients C_1 and C_2 given by Equation (7.31) share the same denominator, one can easily verify that Equation (7.33) can be written in the scalar form

$$I^{n+1} = \frac{a_x^2 + a_y^2 + a_z^2}{(b + cI^{n+1})^2} = f(I^{n+1}) \quad (7.59)$$

where

$$\begin{aligned} a_k &= \left(\epsilon_\infty - \frac{\sigma \Delta t}{2\epsilon_0} + R^n + \alpha \chi_0^{(3)} I^n \right) E_k^n \\ &\quad + \frac{\Delta t}{\epsilon_0} \nabla \times H^{n+1/2} \Big|_k + \frac{1}{\epsilon_0} \Delta P \Big|_k \\ b &= \epsilon_\infty + \frac{\sigma \Delta t}{2\epsilon_0} + R^{n+1} \\ c &= \alpha \chi_0^{(3)}. \end{aligned} \quad (7.60)$$

The term $\nabla \times H^{n+1/2} \Big|_k$ stands for the component k of the finite-difference term of the rotation of the H -Field. The term $\Delta P \Big|_k$ stands for the polarization contributions by Lorentz- and Drude-poles.

The fixed point theorem can be applied to Equation (7.59). It has

to be shown that the first derivation of $f(I)$ given by

$$f'(I^{n+1}) = \frac{-2c(a_x^2 + a_y^2 + a_z^2)}{(b + cI^{n+1})^3} \quad (7.61)$$

is limited $\forall I^{n+1}$ within an interval D . The supremum of $|f'(I^{n+1})|$ is given where $I^{n+1} = 0$:

$$S = \sup_{I^{n+1} \in D} |f'(I^{n+1})| = \frac{2|c|(a_x^2 + a_y^2 + a_z^2)}{|b|^3}. \quad (7.62)$$

If the supremum S is smaller than 1 such that $f(I^{n+1})$ is Lipschitz-continuous with a Lipschitz-constant $L \leq 1$, then $f(I^{n+1})$ is a contraction on D and the fixed point iteration will converge $\forall I^{n+1} \in D$.

However, because a_k is dependent on I^n , the course of $a(I^n)$ has to be considered. As it will be shown later, this limits the fixed point convergence to an electric amplitude interval $D = [0, |\mathbf{E}^n|_{max}^2]$.

The condition for $f(I^{n+1})$ to be a contraction on the interval D can now be written as

$$|c|(a_x^2 + a_y^2 + a_z^2) \leq \frac{|b|^3}{2}. \quad (7.63)$$

In order to find the constraints necessary for the fixed-point iteration to converge, an upper bound for the left hand side of Equation (7.63) and a lower bound for its right hand side have to be found. Presuming sufficiently small spatial and temporal discretization, the upper boundary for $|c|(a_x^2 + a_y^2 + a_z^2)$ can be estimated by neglecting the derivative terms in a_k , setting $\sigma = 0$ and $\alpha = 1$. Equally, the lower bound estimate for b is found by setting $\sigma = 0$ and $\alpha = 1$. For $\alpha = 1$ there is no Raman scattering present and $R^n = 0 \forall n$. Thus, the contraction condition 7.63 can now be written as

$$(\epsilon_\infty + \chi_0^{(3)} I^n)^2 \sum (E_k^n)^2 \chi_0^{(3)} \leq \frac{\epsilon_\infty^3}{2}. \quad (7.64)$$

With $I^n = \sum (E_k^n)^2 = |\mathbf{E}^n|^2$ the final expression is given by

$$|\mathbf{E}^n|^2 \left(\epsilon_\infty + \chi_0^{(3)} |\mathbf{E}^n|^2 \right)^2 \leq \frac{\epsilon_\infty^3}{2\chi_0^{(3)}}. \quad (7.65)$$

The amplitude of the electric field $|\mathbf{E}^n|^2$ has to be limited to an upper value which is determined by the amplitude of the third-order susceptibility $\chi_0^{(3)}$ in order to assure convergence of the fixed point iteration. In this context it is interesting to note that also the Newton-iteration used by [93] becomes unstable for field amplitudes larger than E_{max}^n . Equality in Equation (7.65) is reached at E_{max}^n , such that the convergence interval $D = [0, I_{max}^n = E_{max}^{n2}]$. E_{max}^n can be raised to any desired value by decreasing $\chi_0^{(3)}$. But for a specific material where $\chi_0^{(3)}$ is fixed, only a limited range of intensities can be applied. Furthermore, one has to be aware that the above result is an upper limit which lies too high because some terms were neglected. As a consequence, it is recommended to choose amplitudes that are enough below the above limit.

Equation (7.65) is of third order in $|\mathbf{E}^n|^2$. It can be shown that there exists one real root given by

$$|\mathbf{E}^n|^2 = 0.96 \frac{\epsilon_\infty}{\chi_0^{(3)}} \quad (7.66)$$

which is very similar to the upper boundary for the analytical solution of I^{n+1} , given by Equation (7.43).

Considering the order of magnitude for the third order susceptibilities of physical media as estimated by Equation (2.7), one can see that virtually all media are treatable by both the fixed-point iteration approach and the analytical solution to solve for I^{n+1} .

7.5 Results

The algorithm is subjected to a quantitative accuracy analysis in Section 7.5.1. The verification of the simulated physics of the nonlinear algorithm is done by reproducing the qualitative behavior of the nonlinearity in Section 7.5.2 and a comparison with existing numerical results is in Section 7.5.3.

7.5.1 Four-Wave Mixing (FWM)

In order to test the accuracy of numerical models of the third-order nonlinearity more quantitatively, the approach presented in [84] has

been followed: the analytical solution of a four-wave mixing (FWM) experiment is compared with numerical results. FWM depends only on the third order nonlinearity. Therefore, the accuracy analysis is not affected by inaccuracies of the linear dispersion models.

FWM describes how a pump and a signal wave of frequency ω_p and ω_s , respectively, are converted to a frequency $\omega_c = 2\omega_p - \omega_s$ that is parametrically amplified.

Figure 7.2 shows the output power spectrum at the end of a dielectric slab with a Kerr nonlinearity of $\chi_0^{(3)} = 10^{-18}$. The slab of length 50 μm is illuminated with a pump wave at 192 THz and a signal wave at 195 THz with -20 dB of signal strength. The generated frequencies at 189 THz and 198 THz are clearly visible.

The results of the accuracy analysis are shown in Figure 7.3, where the signal-conversion efficiency in a nonlinear Kerr-medium as a function of pump amplitude is shown. The conversion efficiency is defined as the amplitude ratio of the generated wave and the pump wave. It is found that the FDTD results asymptotically converge to the analytical solution as pump power is decreased. Generally, the FDTD method shows a smaller conversion efficiency than the analytical solution, which is due to the fact that pump and signal depletion in the analytical formulation are ignored (an effect that grows with increasing field intensities). Moreover, the so-called small-signal condition used in the analytical derivation is no longer valid for strong beam intensities. Overall, high accuracy for the new FDTD formulation of the third-order susceptibility can be assessed.

7.5.2 Solitons

A pulse traversing a linear dispersive material suffers from pulse-broadening. On the other hand, nonlinear effects can focus a pulse [82, 95]. If the parameters are well balanced the focusing and defocusing will compensate each other and the pulse will not change its shape, i.e., a soliton is formed.

The results presented here reproduce the findings in [95]. Figures 7.4 and 7.5 show the mode shape of a secant-pulse

$$P(t) = P_0 \cdot \operatorname{sech}\left(\frac{t - 4w}{w}\right)^2 * \sin(\omega t) \quad (7.67)$$

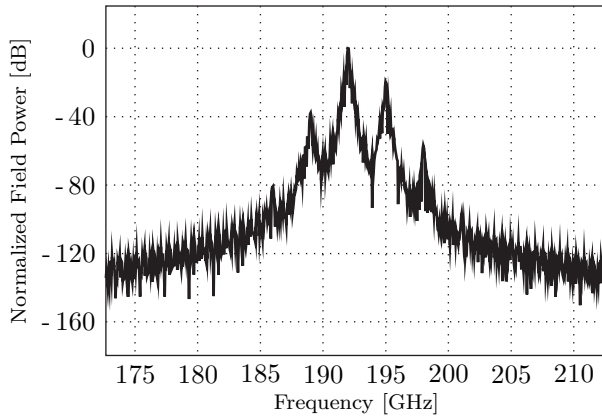


Figure 7.2: Electric field power spectrum of the four-wave mixing experiment. The first two generated frequencies due to FWM are visible at 189 THz and 198 THz.

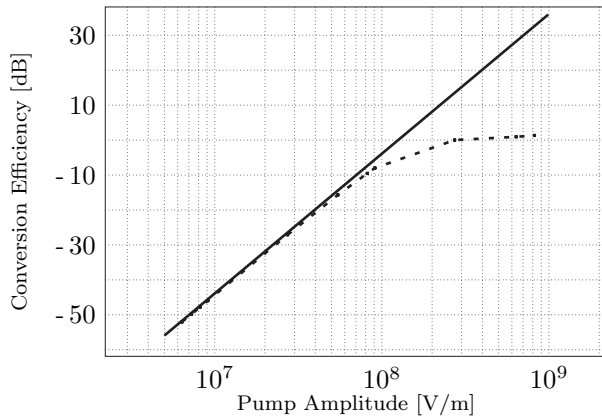


Figure 7.3: Signal-conversion efficiency in a nonlinear Kerr-medium as a function of pump amplitude. The solid line represents the analytical solution, the dotted line results from the proposed FDTD algorithm. For high pump power, signal depletion is observed, giving rise to a strong deviation from the analytical solution.

with Amplitude P_0 and pulse width w , that enters and traverses a dielectric slab with Lorentz dispersion. The TEM pulse, traversing the slab of $60\ \mu\text{m}$, suffers from pulse broadening, as depicted in Figure 7.4. In the second case, where the nonlinear Raman and Kerr effects are present, a soliton is formed, as shown in Figure 7.5. The soliton retains its envelope shape while traversing the slab, indicated through the dotted lines in Figure 7.5. The parameters used in this benchmark are summarized in Table 7.3. Note that the material parameters are not physical. They were chosen to model the soliton phenomenon in order to test the general validity of the algorithm.

Table 7.3: Soliton Benchmark Parameters

Parameter		Value
Pulse Amplitude P_0	[V/m]	1
Pulse Width w	[fs]	10
Center Frequency	[THz]	192
Rel. Permittivity		5.25
Pole Frequency	[GHz]	100
Pol Relax. Time	[10^9 s]	2
Kerr Amplitude	[m^2/V^2]	1
Raman Phonon Frequency	[GHz]	120
Raman Phonon Lifetime	[fs]	32

7.5.3 Photonic Crystal Waveguide

In order to test the 3D performance of our implementation in conjunction with the accelerated hardware solution, the photonic crystal waveguide presented in [96] has been modeled and analyzed in three dimensions. The result is shown in Figure 7.7. For comparison, the power-spectrum obtained with the proposed algorithm is shown in Figure 7.8. It confirms the device's general dynamic performance.

The deviation between the two results may be due to several reasons. First, parameters such as the used boundary method, the reso-

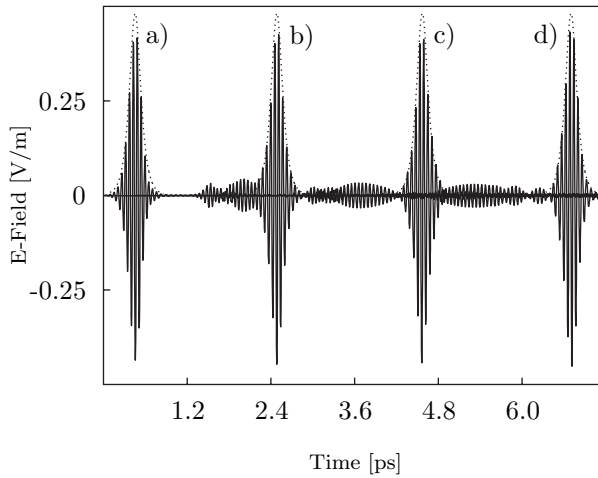


Figure 7.4: A secant pulse is launched and suffers from pulse-broadening due to linear dispersion. The pulse shapes a) through d) show the recorded E-Field values inside the slab at 0, 20, 40, and 60 μm respectively.

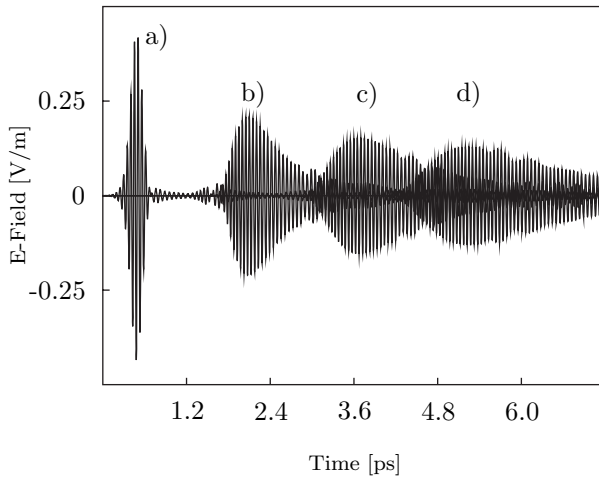


Figure 7.5: A secant pulse is launched and a soliton is formed due to linear and nonlinear dispersion. The pulse shapes a) through d) show the recorded E-Field values inside the slab at 0, 20, 40, and 60 μm respectively. The dotted lines show the constant pulse envelopes.

lution of the simulation, and the excitation scheme may differ between the two implementations. Second, the current implementation of the algorithm lacks a parameter averaging among the FDTD cells, which gives rise to a strong staircasing.

The device is depicted in Figure 7.6, along with four snapshots of the pulse traversing the device. The simulation parameters and benchmark results are given in Table 7.4.

Table 7.4: Waveguide Benchmark Parameters and Results

Parameter		Value
Center Frequency	[GHz]	11.15
Lattice Constant a	[mm]	10
FDTD Grid Step	[mm]	0.3
Simulated Periods		120
Simulated Time	[ns]	5
Total Simulation Time	[min]	3.27

7.6 Conclusion

A novel algorithm that extends the applicability of FDTD to media exhibiting an arbitrary combination of linear and nonlinear effects has been developed, implemented and applied to various benchmarks and real-world problems. The algorithm has been designed to be applied to complex 3D models. In particular, it has been successfully implemented to augment an existing, full-featured simulation package.

The core advantage of the approach is that it avoids the need to employ a vectorial, iterative algorithm to resolve the nonlinear terms. The nonlinear finite-difference expressions are solved by introduction of a new variable. This splits the problem into a linear and nonlinear part, where the latter can be solved by a scalar fixed-point iteration. More importantly, it has been found that the nonlinear terms can be solved analytically for all material compositions with positive third-order susceptibilities, resulting in significant speed improvements.

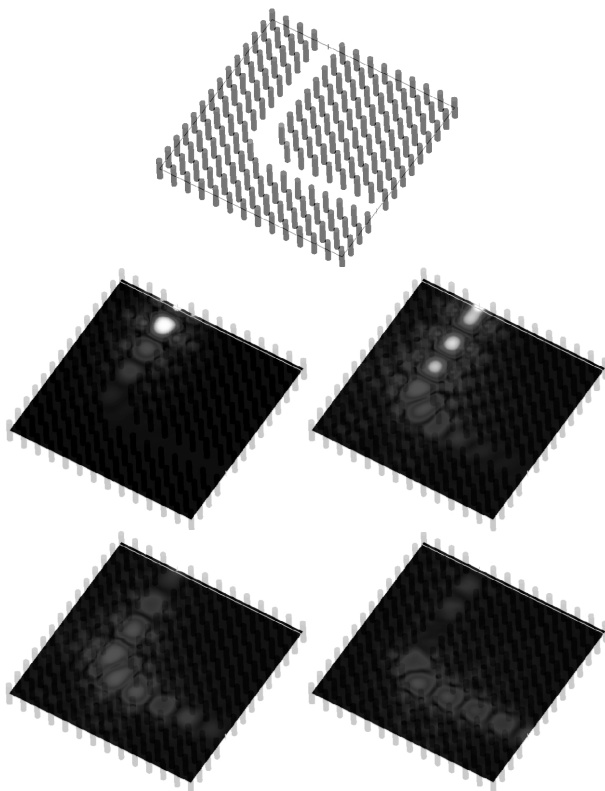


Figure 7.6: A Gaussian pulse is launched into a photonic crystal waveguide. Introducing a nonlinear effect in 3 rods at the waveguide bend improves the transmittance for the lower frequency band shown in Figure 7.8.

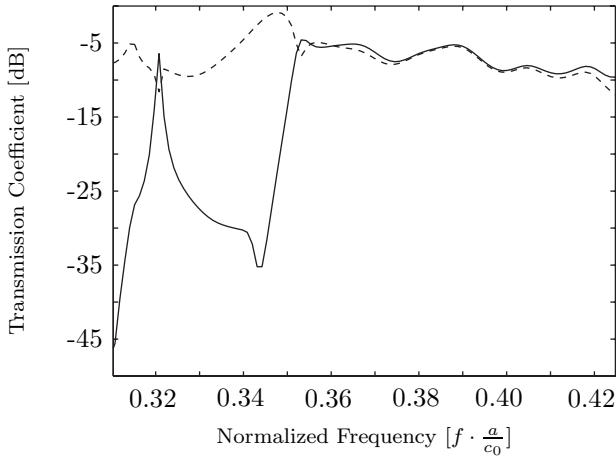


Figure 7.7: Power-spectrum of the transmitted pulse at the waveguide exit (cf. Figure 7.6) as taken from [96]. The solid line represents the linear, the dotted line the nonlinear case.

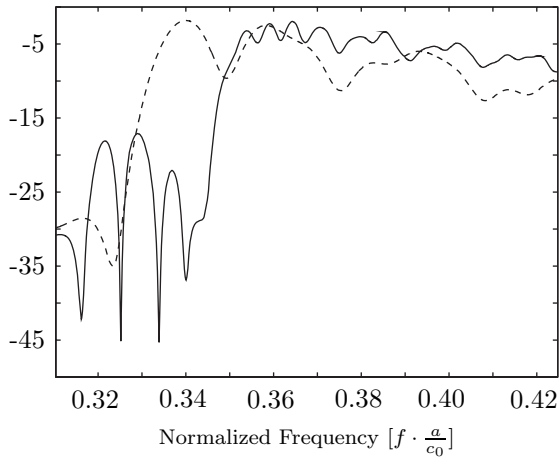


Figure 7.8: Power-spectrum of the transmitted pulse at the waveguide exit (cf. Figure 7.6), simulated with the new algorithm. The solid line represents the linear, the dotted line the nonlinear case.

The benchmarks and applications show very good agreement with analytic values and reference simulations. Future work and research will include an extension of the scheme to treat a broader range of materials, as well as a more detailed analysis of the applicability of the analytical solution to the nonlinear terms. Furthermore, the algorithm is being applied to various research problems in optics with the focus on 3D phenomena.

Part III

Conclusions

Chapter 8

Conclusion

In 2005, when I started working towards my Ph.D. in the IT'IS Laboratories, the first version of SEMCAD X with support for hardware acceleration was just about to be released. It soon became clear that this new technology would enable simulations at a level of detail not previously possible. However, these new possibilities demanded innovative algorithms and methods in order to deal with the new level of detail and complexity. The challenge of developing a grid generation engine that could cope with the new generation of simulations was formulated.

The goal of developing an easy to use, fast, and reliable grid generation framework has been thoroughly achieved. A basic grid generation algorithm has been developed that computes high quality nonuniform grids for the FDTD method in a fraction of a second. The algorithm operates on a optimized data structure that contains all the relevant data from the model and material settings together with a set of parameters designed to work with the grid generation algorithm. Moreover, the algorithm has been designed to be able to process advanced datasets containing information about the geometry of the modeled structure.

The combination of an optimized data and parameter set and an ultra-fast algorithm enables the implementation of an interactive feature, where user changes in parameters are immediately reflected in new grid configurations. It has been shown that this approach signif-

icantly reduces the time necessary to set up a suitable grid configuration. This feature has now been implemented in SEMCAD X and is being used by its customers on a daily basis.

Furthermore, a geometrical analysis that identifies the most critical parts of a structure has been developed. Along with an enhanced version of the grid generation algorithm to process the geometrical data, this feature greatly simplifies the treatment of objects that are highly relevant to the simulation such as antennas or scattering objects.

In order to exploit the possibilities offered by the hardware acceleration systems, an equivalent network method of treating losses in good conductors has been generalized to three dimensions and implemented in SEMCAD X. The results have been shown to be in good agreement with analytical examples and results from recent research. Moreover, it is applied regularly by customers from the mobile phone industry to study the influence of loss on antenna performance.

The broad field of optical applications has moved within reach of FDTD due to the enhanced speed of the accelerated solutions. To provide the means to investigate advanced structures and materials, a novel algorithm to model linear and nonlinear dispersion has been developed. The approach has been tested with generic examples and results from research projects. Stability considerations have been investigated and discussed in detail.

All methods have been designed for maximum efficiency in conjunction with the accelerated solvers. The novel material models have been exposed to both generic and real-world examples and have been found to yield accurate results.

Chapter 9

Outlook

The processing power available through the hardware acceleration technology continues to open new opportunities and challenges. This thesis provides a solid basis on which to overcome the following:

- A range of geometries and structures remains that is not yet optimally supported by the geometrical analysis. An enhanced version that identifies and respects the distinct requirements of different types of 3D objects, e.g., sheets and wires, could further simplify the grid generation process.
- It is not possible to guarantee the stability of every simulation involving media with nonlinear effects. The results of such simulations can depend on parameters such as the amplitude of the excitation that have no qualitative effect in conventional FDTD. A framework to predict the stability and assess the necessary grid and time steps could greatly enhance the usability of the method in investigating optical phenomena.
- Simulations that involve several of the developed material models are not yet supported in every case. An algorithm allowing the simulation of any arbitrary combination of material types would further extend the range of applications.

Appendix A

Dispersion Relation

Starting from the source- and chargefree Maxwell's equations

$$\nabla \times \mathbf{E} = -\mu_{num} \frac{\partial}{\partial t} \mathbf{H} \quad (\text{A.1})$$

$$\nabla \times \mathbf{H} = -\epsilon_{num} \frac{\partial}{\partial t} \mathbf{E} \quad (\text{A.2})$$

$$\nabla \cdot \mathbf{E} = 0 \quad (\text{A.3})$$

$$\nabla \cdot \mathbf{H} = 0 \quad (\text{A.4})$$

the Helmholtz equation is derived by applying the rotation operator to Equation (A.1), solving for $\nabla \times \mathbf{H}$ and combining the result with Equation (A.2):

$$\Delta \mathbf{E} = \epsilon_{num} \mu_{num} \frac{\partial^2}{\partial t^2} \mathbf{E}. \quad (\text{A.5})$$

A plane wave in the discretized grid is of the form

$$\mathbf{E}(t, \mathbf{r}) = \mathbf{E}_0 \cdot e^{i(\omega n_t \Delta t - k_x n_x \Delta x - k_y n_y \Delta y - k_z n_z \Delta z)}. \quad (\text{A.6})$$

In order to insert Equation (A.6) into the Helmholtz equation, the discrete, second-order accurate, central-difference approximation to the second partial derivative of a function $u(x)$ at grid point (u_i, x_i) is used:

$$\left. \frac{\partial^2 u}{\partial x^2} \right|_{x_i} = \frac{u_{i-1} - 2u_i + u_{i+1}}{(\Delta x)^2} + O[(\Delta x)^2]. \quad (\text{A.7})$$

The Laplace operator, when applied to a vector \mathbf{v} , is of the form:

$$\Delta \mathbf{v} = \begin{pmatrix} \Delta v_x \\ \Delta v_y \\ \Delta v_z \end{pmatrix} = \begin{pmatrix} \frac{\partial^2}{\partial x^2} + \frac{\partial^2}{\partial y^2} + \frac{\partial^2}{\partial z^2} \\ \frac{\partial^2}{\partial x^2} + \frac{\partial^2}{\partial y^2} + \frac{\partial^2}{\partial z^2} \\ \frac{\partial^2}{\partial x^2} + \frac{\partial^2}{\partial y^2} + \frac{\partial^2}{\partial z^2} \end{pmatrix} \cdot \begin{pmatrix} v_x \\ v_y \\ v_z \end{pmatrix}. \quad (\text{A.8})$$

With Equations (A.7), (A.8), and (A.6), Equation (A.5) is transformed into

$$\begin{pmatrix} \frac{2}{(\Delta x)^2} [\cos k_x \Delta x - 1] + \frac{2}{(\Delta y)^2} [\cos k_y \Delta y - 1] + \frac{2}{(\Delta z)^2} [\cos k_z \Delta z - 1] \\ \frac{2}{(\Delta x)^2} [\cos k_x \Delta x - 1] + \frac{2}{(\Delta y)^2} [\cos k_y \Delta y - 1] + \frac{2}{(\Delta z)^2} [\cos k_z \Delta z - 1] \\ \frac{2}{(\Delta x)^2} [\cos k_x \Delta x - 1] + \frac{2}{(\Delta y)^2} [\cos k_y \Delta y - 1] + \frac{2}{(\Delta z)^2} [\cos k_z \Delta z - 1] \end{pmatrix} \cdot \begin{pmatrix} E_{0,x} \\ E_{0,y} \\ E_{0,z} \end{pmatrix} = \epsilon_{num} \mu_{num} \frac{2}{(\Delta t)^2} [\cos \omega \Delta t - 1] \cdot \begin{pmatrix} E_{0,x} \\ E_{0,y} \\ E_{0,z} \end{pmatrix}, \quad (\text{A.9})$$

which is a homogeneous system of three equations in the unknown \mathbf{E}_0 . This equation holds if and only if

$$\sum_{i=x,y,z} \frac{2}{(\Delta i)^2} [\cos k_i \Delta i - 1] = \epsilon_{num} \mu_{num} \frac{2}{(\Delta t)^2} [\cos \omega \Delta t - 1] \quad (\text{A.10})$$

which can be simplified to the final form of the dispersion relation

$$\sum_{i=x,y,z} \frac{1}{(\Delta i)^2} \sin^2 \frac{k_i \Delta i}{2} = \frac{\epsilon_{num} \mu_{num}}{(\Delta t)^2} \sin^2 \frac{\omega \Delta t}{2} \quad (\text{A.11})$$

Introducing the numerical frequency Ω and the numerical wave vector \mathbf{K} where

$$\mathbf{K} = \frac{\mathbf{e}_x}{\Delta x} \sin \frac{k_x \Delta x}{2} + \frac{\mathbf{e}_y}{\Delta y} \sin \frac{k_y \Delta y}{2} + \frac{\mathbf{e}_z}{\Delta z} \sin \frac{k_z \Delta z}{2} \quad (\text{A.12})$$

$$\Omega = \frac{1}{\Delta t} \sin \frac{\omega \Delta t}{2} \quad (\text{A.13})$$

the dispersion relation simplifies to

$$\mathbf{K} \cdot \mathbf{K} = \Omega^2 \epsilon_{num} \mu_{num}. \quad (\text{A.14})$$

Appendix B

List of Acronyms

ADE	Auxiliary Differential Equation
ADM	Arbitrary Dispersive Material
CAD	Computer Aided Design
CF	Courant Factor
CFL	Courant-Friedrichs-Lewy
CPU	Central Processing Unit
DCS	Digital Cellular System
DOF	Degree of Freedom
EM	Electromagnetic
FDTD	Finite-Difference Time-Domain
FG	Flat & Grid-Aligned
FWM	Four-Wave Mixing
GSM	Global System for Mobile Communications
GVADE	General Vector Auxiliary Differential Equation
IT'IS	Foundation for Information Technologies in Society
MCells	Million Cells

MKS	Meter Kilogram Second
MRI	Magnetic Resonance Imaging
PCB	Printed Circuit Board
PEC	Perfect Electric Conductor
PML	Perfectly Matched Layer
RC	Resistance-Capacitance
RCS	Radar Cross Section
RF	Radio Frequency
RMS	Root Mean Square
S-Parameter	Scattering-Parameter
SAR	Specific Absorption Rate
SEMCAD	Simulation Platform for Electromagnetic Com- patibility Antenna Design and Dosimetry
SIBC	Surface Impedance Boundary Condition
SPEAG	Schmid & Partner Engineering AG
TCS	Thin Conductive Sheet
TEM	Transverse Electric and Magnetic
TF/SF	Total-Field/Scattered-Field

Appendix C

List of Symbols

Symbol	Dimension	Description
$\nabla \times \mathbf{v}$		Rotation $(\partial/\partial_z - \partial/\partial_y, \partial/\partial_x - \partial/\partial_z, \partial/\partial_y - \partial/\partial_x)^T \cdot \mathbf{v}$
$\nabla \cdot \mathbf{v}$		Divergence $(\partial v_x/\partial_x + \partial v_y/\partial_y + \partial v_z/\partial_z)$
α	1	Relative strength of Kerr effect and Raman scattering respectively
α_E, α_H	1	FDTD E-Field and H-Field self-update coefficients respectively
β_E, β_H	1	FDTD E-Field and H-Field curl-update coefficients respectively
ϵ	$\frac{As}{Vm}$	Electric permittivity
ϵ_r		Relative electric permittivity ϵ/ϵ_0
ϵ_0	$\frac{As}{Vm}$	Electric permittivity of free space: $\epsilon_0 = 1/(c_0\mu_0) \approx 8.8542 \cdot 10^{-12}$
λ	m	Wavelength
μ	$\frac{Vs}{Am}$	Magnetic permeability
μ_r		Relative magnetic permeability μ/μ_0
μ_0	$\frac{Vs}{Am}$	Magnetic permeability of free space:

		$\mu_0 = 4\pi \cdot 10^{-7}$
σ	$\frac{1}{\Omega m}$	Conductivity
$\chi^{(3)}$	$\frac{m^2}{V^2}$	Third order susceptibility
ω, Ω	$\frac{\text{rad}}{s}$	Analytical and numerical angular frequency respectively
B	$\frac{Vs}{m^2}$	Magnetic flux density
C	$\frac{C}{V}$	Capacity
C_x	1	Projection fraction of the x-component in the TCS algorithm
D	$\frac{As}{m^2}$	Electric displacement current
E	$\frac{V}{m}$	Electric field
$E _{(i,j,k)}^n$	$\frac{V}{m}$	E-field component at grid point (i, j, k) and at time $n \cdot \Delta T$
H	$\frac{A}{m}$	Magnetic field
I	$\frac{V^2}{m^2}$	Auxiliary variable in the ADM algorithm
(i, j, k)		Indices of grid lines in an FDTD grid in x-, y- and z-direction respectively
J	$\frac{A}{m^2}$	Current density
k, K	$\frac{1}{m}$	Analytical and numerical wave number respectively
P	$\frac{As}{m^2}$	Polarization
M	$\frac{Vs}{m^2}$	Magnetization
\mathbf{n}		Surface normal (normalized)
N_λ	1	Grid density $N_\lambda = \lambda/\Delta x$
R	Ω	Resistance
R	1	Reflection coefficient
T	1	Transmission coefficient
Δt	s	Time-step
x, y, z	m	Cartesian vector components

Δx	m	Grid step on the x-axis, analogous for the y- and z-axes
Δx_i^E	m	Average grid step on the x-axis between grid lines $i - 1$ and $i + 1$ as used in the FDTD E-field update
$\Delta x_{i+1/2}^H$	m	Grid step on the x-axis between grid lines i and $i + 1$ as used in the FDTD H-field update
Y	$\frac{1}{\Omega}$	Impedance
Z	Ω	Admittance

Bibliography

- [1] Acceleware Inc. <http://www.acceleware.com>.
- [2] J. D. Jackson. *Classical Electrodynamics*. Wiley & Sons, Third edition, 1998.
- [3] R. W. Boyd. *Nonlinear Optics*. Academic Press, 2003.
- [4] H. Ibach and H. Lüth. *Festkörperphysik*. Springer, 2001.
- [5] R. W. Hellwarth. Third-order optical susceptibilities of liquids and solids. *Progress in Quantum Electronics*, 5(1):2–68, 1977.
- [6] K. S. Yee. Numerical solution of initial boundary value problems involving Maxwell's equations in isotropic media. *IEEE Transactions on Antennas and Propagation*, 14(3):302–7, 1966.
- [7] C. Schuster, A. Christ, and W. Fichtner. Review of FDTD time-stepping schemes for efficient simulation of electric conductive media. *Microwave and Optical Technology Letters*, 25(1):16–21, 2000.
- [8] A. Taflove and S. C. Hagness. *Computational Electrodynamics: The Finite-Difference Time-Domain Method*. Artech House, Third edition, 2005.
- [9] R. Courant, K. Friedrichs, and H. Lewy. Über die partiellen Differenzengleichungen der mathematischen Physik. *Mathematische Annalen*, 100(1):32–74, 1928.

- [10] D. H. Choi and J. E. Roy. The dispersion characteristics of the FD-TD method. In *1989 International Symposium Digest: Antennas and Propagation*, volume 1, pages 26–9, San Jose, CA, USA, 1989.
- [11] I. S. Kim and W. J. R. Hoefer. Numerical dispersion characteristics and stability factor for the TD-FD method. *Electronics Letters*, 26(7):485–87, 1990.
- [12] J. Svirgely and R. Mittra. Grid dispersion error using the nonuniform orthogonal finite-difference-time-domain method. *Microwave and Optical Technology Letters*, 10(4):199–201, 1995.
- [13] J. B. Schneider and R. J. Kruhlak. Inhomogeneous waves and faster-than-light propagation in the Yee FDTD grid. *IEEE Antennas and Propagation Society International Symposium Digest*, 1:184–7, 1999.
- [14] J. B. Schneider and C. L. Wagner. FDTD dispersion revisited: faster-than-light propagation. *IEEE Microwave and Guided Wave Letters*, 9(2):54–56, 1999.
- [15] A. Christ. *Analysis and Improvement of the Numerical Properties of the FDTD Algorithm*. PhD thesis, Eidgenössisch Technische Hochschule Zürich, 2003. Diss. ETH - Nr. 15057.
- [16] J. B. Schneider and R. J. Kruhlak. Dispersion of homogeneous and inhomogeneous waves in the Yee finite-difference time-domain grid. *IEEE Transactions on Microwave Theory and Techniques*, 49(2):280–87, 2001.
- [17] K. Nikita, N. K. Uzunoglu, P. Bernardi, M. Cavagnaro, S. Pisa, E. Piuzzi, G. I. Krikellas, and N. Sahalos. A study of uncertainties in modeling the handset antenna and human head interaction using the FDTD method. In T. Perkins, editor, *2000 IEEE MTT-S International Microwave Symposium Digest*, volume 2, pages 1025–8, Boston, MA, USA, 2000.
- [18] K. S. Nikita, M. Cavagnaro, P. Bernardi, N. K. Uzunoglu, S. Pisa, E. Piuzzi, J. N. Sahalos, G. I. Krikelas, J. A. Vaul, P. S. Excell, G. Cerri, S. Chiarandini, R. De Leo, and P. Russo.

- A study of uncertainties in modeling antenna performance and power absorption in the head of a cellular phone user. *IEEE Transactions on Microwave Theory and Techniques*, 48(12):2676–85, 2000.
- [19] P. Monk and E. Suli. Error estimates for Yee’s method on non-uniform grids. *IEEE Transactions on Magnetics*, 30(5):3200–03, 1994.
- [20] D. H. Choi and W. J. R. Hofer. A graded mesh FD-TD algorithm for eigenvalue problems. In *Conference Proceedings: 17th European Microwave Conference*, pages 413–7, Rome, Italy, 1987.
- [21] V. J. Brankovic, D. V. Krupezevic, and F. Arndt. An efficient two-dimensional graded mesh finite-difference time-domain algorithm for shielded or open waveguide structures. *IEEE Transactions on Microwave Theory and Techniques*, 40(12):2272–77, 1992.
- [22] E. A. Navarro, N. T. Sangary, and J. Litva. Some considerations on the accuracy of the nonuniform FDTD method and its application to waveguide analysis when combined with the perfectly matched layer technique. *IEEE Transactions on Microwave Theory and Techniques*, 44(7):1115–24, 1996.
- [23] S. Xiao and R. Vahldieck. A fast FDTD analysis of guided wave structures using a continuously variable mesh with second order accuracy. *Journal of the Institution of Electronics and Telecommunication Engineers*, 41(1):3–14, 1995.
- [24] R. C. Tupynamba and A. S. Omar. Some improvements to the FDTD algorithm for the analysis of passive circuits. In L. Kirby, editor, *Proceedings of IEEE MTT-S International Microwave Symposium*, volume 3, pages 1657–60, Orlando, FL, USA, 1995.
- [25] R. C. Tupynamba and A. S. Omar. Comparison between FDTD graded grids. *IEEE MTT-S International Microwave Symposium*, 2:905–8, 1998.

- [26] J. W. Nehrbass, J. O. Jevtic, and R. Lee. Reducing the phase error for finite-difference methods without increasing the order. *IEEE Transactions on Antennas and Propagation*, 46(8):1194–1201, 1998.
- [27] A. C. Cangellaris and D. B. Wright. Analysis of the numerical error caused by the stair-stepped approximation of a conducting boundary in FDTD simulations of electromagnetic phenomena. *IEEE Transactions on Antennas and Propagation*, 39(10):1518–25, 1991.
- [28] R. Holland. Pitfalls of staircase meshing. *IEEE Transactions on Electromagnetic Compatibility*, 35(4):434–39, 1993.
- [29] C. J. Railton and J. B. Schneider. An analytical and numerical analysis of several locally conformal FDTD schemes. *IEEE Transactions on Microwave Theory and Techniques*, 47(1):56–66, 1999.
- [30] J. B. Schneider and K. L. Shlager. FDTD simulations of TEM horns and the implications for staircased representations. *IEEE Transactions on Antennas and Propagation*, 45(12):1830–38, 1997.
- [31] N. P. Chavannes. *Local Mesh Refinement Algorithms for Enhanced Modeling Capabilities in the FDTD Method*. PhD thesis, Eidgenössisch Technische Hochschule Zürich, 2002. Diss. ETH - Nr. 14577.
- [32] K. S. Kunz and Lee Kuan-Min. A three-dimensional finite-difference solution of the external response of an aircraft to a complex transient EM environment. II. comparison of predictions and measurements. *IEEE Transactions on Electromagnetic Compatibility*, 20(2):333–41, 1978.
- [33] K. S. Kunz and Lee Kuan-Min. A three-dimensional finite-difference solution of the external response of an aircraft to a complex transient EM environment. I. the method and its implementation. *IEEE Transactions on Electromagnetic Compatibility*, 20(2):328–33, 1978.

- [34] Yu Wenhua and R. Mittra. Electromagnetic scattering of underground object using nonuniform mesh FDTD and PML. *Microwave and Optical Technology Letters*, 21(2):151–6, 1999.
- [35] D. V. Krupezevic, V. J. Brankovic, and F. Arndt. A simplified 2D graded mesh FD-TD algorithm for calculating the characteristic impedance of shielded or open planar waveguides with finite metallization thickness. In *1993 IEEE MTT-S International Microwave Symposium Digest (Cat. No. 93CH3277-1)*, volume 2, pages 997–1000, Atlanta, GA, USA, 1993.
- [36] W. Yu, R. Mittra, and S. Dey. Application of the nonuniform FDTD technique to analysis of coaxial discontinuity structures. *IEEE Transactions on Microwave Theory and Techniques*, 49(1):207–9, 2001.
- [37] A. Tinniswood, G. Lazzi, and O. P. Gandhi. The use of the expanding grid FDTD technique for simulation of CAD-derived personal wireless telephones. In *IEEE Antennas and Propagation Society International Symposium*, volume 1, pages 508–11, Atlanta, GA, USA, 1998.
- [38] A. Tinniswood, G. Lazzi, and O. P. Gandhi. The use of the expanding-grid FDTD method for simulation of CAD-derived personal wireless telephones. *Microwave and Optical Technology Letters*, 22(1):24–29, 1999.
- [39] P. Bernardi, M. Cavagnaro, S. Pisa, and E. PiuZZi. A graded-mesh FDTD code for the study of human exposure to cellular phones equipped with helical antennas. *Applied Computational Electromagnetics Society Journal*, 16(2):90–6, 2001.
- [40] Yu Wenhua, Yeo Junho, and R. Mittra. Application of non-uniform and conformal FDTD techniques to the analysis of a class of planar antennas. *IEEE Antennas and Propagation Society International Symposium*, 2:674–7, 2002.
- [41] N. T. Sangary, E. A. Navarro, Wu Chen, and J. Litva. Application of non-uniform FDTD method to PCS antennas. In *IEEE Antennas and Propagation Society International Symposium Digest*, volume 2, pages 1148–51, Newport Beach, CA, USA, 1995.

- [42] Shen Guoqiang, Chen Yinchao, and R. Mittra. An efficient non-uniform FDTD method for analysis of propagation characteristics of optical fiber waveguides. In *IEEE Antennas and Propagation Society International Symposium Digest*, volume 3, pages 1488–91, Atlanta, GA, USA, 1998.
- [43] Shen Guoqiang, Chen Yinchao, and R. Mittra. A nonuniform FDTD technique for efficient analysis of propagation characteristics of optical-fiber waveguides. *IEEE Transactions on Microwave Theory and Techniques*, 47(3):345–49, 1999.
- [44] B. Q. Gao and O. P. Gandhi. An expanding-grid algorithm for the finite-difference time-domain method [EM deposition in human body]. *IEEE Transactions on Electromagnetic Compatibility*, 34(3):277–83, 1992.
- [45] P. Mezzanotte, L. Roselli, C. Huber, H. Zscheile, and W. Heinrich. On the accuracy of the finite-difference method using mesh grading. In L. Kirby, editor, *Proceedings of 1995 IEEE MTT-S International Microwave Symposium*, volume 2, pages 781–4, Orlando, FL, USA, 1995.
- [46] W. Heinrich, K. Beilenhoff, P. Mezzanotte, and L. Roselli. Optimum mesh grading for finite-difference method. *IEEE Transactions on Microwave Theory and Techniques*, 44(9):1569–74, 1996.
- [47] Y. Chen, M. Yang, K. Sun, and R. Mittra. Application of the non-uniform FDTD algorithm on an auto-adjustable mesh to the analysis of scattering parameters of a sandwiched-type coplanar waveguide with adjacent vias in PCBs. *International Journal of Electronics*, 89(10):791–800, 2002.
- [48] S. Xiao, R. Vahldieck, and H. Jin. A fast two-dimensional FDTD full-wave analyser with adaptive mesh size. In *IEEE MTT-S International Microwave Symposium*, volume 2, pages 783–6, Albuquerque, NM, USA, 1992.
- [49] N. Chavannes, E. Ofii, F. Nunez, and N. Kuster. Effective multi-goal optimization of CAD derived mobile phones using novel

- genetic algorithms. In *19th International Conference on Applied Electromagnetics and Communications*, pages 197–200, 2007.
- [50] E. Offi, F. Nunez, N. Chavannes, E. Cherubini, and N. Kuster. Design and optimization of CAD derived mobile phone antennas using multi-goal genetic algorithms. In *2007 IEEE Antennas and Propagation International Symposium*, pages 2221–4, 2008.
- [51] S. Benkler. *Robust Conformal Subcell Modeling for Electromagnetic Simulations in Time Domain*. PhD thesis, Eidgenössisch Technische Hochschule Zürich, 2007. Diss. ETH - Nr. 16969.
- [52] Foundation for Information Technologies in Society (ITIS). <http://www.itis.ethz.ch>.
- [53] A. Christ, W. Kainz, E. Hahn, K. Honegger, J. Shen, R. Rascher, R. Janka, W. Bautz, B. Kiefer, P. Schmitt, H.-P. Hollenbach, J. Chen, A. Kam, E. Neufeld, M. Oberle, and N. Kuster. The “Virtual Family” Project - Development of anatomical whole-body models of two adults and two children. *Proceedings of the 23rd Annual Review of Progress in Applied Computational Electromagnetics (ACES)*, 2007. Session 16: Modeling of Biomedical Problems - 1 (March 21).
- [54] P. Futter, N. Chavannes, R. Tay, M. Meili, A. Klingenbock, K. Pokovic, and N. Kuster. Reliable prediction of mobile phone performance for realistic in-use conditions using the FDTD method. *Antennas and Propagation Magazine, IEEE*, 50(1):87–96, 2008.
- [55] M. Celuch-Marcysiak, W. Gwarek, and M. Sypniewski. A simple and effective approach to FD-TD modelling of structures including lossy metals. In *Asia-Pacific Microwave Conference*, volume 2, pages 991–3, Yokohama, Japan, 1998.
- [56] M. A. Leontovich. Approximate boundary conditions for the electromagnetic field on the surface of a good conductor. *Investigations on Radiowave Propagation*, II:5–12, 1957.
- [57] T. B. A. Senior. Impedance boundary conditions for imperfectly conducting surfaces. *Applied Scientific Research, Section B*, 8(5-6):418–36, 1960.

- [58] G. S. Smith. On the skin effect approximation. *American Journal of Physics*, 58(10):996–1002, 1990.
- [59] J. H. Beggs, R. J. Luebbers, K. S. Yee, and K. S. Kunz. Finite-difference time-domain implementation of surface impedance boundary conditions. *IEEE Transactions on Antennas and Propagation*, 40(1):49–56, 1992.
- [60] J. G. Maloney and G. S. Smith. The use of surface impedance concepts in the finite-difference time-domain method. *IEEE Transactions on Antennas and Propagation*, 40(1):38–48, 1992.
- [61] T. B. A. Senior. Approximate boundary conditions. *IEEE Transactions on Antennas and Propagation [legacy, pre - 1988]*, 29(5):826–829, 1981.
- [62] W. Bächtold. *Lineare Elemente der Höchstfrequenztechnik*. Verlag der Fachvereine Zürich, 1994.
- [63] A. Álvarez Melcón. *Applications of the Integral Equation Technique to the Analysis and Synthesis of Multilayered Printed Shielded Microwave Circuits and Cavity Backed Antennas*. PhD thesis, École Polytechnique Fédérale de Lausanne, 1998. Thèse EPFL - No. 1901.
- [64] P. Crespo Valero, J.-F. Zürcher, M. Mattes, and J.R. Mosig. Benchmark III: Three-layer bandpass filter, analysis of multilayer boxed printed circuit, 2006. ESA-ESTEC 16332/02/NL/LvH, Technical Note TN504Ä3.
- [65] P. Crespo Valero. *Electromagnetic modelling of planar circuits in bounded layered media*. PhD thesis, École Polytechnique Fédérale de Lausanne, 2007. Thèse EPFL - No. 3746.
- [66] SEMCAD X. *Reference Manual for the SEMCAD X Simulation Platform for Electromagnetic Compatibility, Antenna Design and Dosimetry*, volume 11.0. SPEAG - Schmid & Partner Engineering AG, 2008.
- [67] J. G. Maloney and G. S. Smith. The efficient modeling of thin material sheets in the finite-difference time-domain (FDTD)

- method. *IEEE Transactions on Antennas and Propagation*, 40(3):323–30, 1992.
- [68] R. J. Luebbers and K. Kunz. FDTD modeling of thin impedance sheets [radar cross section calculation]. *IEEE Transactions on Antennas and Propagation*, 40(3):349–51, 1992.
- [69] L. K. Wu and L. T. Han. Implementation and application of resistive sheet boundary condition in the finite-difference time-domain method. *IEEE Transactions on Antennas and Propagation*, 40(6):628–33, 1992.
- [70] C. J. Railton. An algorithm for the treatment of curved metallic laminas in the finite difference time domain method. *IEEE Transactions on Microwave Theory and Techniques*, 41(8):1429–38, 1993.
- [71] S. Van den Berghe, F. Olyslager, and D. De Zutter. Accurate modeling of thin conducting layers in FDTD. *IEEE Microwave and Guided Wave Letters*, 8(2):75–77, 1998.
- [72] A. Lauer and I. Wolff. A conducting sheet model for efficient wide band FDTD analysis of planar waveguides and circuits. *1999 IEEE MTT-S International Microwave Symposium Digest*, 4:1589–92, 1999.
- [73] R. M. Makinen. An efficient surface-impedance boundary condition for thin wires of finite conductivity. *IEEE Transactions on Antennas and Propagation*, 52(12):3364–72, 2004.
- [74] J. Wang et al. FDTD simulation of shielding effectiveness of metal-coated plastics for pulsed electromagnetic fields. *IEICE Transactions on Communications*, E88-B(1):358–63, 2005.
- [75] J. G. Maloney and G. S. Smith. A comparison of methods for modeling electrically thin dielectric and conducting sheets in the finite-difference time-domain (FDTD) method. *IEEE Transactions on Antennas and Propagation*, 41(5):690–94, 1993.
- [76] P. A. Tirkas and K. R. Demarest. Modeling of thin dielectric structures using the finite-difference time-domain technique.

- IEEE Transactions on Antennas and Propagation*, 39(9):1338–44, 1991.
- [77] Oh Kyung Suk and J. E. Schutt-Aine. An efficient implementation of surface impedance boundary conditions for the finite-difference time-domain method. *IEEE Transactions on Antennas and Propagation*, 43(7):660–66, 1995.
- [78] C. W. Penney, R. J. Luebbers, and J. W. Schuster. Scattering from coated targets using a frequency-dependent, surface impedance boundary condition in FDTD. *IEEE Transactions on Antennas and Propagation*, 44(4):434–43, 1996.
- [79] J. H. Beggs. A FDTD surface-impedance boundary condition using z-transforms. *Applied Computational Electromagnetics Society Journal*, 13(1):14–24, 1998.
- [80] M. K. Karkkainen. FDTD surface impedance models for electrically thick dispersive material coatings. *Radio Science*, 38(3):16–1–14, 2003.
- [81] K. J. Blow and D. Wood. Theoretical description of transient stimulated Raman scattering in optical fibers. *Journal of Quantum Electronics*, 25(12):2665–73, 1989.
- [82] R. H. Enns and D. E. Edmundson. Guide to fabricating bistable-soliton-supporting media. *Physical Review A*, 47(5):4524–27, 1993.
- [83] M. Fujii, M. Tahara, I. Sagakami, and et al. High-order FDTD and auxiliary differential equation formulation of optical pulse propagation in 2-D Kerr and Raman nonlinear dispersive media. *IEEE Journal of Quantum Electronics*, 40(2):175–82, 2004.
- [84] M. Fuji et al. A simple and rigorous verification technique for nonlinear FDTD algorithms by optical parametric four-wave mixing. *Microwave and Optical Technology Letters*, 48(1):88–91, 2006.
- [85] I. Kourakis and P.K. Shukla. Nonlinear propagation of electromagnetic waves in negative-refraction-index composite materials. *Physical Review E*, 72(1):16626–1–5, 2005.

- [86] M. Ahmaddou. Negative refraction and focusing analysis in a left-handed material slab and realization with a 3D photonic crystal. *Journal of Optics A: Pure and Applied Optics*, 8(2):199–204, 2006.
- [87] A. D. Boardman et al. Negative refraction in perspective. *Electromagnetics*, 25(5):365–89, 2005.
- [88] J. B. Brock et al. Focusing inside negative index materials. *Applied Physics Letters*, 85(13):2472–74, 2004.
- [89] Z. G. Dong et al. Numerical simulations of negative-index refraction in wedge-shaped metamaterials. *Physical Review E*, 72(1):016607–1–4, 2005.
- [90] C. Enkirch et al. Magnetic metamaterials at telecommunication and visible frequencies. *Physical Review Letters*, 95:203901–1–4, 2005.
- [91] S. Foteinopoulou et al. Refraction in media with a negative refractive index. *Physical Review Letters*, 90(10):107402–1–4, 2003.
- [92] M. Grzegorzczuk et al., T. Properties of left-handed metamaterials: Transmission, backward phase, negative refraction and focusing. *IEEE Transactions on Microwave Theory and Techniques*, 53(9):2956–67, 2005.
- [93] J. H. Greene and A. Taflove. General vector auxiliary differential equation finite-difference time-domain method for nonlinear optics. *Optics Express*, 14(18):8305–10, 2006.
- [94] K. Königsberger. *Analysis 2*. Springer, 2000.
- [95] S. Longhi. Gap solitons in metamaterials. *Waves in Random and Complex Media*, 15(1):119–26, 2005.
- [96] E. P. Kosmidou and T. D. Tsiboukis. An FDTD analysis of photonic crystal waveguides comprising third-order nonlinear materials. *Optical and Quantum Electronics*, 35(10):931–46, 2003.

- [97] S. Schild, N. Chavannes, and N. Kuster. New FDTD scheme for the modeling of arbitrarily curved thin conductive sheets. *IEEE Antennas and Propagation Society International Symposium*. July 9-14 2006, Albuquerque, NM, USA.
- [98] S. Schild, M. Ammann, N. Chavannes, and N. Kuster. A novel approach to model linear and nonlinear dispersion with ADE-FDTD. *Progress in Electromagnetics Research Symposium*. Prague, Czech Republic, 2007.
- [99] S. Schild, N. Chavannes, and N. Kuster. A robust method to accurately treat arbitrarily curved 3-D thin conductive sheets in FDTD. *IEEE Transactions on Antennas and Propagation*, 55(12):3587–94, 2007.
- [100] S. Schild, N. Chavannes, and N. Kuster. Accurate treatment of arbitrarily curved 3D thin conductive sheets in real-world FDTD applications. *3rd International Workshop on Antenna Technology*. March 21-23 2007, Cambridge, UK.
- [101] S. Schild, M. Ammann, N. Chavannes, and N. Kuster. A fast ADE-FDTD method for linear and nonlinear dispersion. *XVIth International Workshop on Optical Waveguide Theory and Numerical Modelling*. June 13-14 2008, Eindhoven, Netherlands.
- [102] S. Schild, N. Chavannes, and N. Kuster. Extended FDTD scheme for thin conductive sheets with geometrical curvature analysis. *IEEE Antennas and Propagation Society International Symposium*. June 9-15 2008, Honolulu, HI, USA.
- [103] S. Schild, M. Ammann, N. Chavannes, and N. Kuster. A novel approach to model linear and nonlinear dispersion with ADE-FDTD. *IEEE Antennas and Propagation Society International Symposium*, July 5-12 2008.
- [104] S. Schild, M. Ammann, N. Chavannes, and N. Kuster. A fast auxiliary differential equation finite-difference time-domain method for linear and nonlinear dispersion. 2008. To be published.

- [105] S. Schild, N. Chavannes, and N. Kuster. A novel interactive FDTD grid generation algorithm with geometrical analysis for highly complex 3D models. 2008. To be published.

Curriculum Vitae

Personal Information

- **Date of birth** 4. April 1977
- **Place of birth** Basel BS, Switzerland
- **Citizenship** Swiss
- **Parents** Heidi und Kaspar Schild

Education

- **Kantonsschule Wohlen, Switzerland**
1993 - 1997
- **Department of Physics, ETH Zurich, Switzerland**
1997 - 1999
- **Department of Information Technology and Electrical Engineering, ETH Zurich, Switzerland**
Master Studies
1999 - 2005

- **School of Electrical and Computer Engineering, Georgia Institute of Technology, Atlanta, GA, USA**
Exchange Semester; Master Thesis
August 2004 - December 2004
- **Foundation for Research on Information Technologies in Society, Zurich, Switzerland**
PhD Studies
2005 - 2008

Theses & Internships

- **Industrial Internship Philips Semiconductors AG, Zurich, Switzerland**
August - October 2002
- **Semester Thesis *Embedded System für neuartige Durchflussensoren***
Electrical Engineering and Design Laboratory,
ETH Zurich, Switzerland
Supervisor: Dr. Daniel Schrag
2003
- **Semester Thesis *Single Spike Recovery***
Physical Electronics Laboratory, ETH Zurich, Switzerland
Supervisor: Sadik Hafizović
2004
- **Master Thesis *A Silicon Micromachined Gyroscope***
Microsystems Group, Georgia Institute of Technology, Atlanta, GA, USA
Physical Electronics Laboratory, ETH Zurich, Switzerland
Supervisor: Prof. Oliver Brand, Georgia Institute of Technology
August 2004 - February 2005